Uniwersytet Jagielloński
Instytut Fizyki im. Mariana Smoluchowskiego
Zaklad Teorii Materii Skondensowanej i Nanofizyki

Wojciech Brzezicki

Ground states and excitations in spin models with orbital degrees of freedom

Thesis written under the supervision of
Prof. dr hab. Andrzej M. Oleś, presented
in fulfillment of the requirements for the
degree of Doctor of Science in the
Jagiellonian University of Cracow

Kraków, 2012

I thank Professor Andrzej M. Oleś for valuable comments and help in realization of this work and great support during my doctoral sudies.

I thank Professor Jacek Dziarmaga for insightful discussions on the 2D KK model and for suggesting the perturbative treatment of double-AF state.

I thank Professor Krzysztof Rościszewski for his patience and kind support.

A partial support by the Foundation for Polish Science (FNP) and by the Polish Ministry of Science and Higher Education under Projects No. N202 069639 and N202 068 32/1481 is kindly acknowledged.

This thesis is based on the following publications of the author:

1. W. Brzezicki and A. M. Oleś, Eur. Phys. J. B **66**, 361 (2008).

2. W. Brzezicki and A. M. Oleś, Phys. Rev. B **80**, 014405 (2009).

3. W. Brzezicki and A. M. Oleś, J. Phys.: Conf. Ser. **200**, 012017 (2010).

4. W. Brzezicki and A. M. Oleś, Phys. Rev. B **82**, 060401 (2010).

5. W. Brzezicki, *Lectures On The Physics Of Strongly Correlated Systems XV*, edited by A. Avella and F. Mancini, AIP Conference Proceedings, Vol. 1297 (AIP, New York, 2010) pp. 407-411.

6. W. Brzezicki and A. M. Oleś, Phys. Rev. B **83**, 214408 (2011).

7. W. Brzezicki, *Lectures On The Physics Of Strongly Correlated Systems XV*, edited by A. Avella and F. Mancini, AIP Conference Proceedings, Vol. 1419 (AIP, New York, 2011) pp. 261-265.

Contents

List of abbreviations:

1D	one-dimensional
2D	two-dimensional
3D	three-dimensional
AF	antiferromagnetic
AO	alternating-orbital
FM	ferromagnetic
FO	ferro-orbital
KK	Kugel-Khomskii
MF	mean-field
NN	nearest-neighbor
NNN	next-nearest-neighbor
PBC	periodic boundary condition
QIM	Quantum Ising Model
QCM	Quantum Compass Model
QPT	quantum phase transition
SO	spin-orbital

Chapter 1

Introduction

1.1 Models with spin and orbital degrees of freedom

The wave function of an electron takes various shapes when bound to an atomic nucleus by Coulomb force. Consider a transition-metal atom in a crystal with perovskite structure. It is surrounded by six oxygen ions, which give rise to the crystal field potential which lowers the rotational symmetry of the system and quenches the orbital angular momentum by introducing the crystal field splitting of the d orbitals. Wave functions pointing towards O^{2-} ions have higher energy in comparison with those pointing between them. The former wave functions are called e_g orbitals (x^2-y^2 and $3z^2-r^2$), whereas the latter ones are the t_{2g} orbitals (xy, yz and zx)– see Fig. 1.1. When electrons are put into these wave functions, the ground state is determined by the Hund's exchange interaction which stabilizes the configuration

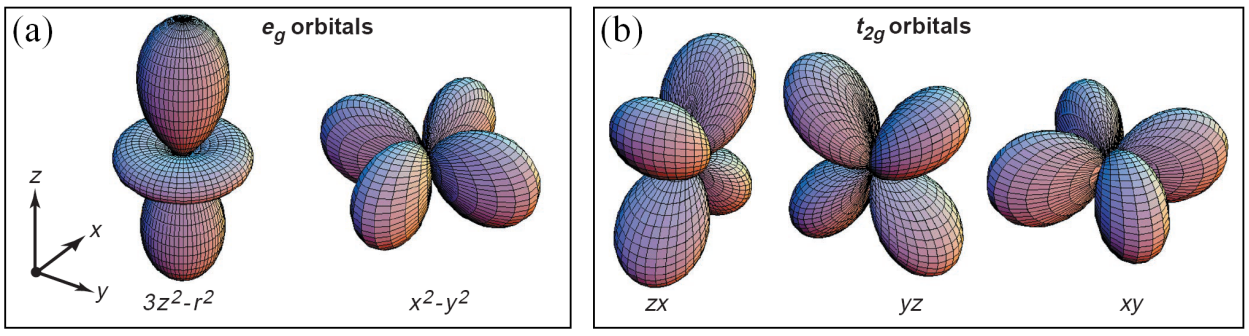

Figure 1.1: View of the five d orbitals. In the cubic crystal field the fivefold degeneracy, occurring for a single atom, is lifted to two e_g orbitals and three t_{2g} orbitals.

with all spins being parallel, if the d electrons number is $n \leq 5$ (otherwise the same applies to the hole spins). For example in $LaMnO_3$, where Mn^{3+} is in a d^4 configuration, three electrons are put to t_{2g} orbitals and one occupies an e_g orbital and their spins are aligned parallel leading to total spin $S = 2$. The relativistic correction gives rise to the spin-orbit interaction $H_{spin-orb.} = \lambda \mathbf{LS}$, where $\mathbf{L}$ and $\mathbf{S}$ are the orbital and spin angular momenta. This interaction plays an important role in some cases, especially when t_{2g} states are partialy filled by electrons. However, the coupling between spin and orbital degrees of freedom described below is not due to this relativistic spin-orbit coupling.

Up to now, we have considered only one transition-metal ion. However, in solids, there are periodic arrays of ions. There are two important aspects caused by this: one is the magnetic interactions, i.e., exchange interactions, between the spins and the other is the possible band formation and metallic conduction of the electrons. Before explaining these two, let us introduce the Mott insulating state. Band theory predicts an insulating state when all bands are either fully occupied or empty, whereas a metallic state occurs under different conditions. However, it is also possible that the system is insulating because of the Coulomb interaction when the electron number is an integer per atom, even if the band theory without the period doubling predicts a metallic state. This occurs when the kinetic energy gain is relatively small and blocked by the strong Coulomb repulsion energy U, and the electron cannot hop to the other atom. This insulator is called a correlated or Mott insulator. The most important difference from the usual band insulator is that the internal degrees of freedom, spin and orbital, still survive in the Mott insulator. $LaMnO_3$ is a Mott insulator with spin $S = 2$ and the orbital degrees of freedom. The spin $S = 2$ is here represented by the t_{2g} spin 3/2 strongly coupled to the e_g spin 1/2 by ferromagnetic J_H (Hund's coupling). The two possible choices of an occupied e_g orbital are represented by the pseudospin $\mathbf{T}$ in the way that $T^z = 1/2$ when orbital $d_{x^2-y^2}$ is occupied and $T^z = -1/2$ when orbital $d_{3z^2-r^2}$ is occupied. Due to the anticommutation rules for electrons three components of $\mathbf{T}$ satisfy similar commutation relation as the spin operator.

As the exchange interactions arise from virtual excitations of electrons which carry both spin and orbital flavor, there is a strong coupling between the spin $\mathbf{S}$ and pseudospin $\mathbf{T}$ on different ions. As a result the exchange interaction is represented by the generalized Heisenberg Hamiltonian [1] of the form:

$$H_{sup-ex} = \sum_{\langle i,j \rangle} \left\{ J_{i,j} \left(\mathbf{T}_i, \mathbf{T}_j \right) \mathbf{S}_i \mathbf{S}_j + K_{i,j} \left(\mathbf{T}_i, \mathbf{T}_j \right) \right\}. \tag{1.1}$$

The exchange interactions $J_{i,j}$ and $K_{i,j}$ originate from the quantum mechanical process with intermediate virtual states on oxygen ion lying between two transition metal ions at neighboring sites i and j called superexchange. This is a direct generalization of the superexchange for nondegenerate states [2, 3] to the case of orbital degeneracy and thus provides an immediate link between magnetism and orbital ordering– see [4, 5] for reviews on this subject. The rotational symmetry in the spin space leads to the $SU(2)$ invariant form of the interaction but the orbital degrees of freedom usually lead to anisotropy. In general, the transfer integral $t_{i,j}$ depends on the direction of the bond $\langle i,j\rangle$ and also on the pair of the two coupled orbitals from the set $\{x^2-y^2, 3z^2-r^2\}$. This gives rise to the anisotropy of the Hamiltonian in the pseudospin space as well as in the real space. For example, the transfer integral between the two neighboring Mn atoms in the crystal lattice is determined by the overlaps of the d orbitals with the p orbital of the oxygen atom between them. The overlap between the x^2-y^2 and p_z orbitals is zero for the symmetry reasons. Therefore, the electron in the $d_{x^2-y^2}$ orbital cannot hop along the z axis. This fact will be important later in our discussion.

One can consider the long-range ordered state of the orbital pseudospin $\mathbf{T}$ as well as the spin $\mathbf{S}$. In many respects there are analogies between spin and orbital orders in spite of the anisotropy in the pseudospin space. However, there is one more aspect that is special to $\mathbf{T}$ —Jahn-Teller (JT) coupling [6, 7]. Because each orbital has different anisotropy of the wave function, it is coupled to certain displacements of the oxygen atoms surrounding the transition-metal ion. For example, when the two apical O atoms move toward the ion, the energy of $3z^2-r^2$ electron becomes higher than the one of x^2-y^2 and the degeneracy is lifted. This is called the JT effect [6] and is represented by the following Hamiltonian for a single octahedron:

$$H_{JT} = -g\left(T^x Q_2 + T^z Q_3\right), \tag{1.2}$$

where (Q_2, Q_3) are the coordinates for the displacements of oxygen atoms surrounding the transition-metal atom and g is the coupling constant. When the crystal is considered, $\{Q_2, Q_3\}$ should be generalized to $\{Q_{i,2}, Q_{i,3}\}$, which is represented as the sum of the phonon coordinates and the uniform component (u_2, u_3). Here, (u_2, u_3) describes the crystal distortion as a whole. When the long-range orbital order exists, i.e., $\langle T_i^z\rangle \neq 0$ or $\langle T_i^x\rangle \neq 0$, the JT distortion is always present.

The orbital-only models neglecting spin degrees of freedom (e.g. in a ferromagnet) are already interesting subject to study, as the full many-body problem with active orbital, spin,

lattice and charge degrees of freedom is far from being understood. Thus one can concentrate on a single aspect and investigate orbital degrees of freedom in detail [8]. These models are non-trivial and interesting in themselves as the symmetry of real space, the point group symmetry of the lattice, is reflected in orbital models leading to anisotropy and intrinsic frustration. Spins, in contrast, are essentially decoupled from the lattice as long as relativistic spin–orbit coupling is small, so that general spin Hamiltonians are Heisenberg-like and exhibit continuous spin rotation SU(2) symmetry. In any realistic orbital Hamiltonian, continuous orbital rotation symmetry is manifestly broken. Finally, in many compounds, the orbital ordering temperature is higher than the magnetic ordering temperature. For example, in $LaMnO_3$ the Nèel temperature is $T_N \simeq 146K$ [9], while orbital ordering occurs already below $T_{OO} \approx 780K$. This implies that there is a large temperature range in which the system is orbital-ordered while the spins are still disordered. This justifies a description of the systems in terms of orbital-only Hamiltonians such as the so-called 120° model, in classical [10] or quantum version [11], for e_g orbitals doublet and classical [12] or quantum compass [5] model for t_{2g} orbital triplet.

Now, going beyond the Mott insulating state, let us consider the doped carriers into a Mott insulator. High-T_c superconducting cuprates, e.g., $La_{2-x}Sr_xCuO_4$, offer the most dramatic example of such a carrier doping. However, the two-dimensional (2D) nature of the lattice, as well as the larger coherent JT distortion for the Cu_2O sheet, gives a large energy splitting between x^2-y^2 or $3z^2-r^2$ orbitals, and only x^2-y^2 is relevant. In the case of $La_{1-x}Sr_xMnO_3$, known for the colossal magnetoresistance effect [4], Mn^{4+} or holes with concentration x are doped, and still, the orbital degrees of freedom are active at undoped Mn^{3+} ions. The most important and fundamental interaction in the doped case is the double exchange interaction [13–15], when e_g electrons are forced to be parallel to the localized t_{2g} spins by the strong J_H (we consider electron doped manganites as an example). The hopping amplitude $t_{i,j}$ for a doped e_g electron to hop from atom i to j depends on spin wave functions of the t_{2g} electrons at sites i and j, $|\chi_i\rangle$ and $|\chi_j\rangle$, in the way that effectively $t_{i,j} \simeq t \langle\chi_i|\chi_j\rangle$. Thus, $|t_{i,j}|$ explicitly depends on the relative orientation of the two spins as: $|\langle\chi_i|\chi_j\rangle| = \cos(\theta_{i,j}/2)$ ($\theta_{i,j}$ the angle between the two spins) and it is maximized for parallel spins and is zero for antiparallel spins. Therefore, the kinetic energy gain of the doped holes is maximized for the ferromagnetic configuration of the spins. Such mechanism of ferromagnetism is called double exchange.

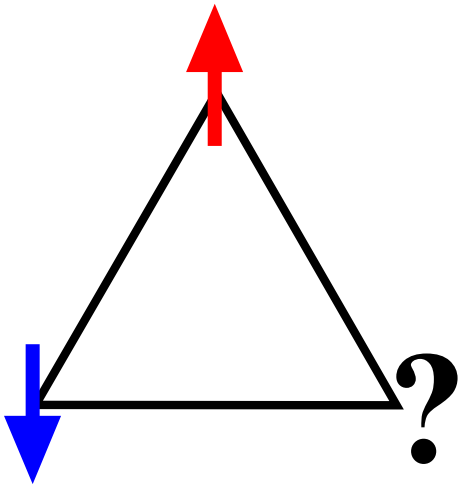

Figure 1.2: Example of frustration for a classical AF Ising model on a triangle.

1.2 Frustration

Frustration in solid-state physics means that the Hamiltonian contains conflicting interactions which energy cannot be minimized in an single configuration. Frustration can be caused by the form of interactions or by the geometry of the lattice. In Fig. 1.2 we show a canonical example of a frustrated configuration of classical Ising spins on vertices of a triangle. If the interactions between nearest neighbors are antiferromagnetic then two spins can minimize the energy of their interaction but the third one cannot; if it points down it will minimize the interaction with the up spin but maximize the one with the down spin, if it points up then situation will be opposite. Thus, the third spin can point up or down and the total energy will be the same leading to the two-fold degeneracy of the ground-state. The situation become more complicated in the thermodynamic limit, i.e. it turns out that a classical AF Ising model on a triangular lattice has no magnetic order in any temperature [16] whereas in FM version it behave similarly to the square lattice Ising model solved by Lars Onsager (see Ref. [17] for a gentle version of the Onsager's solution). On the one hand, periodically distributed frustrated Ising interactions do not suffice to destroy magnetic long-range order in a two-dimensional (2D) system, but only reduce the temperature of the magnetic phase transition [18]. The problem of frustration becomes even more complex in case of quantum interactions. For instance, 2D Heisenberg model on kagome and triangular lattices exhibits spin liquid behavior with no signs of a symmetry breaking in zero temperature and $S = 1/2$ bosonic spinon excitations [19] whereas the 2D AF $J_1 - J_2$ Heisenberg model shows the non-

magnetic collinear order in the intermediate coupling ($0.4 \lesssim J_2/J_1 \lesssim 0.65$) region [20] being either a spin liquid or a valence-bond state. Despite the absence of any symmetry breaking, the spin liquid state often exhibits a peculiar non-local order called a topological order, a property of which one becomes aware only on crossing the entire system or on wrapping once around it, if a system is placed on a cylinder or a torus [21]. On the other hand, when the model is quantum, increasing frustration of exchange interactions may trigger a quantum phase transition (QPT), as for instance in the one-dimensional (1D) compass model [22] were the critical phase with algebraic correlations is of the measure zero in the parameter space. Another example of frustrated magnetic system is a spin ice, being essentially classical in case of large spins, where spins lie on the veritices of corner-sharing tetrahedra in a pyrochlore lattice and the ground state belongs to a manifold of states satisfying the so-called ice rule leading to a macroscopic ground-state degeneracy [23]. The excitations in such systems can exhibit a very exotic nature involving magnetic monopoles and Dirac strings [24].

An important feature of spin-orbital (SO) superexchange, which arises in transition metal oxides with active orbital degrees of freedom [4, 5, 25, 26], is generic frustration of the orbital interactions. In such SO models frustration is intrinsic and follows from the directional nature of orbital interactions [27], so it is also present on lattices without geometrical frustration, such as the three-dimensional (3D) perovskite lattice of $KCuF_3$ or $LaMnO_3$. Usually such frustration is removed either by spin order which arises due to Hund's exchange J_H or by Jahn-Teller orbital interactions, but when these terms are absent it leads to a disordered orbital liquid ground state. Perhaps the simplest realistic example of this behavior is the (Kugel-Khomskii) model for Cu^{2+} ions in the d^9 electronic configuration at $J_H = 0$, where a disordered ground state was found [28]. Examples of such disordered states are either various valence-bond phases with singlet spin configurations on selected bonds [29], or orbital liquids established both in t_{2g} systems [30] and in e_g systems [31] in three dimensions. Characteristic features of SO models are enhanced quantum effects and entanglement [32], so their ground states cannot be predicted using mean-field decoupling schemes. Also in doped systems some unexpected features emerge for frustrated orbital superexchange interactions, and the quasiparticle states are qualitatively different from those arising in the spin t–J model [33].

A qualitatively new SO liquid phase may arise when the superexchange interactions are also geometrically frustrated, as it happens on the triangular lattice [34] where sometimes orbital frustration is cured by the tendency towards spin-singlets formation [35]. This means that the two types of frustration can cancel out. The mixture of geometrical and orbital frustration was also proposed for explaining the difference in magnetic phase diagrams of

$LiNiO_2$ and $NaNiO_2$, which are otherwise very similar, by the resonating valence-bond ground states with SO entanglement [36]. This however turned out to be insufficient to explain the absence of magnetic order and the low-temperature behaviour of the magnetic susceptibility in $LiNiO_2$ [37] which requires an extension of the microscopic model by a description of both the interlayer coupling and of the coupling between orbitals and the lattice.

1.3 Considered problems

In the following parts of this dissertation we will address the problem of orbital interactions using two generic models: the pseudospin model and the simplest SO model which in general cases have no exact solutions. In Chapter 2 we consider the so-called quantum compass model (QCM), belonging to the class of orbital-only models originating from the superexchange for t_{2g} triplet [8]. First, we will search for its exact, analytical solution for a quasi-one-dimensional lattice with geometry of a ladder including its ground-state properties and possible excitations at finite temperature. Then we will study a two-dimensional (2D) case, on one hand focusing on its symmetries and analytical properties in the ground state and on the other hand presenting the results of exact diagonalization obtained for finite square clusters, providing information on both ground state and the structure of excited states.

In Chapter 3 we consider a SO interplay and we present the phase diagrams of the SO Kugel-Khomskii model [1] for a bilayer, 2D and 3D square lattices, depending on the Hund's exchange coupling and crystal field splitting. The phase diagrams are obtained using cluster mean-field (MF) approximation, in zero and finite temperature, giving qualitatively different results than a standard, single-site mean-field method, which will be showed. The most interesting configurations, including valence-bond phases and phases with entangled SO order, will be further characterized by the behavior of order parameters, correlations and SO covariances at the quantum and thermal phase transitions. Finally, we will explain some exotic types of magnetic orders, encountered in the cluster MF approach, with effective, perturbative spin Hamiltonians derived around different states with orbital order.

Chapter 2

Quantum Compass Model

Although orbital interactions are in reality rather complicated [8, 27, 30, 32], a generic and simplest model of this type is the so-called quantum compass model introduced in Ref. [5], when the coupling along a given bond is Ising-like, but different spin components are active along different bond directions, for instance $J_x\sigma_i^x\sigma_j^x$ and $J_z\sigma_i^z\sigma_j^z$ along a and b axis in the 2D compass model. The compass model is challenging already for the classical interactions [10]. Recent interest in this model is motivated by its interdisciplinary character as it plays a role in the variety of phenomena beyond the correlated oxides; is is also dual to recently studied models of $p + ip$ superconducting arrays [38], namely Xu and Moore Hamiltonian [39], and to the toric code model in a transverse field [40]. Its 2D and 3D version was studied in the general framework of unified approach to classical and quantum dualities [41] and in 2D it was proved to be self-dual [39]. QMC was also suggested as an effective model for Josephson arrays of protected qubits [42], as realized in recent experiment [43]. Finally, it could describe polar molecules in optical lattices and systems of trapped ions [44].

QCM in two dimensions describes first quantum phase transition (QPT) between competing types of nematic orders, favored either by x or $z-$ part of the Hamiltonian and accompanied by discontinuous behavior of the nearest-neighbor (NN) spin correlations [45], when anisotropic interactions are varied through the isotropic point $J_x = J_z$, as shown by high-order perturbation theory [46], rigorous mathematical approach [47], mean-field theory on the Jordan-Wigner fermions [48] and sophisticated pair-entangled product states (PEPS) numerical studies [40]. Thus, in the thermodynamic limit the model is frustrated because the energy of bonds in one direction is not minimized. On the contrary, these bonds give no energy contribution and are totally ignored. What more, the quantum Monte-Carlo studies of

the isotropic QCM proved that the nematic order remains stable at finite temperature up to $T_c = 0.055J$ and the phase transition to disordered phase stays in the Ising universality class [49]. As shown by Douçot *et. al.* [42], the eigenstates of the QCM are twofold degenerate and the number of low-energy excitations scales as linear size of the system. Further on, it was proved by exact diagonalization of small systems that these excitations correspond to the spin flips of whole rows or columns of the 2D lattice and survive when a small admixture of the Heisenberg interactions is included into the compass Hamiltonian [50]. The elaborated multiscale entanglement-renormalization ansatz (MERA) calculations together with high-order spin wave expansion [51] showed that the 2D QCM undergoes a second order QPT when the interactions become less frustrated, i.e. when they are modified smoothly towards classical Ising model. In the same paper [51] we also find that the isotropic QCM is not critical in the sense that the spin waves remain gapfull in the ground state confirming that the order of 2D QCM is not of the magnetic type.

The 1D, generalized variant of the compass model with z-th and x-th spin component interactions on bonds, that alternate on even/odd bonds as in the QCM, can be solved exactly by an analytical method in two different ways [22, 52]. We note that the 1D compass model is equivalent to the 1D anisotropic XY model, solved exactly in the seventies [53]. An exact solution of the 1D compass model demonstrates that certain NN spin correlation functions change discontinuously at the point of a QPT when both types of interactions have the same strength, similarly to the 2D QCM. This somewhat exotic behavior is due to the QPT occurring in this case at the multicritical point in the parameter space [54]. The entanglement measures together with so called quantum discord in the ground state, characterizing the quantumness of the correlations, were analyzed recently [55, 56] to find the location of quantum critical points and show that the correlations between two pseudospins on even bonds are essentially classical in the 1D QCM . While small anisotropy of interactions leads to particular short-range correlations dictated by the stronger interaction, in both 1D and 2D compass model one finds a QPT to a highly degenerate disordered ground state when the competing interactions are balanced.

2.1 Quantum compass model on a ladder

Spin ladders play an important role in quantum magnetism. Interest in them is motivated by their numerous experimental realizations in transition metal oxides [57] and has increased over the last two decades. One of recently investigated realizations of spin ladders

are $Sr_{n-1}Cu_{n+1}O_{2n}$ cuprates (with $n = 3, 5, 7, \cdots$) [58], and the simplest of them, a spin ladder with two legs connected by rungs, occurs in $Sr_2Cu_4O_6$. Excitation spectra of such antiferromagnetic (AF) spin ladders are rich and were understood only in the last decade. They consist of triplet excitations, bound states and two-particle continuum [59], and were calculated in unprecedented detail for quantum AF spin $S = 1/2$ two-leg ladder employing optimally chosen unitary transformation [60]. In some of spin ladder systems charge degrees of freedom also play a role, as for instance in α'-NaV_2O_5, where AF order and charge order coexist in spin ladders with two legs [61], or in the Cu–O planes of $La_xSr_{14-x}Cu_{24}O_{41}$, where spin and charge order coexist for some values of x [62]. This advance in the theoretical understanding of the ground states and excitation spectra of spin ladders is accompanied by recent experimental investigations of triplon spectra by inelastic neutron scattering [63] of almost perfect spin ladders in $La_4Sr_{10}Cu_{24}O_{41}$. Finally, spin ladders could serve in the theory as a testing ground for new (ordered or disordered) phases which might arise for various frustrated exchange interactions [64].

The purpose of this section, based on papers [65, 66], is to present an exact solution of the compass model on a ladder, with ZZ Ising interactions between z-th spin components along the ladder legs, and interactions on the rungs which gradually evolve from ZZ Ising interactions to XX Ising ones. In this way the interactions interpolate between the classical Ising spin ladder and the quantum compass ladder with frustrated interactions. The latter case will be called compass ladder below — it stands for a generic competition between directional orbital interactions on different bonds and can serve to understand better the physical consequences of the frustrated orbital superexchange.

This section is organized as follows. The model and its invariant dimer subspaces are introduced in Sec. 2.1.1. Next the ground state and the lowest excited states of the model are found in Sec. 2.1.2 by solving the model in all nonequivalent subspaces. Thereby we discuss the role played by defects in spin configuration and show that the ground state is obtained by solving the 1D quantum Ising (pseudospin) model (QIM). Using a finite system, we provide an example of the energy spectrum, and next extrapolate the ground state energy obtained for finite systems to the thermodynamic limit. We also present the changes of spin correlations at the QPT, and derive the long-range spin correlations. Next we construct canonical ensemble for the compass ladder in Sec. 2.1.3 and present the details concerning the calculation of energies in the Appendix A. The constructed partition function is used to derive such thermodynamic properties of the compass ladder as the temperature variation of spin correlations, and the average length of fragmented chains separated by kinked areas

in Sec. 2.1.4. In Sec. 2.1.5 we present the evolution of heat capacity C_V when interactions change from the Ising to compass ladder for a small ladder of $2L = 8$ spins, and next analyze C_V for a large (mesoscopic) compass ladder of $2L = 104$ spins. While the characteristic excitation energies responsible for the maxima in heat capacities can be deduced from the energy spectrum for $2L = 8$ spins, generic features of excitations follow from the form of C_V in case of the mesoscopic compass ladder. Final discussion and the summary of results are given in Sec. 2.1.6.

2.1.1 Compass ladder Hamiltonian and invariant subspaces

We consider a spin ladder with L rungs $\langle 2i-1, 2i\rangle$ labeled by $i = 1, 2, \cdots, L$, see Fig. 2.1. The interactions along ladder legs are Ising-like with AF coupling J between z-th spin components $(\sigma_i^z\sigma_{i+1}^z)$, while AF interactions on the rungs interpolate between the Ising coupling of z-th $(2\sigma_{n-1}^z\sigma_{n+1}^z)$ and x-th $(2\sigma_{n-1}^x\sigma_{n+1}^x)$ spin components by varying parameter $0 \leq \alpha \leq 1$,

$$\mathcal{H}(\alpha) \;=\; 2J\sum_{i=1}^{L}\left\{\alpha\sigma_{2i-1}^x\sigma_{2i}^x + (1-\alpha)\sigma_{2i-1}^z\sigma_{2i}^z\right\} + J\sum_{i=1}^{L}\left(\sigma_{2i-1}^z\sigma_{2i+1}^z + \sigma_{2i}^z\sigma_{2i+2}^z\right)\,. \quad (2.1)$$

We assume periodic boundary conditions (PBCs) along the ladder legs, i.e., $\sigma_{2L+1}^z \equiv \sigma_1^z$ and $\sigma_{2L+2}^z \equiv \sigma_2^z$. The factor of two for the interactions on the rungs $\propto 2J$ was chosen to guarantee the same strength of interactions on the rungs (with only one rung neighbor of each spin) as along the ladder legs (with two leg neighbors). Increasing α gradually modifies the interactions on the rungs and increases frustration. For $\alpha = 0$ one finds the reference Ising ladder, while at $\alpha = 1$ the interactions describe a competition between frustrated ZZ interactions along the ladder legs and 2XX interactions on the rungs, characteristic of the compass ladder. A representative compass ladder with $L = 4$ rungs (i.e., $2L = 8$ spins) is shown in Fig. 2.1.

To solve the spin ladder given by Eq. (2.1) in the range of $0 \leq \alpha \leq 1$ we notice that $[\mathcal{H}(\alpha), \sigma_{2i-1}^z\sigma_{2i}^z] \equiv 0$. Therefore we have a set of L symmetry operators,

$$R_i \equiv \sigma_{2i-1}^z\sigma_{2i}^z\,, \quad (2.2)$$

with respective eigenvalues $r_i = \pm 1$. Each state of the system can be thus written in a basis of σ_i^z eigenvectors $|s_1, s_2, s_3, \ldots, s_{2L}\rangle$ fixed by strings of quantum numbers $s_i = \pm 1$. These vectors can be parametrized differently by a new set of quantum numbers $\{t_i\}$ and $\{r_i\}$, with

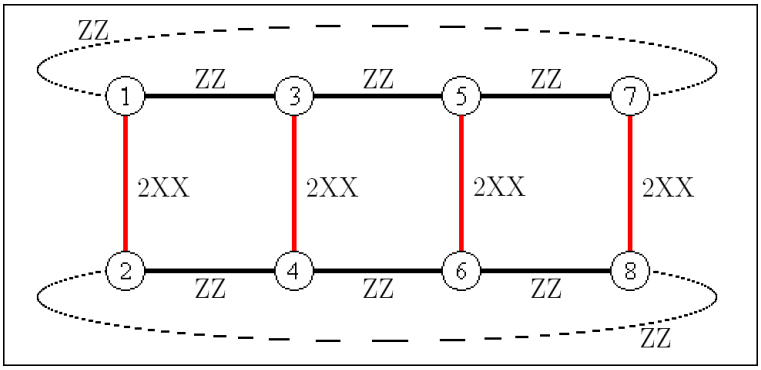

Figure 2.1: Schematic view of the quantum compass ladder with $L = 4$ rungs, described by Hamiltonian (2.1) with $\alpha = 1$. Interactions along the ladder legs labeled as ZZ (black lines) are $\sigma^z_{2i-1}\sigma^z_{2i+1}$ (upper leg) and $\sigma^z_{2i}\sigma^z_{2i+2}$ (lower leg). The interactions along the rungs labeled as $2XX$ (red lines) are $2\sigma^x_{2i-1}\sigma^x_{2i}$ (the factor of 2 simulates the PBC along the rungs). Dashed lines indicate PBCs along the ladder legs.

$i = 1, 2, \cdots, L$; they are related to the old ones by the formulae: $t_i \equiv s_{2i-1}$ and $r_i \equiv s_{2i-1}s_{2i}$. Now we introduce new notation for the basis states

$$|t_1, t_2, \ldots, t_L\rangle_{r_1 r_2 \cdots r_L} \equiv |t_1, t_1 r_1, t_2, t_2 r_2, \ldots, t_L, t_L r_L\rangle \ , \tag{2.3}$$

where the right-hand side of Eq. (2.3) is the state $|s_1, s_2, s_3, \ldots, s_{2L}\rangle$ written in terms of variables $\{t_i\}$ and $\{r_i\}$, and the left-hand side defines new notation. This notation highlights the different role played by r_i's, which are conserved quantities, and by t_i's, being new pseudospin variables. For states like in Eq. (2.3), we define new pseudospin operators τ^z_i and τ^x_i acting on $\{t_i\}$ quantum numbers as Pauli matrices, e.g. for $i = 1$:

$$\begin{aligned} \tau^x_1 |t_1, t_2, \ldots, t_L\rangle_{r_1 r_2 \cdots r_L} &= |-t_1, t_2, \ldots, t_L\rangle_{r_1 r_2 \cdots r_L} \ , \\ \tau^z_1 |t_1, t_2, \ldots, t_L\rangle_{r_1 r_2 \cdots r_L} &= t_1 |t_1, t_2, \ldots, t_L\rangle_{r_1 r_2 \cdots r_L} \ . \end{aligned} \tag{2.4}$$

A similar transformation was introduced for a frustrated spin-1/2 chain by Emery and Noguera [67], who showed that it can by mapped onto an Ising model in a transverse field. Recently this procedure was used to investigate quantum criticality in a two-leg strongly correlated ladder model at quarter filling [68].

The Hamiltonian can be now written in a common eigenbasis of R_i (2.2) operators by means of $\{\tau^x_i, \tau^z_i\}$ operators. In a subspace labeled by a string $r_1, r_2, \cdots, r_L$, the reduced

form of the Hamiltonian is

$$\mathcal{H}_{r_1 r_2 \cdots r_L}(\alpha) \equiv J \sum_{i=1}^{L} \left\{ (1 + r_i r_{i+1}) \tau_i^z \tau_{i+1}^z + 2\alpha \tau_i^x \right\} + 2J C_{\vec{r}}(\alpha) \,, \tag{2.5}$$

with a constant

$$C_{\vec{r}}(\alpha) = (1 - \alpha) \sum_{i=1}^{L} r_i \,, \tag{2.6}$$

and PBC $\tau_{L+1}^z \equiv \tau_1^z$. This leads to the exactly solvable QIM with transverse field [17, 69, 70], if only $r_i \equiv 1$ or $r_i \equiv -1$. Otherwise there are always some $\tau_i^z \tau_{i+1}^z$ interactions missing (defects created in the chain) and we obtain a set of disconnected quantum Ising chains with loose ends and different lengths. The bonds with no pseudospin interactions may stand next to each other, so in an extreme case when $r_{i+1} = -r_i$ for all i, one finds no Ising bonds and no chains appear.

One may easily recognize that the ground state of the spin ladder described by Hamiltonian (2.1) lies in a subspace with $r_i \equiv -1$ for $\alpha < 1$. First of all, $r_i \equiv -1$ minimizes $C_{\vec{r}}(\alpha)$, see Eq. (2.6). To understand a second reason which justifies the above statement let us examine a partial Hamiltonian (open chain) of the form

$$\mathcal{H}(\alpha, L_1) = 2J \sum_{i=1}^{L_1 - 1} \tau_i^z \tau_{i+1}^z + 2J\alpha \sum_{i=1}^{L_1} \tau_i^x \,, \tag{2.7}$$

with $2 \leq L_1 \leq L - 1$. Note that it appears generically in Eq. (2.5) and consists of two terms containing pseudospin operators $\{\tau_i^x\}$ and $\{\tau_i^z\}$. Let us call them $\mathcal{H}^x$ and $\mathcal{H}^z$ and denote the ground state of $\mathcal{H}^x$ as $|x\rangle$ with energy E_x. The mean value of $\mathcal{H}(\alpha, L_1)$ in state $|x\rangle$ is also E_x because every τ_i^z operator has zero expectation value in state $|x\rangle$, i.e., $\langle x|\tau_i^z|x\rangle = 0$. However, we know that $|x\rangle$ is not an eigenvector of $\mathcal{H}(\alpha, L_1)$ which implies that $\mathcal{H}(\alpha, L_1)$ must have a lower energy than E_x in the ground state. This shows that the presence of $\tau_i^z \tau_{i+1}^z$ bonds in the Hamiltonian $\mathcal{H}(\alpha, L_1)$ lowers the energy of bare $\mathcal{H}^x$. One may also expect that this energy decreases with increasing length L_1 of the chain, and is proportional to L' in the thermodynamic limit. The numerical evidence for this are plots of the ground state energy versus L_1 presented in section 3. Looking at Hamiltonian (2.5) we see that the longest chains of the type (2.7) appear in subspaces with $r_i \equiv -1$ and $r_i \equiv 1$, but the constant term $C_{\vec{r}}(\alpha)$ favors $r_i \equiv -1$ if only $\alpha < 1$. For $\alpha = 1$ the ground state can be in both subspaces, and its degeneracy follows, see below.

2.1.2 Energy spectra in invariant subspaces

Quantum Ising Model

To find the ground state of spin ladder (2.1) we need to solve the QIM that arises from Eq. (2.5) when $r_i \equiv -1$. Thus we need to diagonalize the Hamiltonian of the form

$$\mathcal{H}_{\rm QIM}(\beta,\alpha) = 2J\sum_{i=1}^{L}(\beta\tau_i^z\tau_{i+1}^z + \alpha\tau_i^x) \ , \tag{2.8}$$

which is related to our original problem by the formula

$$\mathcal{H}_{-1-1\cdots-1} = \mathcal{H}_{\rm QIM}(1,\alpha) - 2LJ(1-\alpha) \ . \tag{2.9}$$

The formal parameter β is introduced for convenience and will be used to determine the correlation functions along the ladder legs by differentiation, see below. The standard way of solving $\mathcal{H}_{\rm QIM}$ starts with Jordan–Wigner (JW) transformation. This non–linear mapping replacing spin operators by spinless fermions is of the form

$$\begin{aligned} \tau_j^z &= (c_j + c_j^\dagger)\prod_{i<j}(1-2c_i^\dagger c_i) \ , \\ \tau_j^x &= (1-2c_j^\dagger c_j) \ . \end{aligned} \tag{2.10}$$

The boundary condition for fermion operators $\{c_i\}$ after inserting them into $\mathcal{H}_{\rm QIM}$ (2.8) is antiperiodic for even and periodic for odd number of JW quasiparticles in the chain. The operator $\mathcal{P}$ of the parity of fermions,

$$\mathcal{P} = \prod_{i=1}^{L}(1-2c_i^\dagger c_i) \ , \tag{2.11}$$

corresponds to the operation of flipping all spins along the z-th axis and commutes with $\mathcal{H}_{\rm QIM}$. Therefore, the Hamiltonian can be split into two diagonal blocks, for even (+) and odd (−) number of JW fermions by means of projection operators $\frac{1}{2}(1\pm\mathcal{P})$. Therefore we write

$$\mathcal{H}_{\rm QIM} = \frac{1}{2}(1+\mathcal{P})\mathcal{H}^+ + \frac{1}{2}(1-\mathcal{P})\mathcal{H}^- \ , \tag{2.12}$$

where

$$\mathcal{H}^{\pm} \;=\; 2J\sum_{i=1}^{L}\Big\{\beta(c_i^{\dagger}-c_i)(c_{i+1}^{\dagger}+c_{i+1})-2\alpha c_i^{\dagger}c_i\Big\}+2JL\alpha\;, \tag{2.13}$$

with two different boundary conditions: $c_{L+1}=\mp c_1$ for $(\pm)$ subspaces. Let us point out that the only consequence of the non-linearity of the JW transformation is the minus sign which appears in the first bracket multiplying β. This is thanks to one-dimensionality and only NN interactions in the reduced Hamiltonian (2.5), but is not the case for the original Hamiltonian (2.1).

Next step is the Fourier transformation,

$$c_j=\frac{1}{\sqrt{L}}\sum_k e^{ijk}c_k\,, \tag{2.14}$$

with quasimomenta $k=\pm(2l-1)\pi/L$ $[l=1,2,\cdots,L/2]$ in an even subspace $(+)$, and $k=0,\pi,\pm 2l\pi/L$ $[l=1,2,\cdots,(L/2-1)]$ in an odd one $(-)$. After transforming the operators in Eq. (2.13) we obtain $\mathcal{H}^{\pm}$ in a block diagonal form,

$$\mathcal{H}^{\pm} \;=\; 4J{\sum_k}^{\pm}(\beta\cos k-\alpha)c_k^{\dagger}c_k+2J{\sum_k}^{\pm}\beta(c_k^{\dagger}c_{-k}^{\dagger}e^{ik}+h.c.)+2JL\alpha\,. \tag{2.15}$$

Diagonalization is completed by a Bogoliubov transformation, defining new fermion operators $\gamma_k^{\dagger}\equiv\alpha_k c_k^{\dagger}+\beta_k c_{-k}$ (for $k\neq 0,\pi$, while the operators c_0 and c_π have no partner and are left untransformed). Transformation coefficients α_k and β_k are obtained from the condition

$$\Big[\mathcal{H}_{\rm QIM},\gamma_k^{\dagger}\Big]=\omega_k\gamma_k^{\dagger}\,, \tag{2.16}$$

which is an eigenproblem in linear space spanned by operators $c_k^{\dagger}$ and c_{-k}. We get two eigenvectors (α_k,β_k), corresponding to the quasiparticle operators $\gamma_k^{\dagger}$ and γ_{-k}, and two corresponding eigenvalues $\omega_k=\pm E_k$, with

$$E_k(\beta,\alpha)=4J\left\{\alpha^2+\beta^2-2\alpha\beta\cos k\right\}^{1/2}\,. \tag{2.17}$$

Therefore, the Hamiltonian is brought to the diagonal form in both subspaces

$$\mathcal{H}^{+} = \sum_{k}^{+} E_k \left(\gamma_k^\dagger \gamma_k - \frac{1}{2}\right) , \tag{2.18}$$

$$\mathcal{H}^{-} = \sum_{k}^{-} E_k \left(\gamma_k^\dagger \gamma_k - \frac{1}{2}\right) + 4J(\beta-\alpha)c_0^\dagger c_0 - 4J(\beta+\alpha)c_\pi^\dagger c_\pi + 4J\alpha \ . \tag{2.19}$$

We still need to transform the parity operator $\mathcal{P}$. Luckily, the Fourier transformation does not change its form, neither does the Bogoliubov transformation and to see that one can look at the vacuum state $|0\rangle$ for quasiparticle operators γ_k. From the condition $\gamma_k|0\rangle = 0$ for all k we get

$$|0\rangle = \prod_k \left(\bar{\alpha}_k + \bar{\beta}_k c_{-k}^\dagger c_k^\dagger\right)|vac\rangle \ , \tag{2.20}$$

where $|vac\rangle$ is a true vacuum state for JW fermions or a state with all spins up. From the form of $|0\rangle$ we see that it contains a superposition of all even numbers of quasiparticles $c_k^\dagger$, and the total quasiparticle number is not fixed. Acting on the vacuum with a single creation operator $\gamma_k^\dagger$ we obtain a state with odd number of JW fermions, because $\gamma_k^\dagger$ is a linear combination of a creation $c_k^\dagger$ and annihilation c_{-k} operator of a single fermion. In this way one may get convinced that the parity of quasiparticles $\gamma_k^\dagger$ and the original $c_k^\dagger$ operators is the same.

Ground state and the energy spectrum

From the diagonal form of the QIM Hamiltonian given by Eq. (2.18) we see that the ground state of spin ladder (2.1) is simply $|0\rangle$ in subspace $r_i \equiv -1$ (or $r_i \equiv 1$ when $\alpha = 0$). For the ground state energy, one uses Eq. (2.9) to get

$$E_{-1-1\cdots-1} = E_{\mathrm{QIM}}(1,\alpha) - 2LJ(1-\alpha) \ , \tag{2.21}$$

with $E_{\mathrm{QIM}}(1,\alpha)$ given in the thermodynamic limit by an integral

$$E_{\mathrm{QIM}}(\beta,\alpha) = -\frac{L}{2\pi}\int_0^\pi dk\ E_k(\beta,\alpha)\,. \tag{2.22}$$

The ground state in the absence of transverse field (at $\alpha = 0$) is doubly degenerate — it is given by two possible Néel states. At finite $\alpha > 0$, this degeneracy is removed, and the sum of the two Néel states (symmetric state), $|0_+\rangle$, is the ground state, while their difference (antisymmetric state) becomes the first excited state. This first excited state, $|0_-\rangle = \gamma_\pi^\dagger|0_+\rangle$,

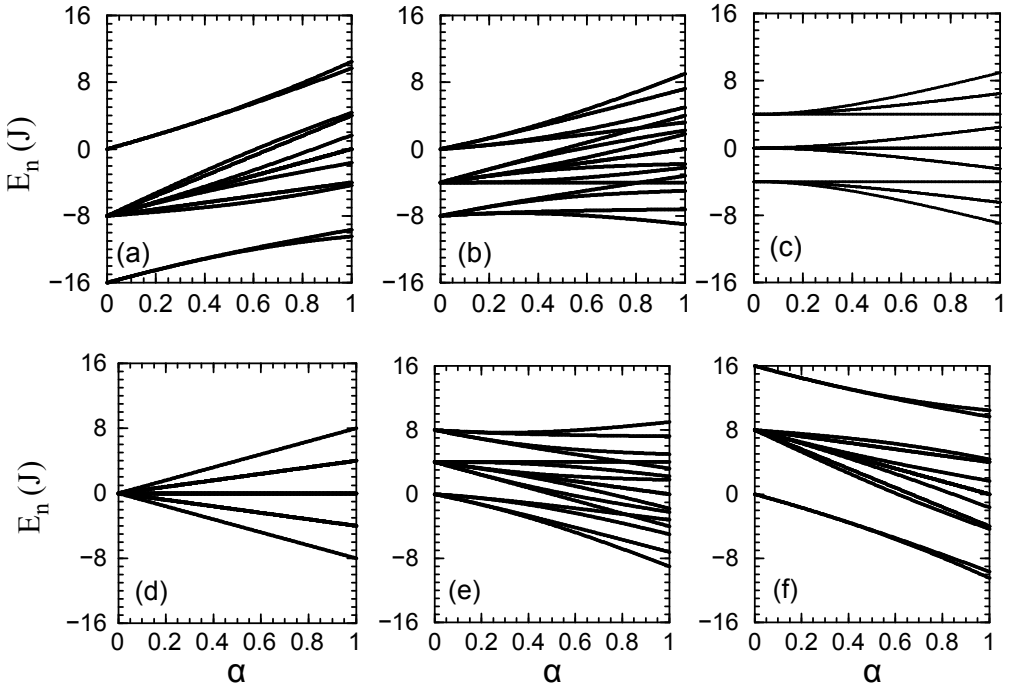

Figure 2.2: Eigenenergies E_n of the spin ladder (2.1) of Fig. 2.1 with $L = 4$ rungs for increasing α, obtained by exact diagonalization. Different panels show energies in invariant subspaces of the effective Hamiltonian (2.5), with 1 and $\bar{1}$ standing for positive or negative values of r_i: (a) $\bar{1}\bar{1}\bar{1}\bar{1}$, (b) $1\bar{1}\bar{1}\bar{1}$, (c) $11\bar{1}\bar{1}$, (d) $1\bar{1}1\bar{1}$, (e) $111\bar{1}$ and (f) 1111. While the subspaces (a) and (f) are unique, other subspaces are equivalent by symmetry to those shown in panels (b)–(e), resulting in total spectrum of 256 eigenstates. Quantum phase transition occurs at $\alpha = 1$, where the lowest eigenenergies in the subspaces (a) and (f) become degenerate. In the thermodynamic limit $L \to \infty$ the spectrum changes qualitatively — the two lowest energies in the subspaces $\bar{1}\bar{1}\bar{1}\bar{1}$ and 1111 are degenerate and the ground state from the subspace (b) ($1\bar{1}\bar{1}\bar{1}$) becomes the first excited state of the spin ladder.

stems from the same subspace and belongs to the spectrum of $\mathcal{H}^-$. The splitting of the states $|0_+\rangle$ and $|0_-\rangle$ increases with α, see Fig. 2.2(a). For finite L and $\alpha > 0$ there is always finite energy difference between the energies of $|0_+\rangle$ and $|0_-\rangle = \gamma_\pi^\dagger|0_+\rangle$ states. However, in the thermodynamic limit $L \to \infty$, this energy gap vanishes for $\alpha \leq 1$.

The full spectrum for the ladder with $L = 4$ rungs belongs to six classes of subspaces equivalent by symmetry — it is depicted in Fig. 2.2. With increasing α the spectrum changes qualitatively from discrete energy levels of the classical Ising ladder at $\alpha = 0$, with the ground state energy per spin equal $-2J$, to a narrower and quasi–continuous spectrum when the quantum compass ladder at $\alpha = 1$ is approached, with the ground state energy $-4J/\pi$ per spin. At the $\alpha = 1$ point one finds an additional symmetry; subspaces indexed

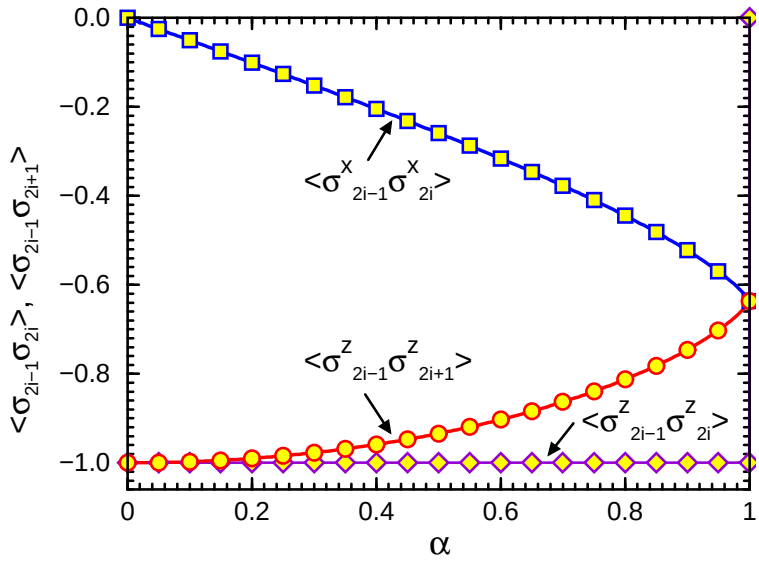

Figure 2.3: Nearest-neighbor correlation functions in the ground state for spin ladder (2.1) in the thermodynamic limit $L \to \infty$. For increasing α spin correlations $\langle \sigma^x_{2i-1}\sigma^x_{2i}\rangle$ on the rungs decrease from zero to $-2/\pi$. At the same time, AF correlations $\langle \sigma^z_{2i-1}\sigma^z_{2i+1}\rangle$ along the ladder legs gradually weaken (increase from the classical value -1 at $\alpha = 0$ to $-2/\pi$ at $\alpha = 1$), and become degenerate with the rung $\langle \sigma^x_{2i-1}\sigma^x_{2i}\rangle$ correlations at the quantum critical point $\alpha = 1$. Correlation function $\langle \sigma^z_{2i-1}\sigma^z_{2i}\rangle$ on the rungs, directly related to the subspace indices r_i, remains constant ($\langle \sigma^z_{2i-1}\sigma^z_{2i}\rangle = -1$) in the entire range of $\alpha < 1$, and jumps to 0 at $\alpha = 1$.

by $\vec{r}$ and $-\vec{r}$ are then equivalent which makes each energy level at least doubly degenerate.

Correlation functions

All the nontrivial NN spin correlation functions in the ground state can be determined by taking derivatives of the ground state energy $E_{\rm QIM}(\beta, \alpha)$ (2.22) with respect to α or β, while the others are evident from the construction of the subspaces. In this way one finds $\langle \sigma^z_{2i-1}\sigma^z_{2i+1}\rangle$ correlation along the legs and $\langle \sigma^x_{2i-1}\sigma^x_{2i}\rangle$ along the rungs, shown in Fig. 2.3. Spin correlations $\langle \sigma^z_{2i-1}\sigma^z_{2i+1}\rangle$ along the legs increase from the classical value -1 up to $-2/\pi$ for $\alpha = 1$. By symmetry, both ladder legs are equivalent and $\langle \sigma^\alpha_{2i-1}\sigma^\alpha_{2i+1}\rangle = \langle \sigma^\alpha_{2i}\sigma^\alpha_{2i+2}\rangle$ for $\alpha = x, z$. At the same time spin correlations $\langle \sigma^x_{2i-1}\sigma^x_{2i}\rangle$ along the rungs gradually develop from 0 in the classical limit to $-2/\pi$ at the quantum critical point $\alpha = 1$ which indicates increasing frustration. Both functions meet at $\alpha = 1$ which indicates balanced interactions — ZZ along the legs and 2XX along the rungs in case of the quantum compass ladder (see

Fig. 2.1).

For the remaining correlations one finds

$$\langle \sigma^x_{2i-1}\sigma^x_{2i+1}\rangle = 0 \ , \tag{2.23}$$

$$\langle \sigma^z_{2i-1}\sigma^z_{2i}\rangle = \langle R_i\rangle = r_i \ . \tag{2.24}$$

Eq. (2.23) follows from the fact that operators $\sigma^x_{2i-1}\sigma^x_{2i+1}$ do not commute with the symmetry operators R_i (2.2). In turn, averages of the symmetry operators along the rungs (2.24) are constant and equal -1 for $\alpha < 1$, but at $\alpha = 1$ they change in a discontinuous way and become zero, because at this point the degeneracy of the ground state increases to $2 \times 2 = 4$, and the spins on the rungs are disordered, so the ZZ correlations vanish.

Finally, one can calculate the long range correlation functions for z-th spin components,

$$\langle \sigma^z_{2i+a}\sigma^z_{2j+b}\rangle = r_i^{a+1} r_j^{b+1} \langle \tau^z_i \tau^z_j\rangle \ . \tag{2.25}$$

The right–hand side of Eq. (2.25) can be obtained from the QIM by the so–called Toeplitz determinant [17] and can be also found in Ref. [22]. All the long range XX correlation functions are zero in the ground state as they do not commute with R_i's operators (2.2).

Note that correlations $\langle \tau^z_i \tau^z_j\rangle$ vanish in any subspace when $|i-j|$ exceeds the length of the longest Ising chain. This is due to the fact that, as already mentioned in section 2.1.1, the effective Hamiltonian in a given subspace describes a set of completely independent quantum Ising chains. Thus, at finite temperature, one can expect that the compass ladder will be *more* disordered than a standard, 1D QIM. The problem of chain partition at finite temperature will be discussed in detail below.

Energies in the subspaces with open Ising chains

As already mentioned, the general Hamiltonian of the form (2.5) is exactly solvable only in cases when $r_i = r_{i+1}$ or $r_i = -r_{i+1}$ for all i. Therefore, one may find exactly the ground state of spin ladder (2.1), see below. Otherwise, in a general case (i.e., in arbitrary subspace) one needs to deal with a problem of the QIM on an open chain of length L_1 where $L_1 < L$, described by Hamiltonian (2.7);

$$\mathcal{H}(\alpha, L) = 2J \sum_{i=1}^{L_1-1} \tau^z_i \tau^z_{i+1} + 2J\alpha \sum_{i=1}^{L_1} \tau^x_i \ . \tag{2.26}$$

After applying the JW transformation (2.10), Eq. (2.26) takes the form

$$\mathcal{H}(\alpha, L_1) \;=\; 2J\sum_{i=1}^{L_1}\{(c_i^\dagger - c_i)(c_{i+1}^\dagger + c_{i+1}) - 2\alpha c_i^\dagger c_i\} + 2JL_1\alpha \;, \tag{2.27}$$

with an open boundary condition $c_{L_1+1}^\dagger \equiv 0$. This condition prevents us from the plane waves expansion, but we can still use the Bogoliubov transformation. We remark that the broken chain considered here is sufficient to get a general solution, and the sum over all subspaces with open (broken) chains is included in the partition function $\mathcal{Z}(\alpha)$, see Sec. 2.1.3.

We define new fermion operators $\gamma_i^\dagger$ as follows

$$\gamma_i^\dagger = \sum_{j=1}^{L_1}\Big(\alpha_{ij}c_j^\dagger + \beta_{ij}c_j\Big) \;, \tag{2.28}$$

for $i = 1, 2, \ldots, L_1$. Coefficients α_{ij} and β_{ij} can be chosen in such a way that the transformation is canonical and $\mathcal{H}(\alpha, L_1)$ takes the diagonal form:

$$\mathcal{H}(\alpha, L_1) = \sum_{i=1}^{L_1} E_i(\alpha, L_1)\left(\gamma_i^\dagger\gamma_i - \frac{1}{2}\right) \;. \tag{2.29}$$

Both excitations energies E_i and transformation coefficients $\{\alpha_{ij}, \beta_{ij}\}$ can be determined from the condition

$$[\mathcal{H}(\alpha, L_1), \gamma_i^\dagger] = E_i\gamma_i^\dagger \,. \tag{2.30}$$

This leads to an eigenequation

$$\begin{pmatrix} A & B \\ -B & -A \end{pmatrix}\begin{pmatrix} \vec{\alpha}_i \\ \vec{\beta}_i \end{pmatrix} = E_i\begin{pmatrix} \vec{\alpha}_i \\ \vec{\beta}_i \end{pmatrix} \;, \tag{2.31}$$

where A and B are matrices of size $L_1 \times L_1$ (A is a symmetric and B is an antisymmetric matrix), and $\vec{\alpha}_i$, $\vec{\beta}_i$ are vectors of length L_1. The explicit form of A and B for $L_1 = 4$ is

$$A = 2J\begin{pmatrix} -2\alpha & 1 & 0 & 0 \\ 1 & -2\alpha & 1 & 0 \\ 0 & 1 & -2\alpha & 1 \\ 0 & 0 & 1 & -2\alpha \end{pmatrix}, \qquad B = 2J\begin{pmatrix} 0 & 1 & 0 & 0 \\ -1 & 0 & 1 & 0 \\ 0 & -1 & 0 & 1 \\ 0 & 0 & -1 & 0 \end{pmatrix}, \tag{2.32}$$

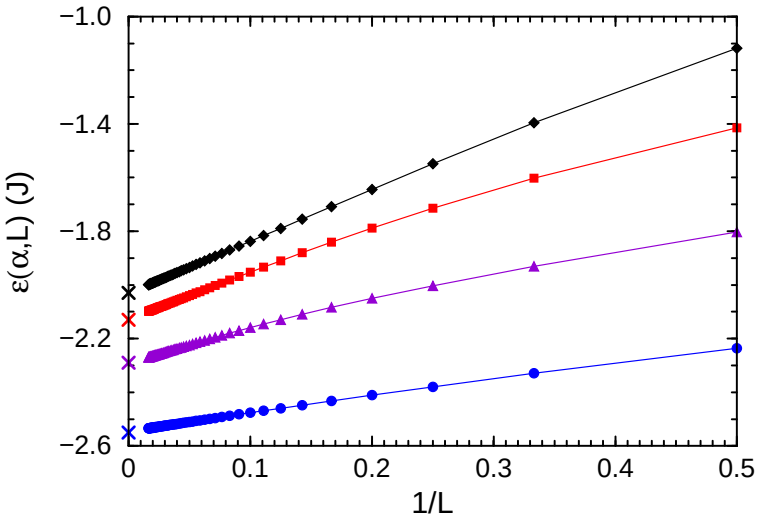

Figure 2.4: Ground state energies per site $\varepsilon(\alpha, L_1)$ for the QIM on open chains (2.7) as functions of inverse chain's length $1/L_1$ (for $2 \leq L_1 \leq 61$) plotted for $\alpha = 1,\ 3/4,\ 1/2$ and $1/4$, from bottom to top. Linear fit gives the asymptotic values of energies for $L_1 \to \infty$, indicated by crosses; these are: $\varepsilon(\alpha, L_1 \to \infty) = -2.55J,\ -2.29J,\ -2.13J$ and $-2.03J$ for the respective values of α.

which can be simply generalized to the case of any finite L_1. The spectrum of $\mathcal{H}(\alpha, L_1)$ can be now determined by a numerical diagonalization of the $2L_1 \times 2L_1$ matrix from Eq. (2.31). For each L_1 one obtains a set of $2L_1$ eigenvalues symmetric around zero. Only the positive ones are the excitation energies E_i appearing in Eq. (2.29). Therefore, the ground state energy $E_0(\alpha, L_1)$ is obtained in absence of any excited states, so the energy per site can be easily expressed as

$$\varepsilon(\alpha, L_1) = \frac{1}{L'} E_0(\alpha, L_1) = -\frac{1}{2L'} \sum_{i=1}^{L'} E_i(\alpha, L_1) \ . \tag{2.33}$$

Fixing α and increasing L_1 we can trace the dependence of $\varepsilon(\alpha, L_1)$ on the system size and make an extrapolation to an infinite chain by considering $L_1 \to \infty$. Results for $\varepsilon(\alpha, L_1)$ (2.33) as a function of decreasing $1/L_1$, obtained for $\alpha = 1, 3/4, 1/2, 1/4$ and L_1 changing from 2 to 61, are shown in Fig. 2.4. The energies decrease with increasing L_1 which suggests that the ground state corresponds indeed to a closed chain without any defects, as presented in Sec. 2.1.2.

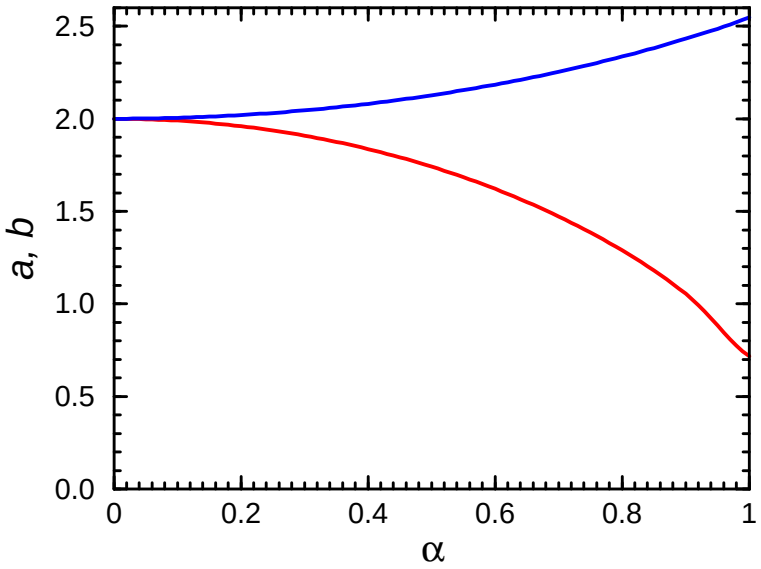

Figure 2.5: Coefficients $a(\alpha)$ (red line) and $b(\alpha)$ (blue line) of the linear fit (2.34) performed using the data for $L_1 = 60$ and $L_1 = 61$ for different values of α. At $\alpha = 0$ one recovers the classical values of the Ising chain.

The dependence of $\varepsilon(\alpha, L_1)$ on $1/L_1$ seems to be almost linear in each case. This is almost exact for $\alpha = 1$ and for $\alpha = 1/4$, while it holds approximately for intermediate values of α in the regime of sufficiently large L_1. This observation can be used to derive a simple, approximate formula for the energy $\varepsilon(\alpha, L_1)$. One can take the values of $\varepsilon(\alpha, L_1)$ obtained for two largest L_1 ($L_1 = 60, 61$) with fixed α and perform a linear fit. Hence, we get

$$\varepsilon(\alpha, L_1) \cong a(\alpha)\,\frac{1}{L_1} - b(\alpha)\ , \tag{2.34}$$

with coefficients a and b depending on α. These new functions can be determined numerically for α changing between 0 and 1 with sufficiently small step. Results obtained by a numerical analysis are plotted in Fig. 2.5. Both a and b starts from a value 2 at $\alpha = 0$, then $a(\alpha)$ decreases monotonically to about 0.72 while $b(\alpha)$ slightly increases to 2.55 at $\alpha = 1$. Eq. (2.34) is exact for $\alpha = 0$ and any L_1, as well as for $L_1 = 60, 61$ and any α. Nevertheless, looking at Fig. 2.4, one can expect it to be a good approximation in case of sufficiently large L_1. From this formula one can read that for $L_1 \to \infty$ one gets for the total energy $E_0(\alpha, L_1) = -L_1 b(\alpha) + O(L_1^0)$ which agrees with the classical intuition based on extensiveness of the internal energy.

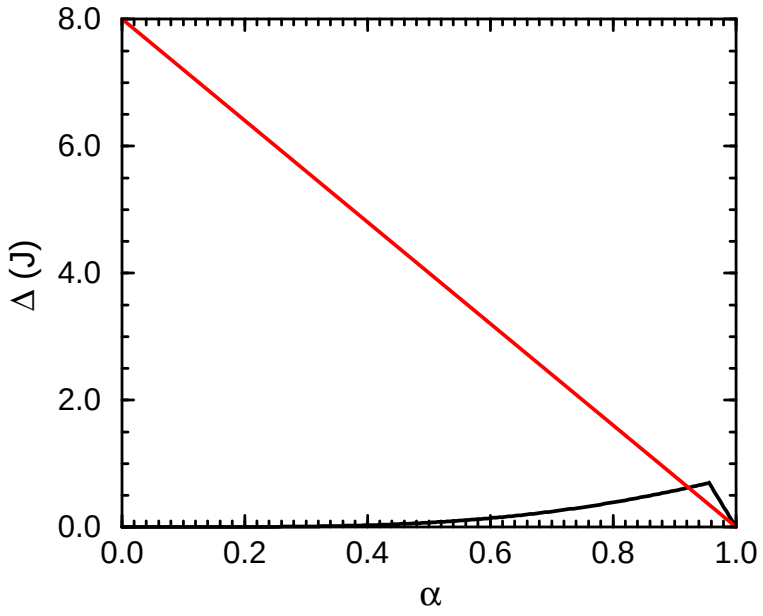

Figure 2.6: Excitation energy $\Delta(J)$ as a function of α for: (i) a ladder with $L = 4$ rungs (black line) and (ii) an infinite ladder (red line). In the first case, as long as the QPT is not approached, the excited state remains in the ground state subspace with $r_i \equiv -1$ and contains one Bogoliubov quasiparticle with $k = \pi$. The latter excited state collapses to the ground state for $L = \infty$, so the first excitation is here different than the one for infinite L. On the contrary, the excited state for $L = \infty$ contains two Bogoliubov quasiparticles with $k = 0^{\pm}$. This leads to the linear gap following $\Delta(\alpha) = 8J(1 - \alpha)$.

Lowest energy excitations

As we pointed out in Sec. 2.1.2, the lowest excited state in the case of a finite system, for α far enough from $\alpha = 1$, is simply $\gamma_{\pi}^{\dagger}|0_+\rangle$ and belongs to the subspace $r_i \equiv -1$. This is a collective excitation creating a wave of spin–flips in the ground state. Close to $\alpha = 1$ one finds that the lowest excited state is the ground state from the subspace $r_i \equiv 1$ which means that the spin order along the rungs changes from AF to FM one along the z–th axis.

The lowest energy excitation changes qualitatively in the thermodynamic limit $L \to \infty$, where $\gamma_{\pi}^{\dagger}|0_+\rangle$ and $|0_+\rangle$ states have the same energy and the dominating excitation is a pair of Bogoliubov quasiparticles with $k = 0^{\pm}$ which corresponds to flipping one spin at $\alpha = 0$. The first excited state remains in the $r_i \equiv -1$ subspace for all α and the gap follows linear law $\Delta(\alpha) = 8J(1-\alpha)$, see Fig. 2.6. This shows that the low energy spectrum of the ladder is the same as for ordinary QIM in the thermodynamic limit ($L \to \infty$). Note that such behavior is

in sharp contrast with the case of finite ladder of $L = 4$ rungs.

2.1.3 Canonical ensemble for the ladder

Partition function

In order to construct the partition function of spin ladder (2.1), we shall analyze its quantum states in different subspaces. Every invariant subspace introduced in Sec. 2.1.1 is labeled by a string $r_1 r_2 \cdots r_L$. Let us consider an exemplary string of the form

$$1\ 1\ 1\ \bar{1}\ 1\ \bar{1}\ 1\ 1\ \bar{1}\ \bar{1}\ \bar{1}\ 1\ 1\ \bar{1}\ 1\ 1\ 1\ 1\ \bar{1}\ \bar{1}\ \bar{1}\ 1\ , \tag{2.35}$$

where $\bar{1} = -1$, and either $r_i = r_{i+1}$ or $r_i \neq r_{i+1}$. Each time when $r_i = r_{i+1}$ the chain continues, and when $r_i \neq r_{i+1}$ we may say that a kink occurs at site i in the chain. We introduce a PBC, so the string is closed to a loop and r_N stands next to r_1. From the point of view of the reduced Hamiltonian $\mathcal{H}_{r_1 r_2 \cdots r_L}$, given by Eq. (2.5), it is useful to split the string $\{r_i\}$ into chains and kinked areas. A chain is a maximal sequence of r_i's without any kinks consisting of at least of two sites. Kink areas are the intermediate areas separating neighboring chains. Using these definitions we can divide our exemplary string (2.35) as follows

$$1\ 1\ 1)\ \bar{1}\ 1\ \bar{1}\ (1\ 1)\ (\bar{1}\ \bar{1}\ \bar{1})\ (1\ 1)\ \bar{1}\ (1\ 1\ 1\ 1)\ (\bar{1}\ \bar{1}\ \bar{1})\ (1\ , \tag{2.36}$$

where we adopt the convention to denote chains as $(r_i r_{i+1} \cdots r_{i+p})$, and kink areas as $)r_i r_{i+1} \cdots r_{i+q}($. For any string of r_i's containing m chains we can define chain configuration $\{L_i\}$ with $i = 1, 2, \ldots, m$, where L_i's are the lengths of these chains put in descending order. In case of our exemplary string its chain configuration is $\{4, 4, 3, 3, 2, 2\}$- note the PBC. Variables $\{L_i\}$ must satisfy three conditions: (i) $L_i \geq 2$ for all i, (ii) $\sum_{i=1}^{m} L_i \leq L$, and (iii) $\prod_{i=1}^{m} (-1)^{L_i} \equiv (-1)^m$. The first two of them are obvious, while the last one is a consequence of the PBC. Using chain parameters the effective Hamiltonian $\mathcal{H}_{r_1 r_2 \cdots r_L}$ can be written as a sum of commuting operators

$$\mathcal{H}_{r_1 r_2 \cdots r_L}(\alpha) = \sum_{i=1}^{m} \mathcal{H}(\alpha, L_i) - 2J\alpha \sum_{i=1}^{K} \tau_i^x + 2JC_{\vec{r}}(\alpha)\ , \tag{2.37}$$

where $K = L - \sum_{i=1}^{m} L_i$ stands for the total size of kinked areas. This formula refers to all subspaces excluding those with $r_{i+1} \equiv r_i$, where we have already obtained exact solutions.

The evaluation of the constant $C_{\vec{r}}(\alpha)$ can be completed by considering chain and kink areas in each subspace, see Appendix A. Having the diagonal form of $\mathcal{H}(\alpha, L_1)$, given by Eq. (2.29), one can now calculate partition function for the ladder of $2L$ spins. It can be written as follows

$$\mathcal{Z}(\alpha) \;=\; \sum_{\{L_i\}} \sum_{R_{\{L_i\}}} F_\alpha[\{L_i\}, R_{\{L_i\}}] e^{-2JC_{\vec{r}}/T} Z(\alpha, \{L_i\}) + Z_0(\alpha) \;, \tag{2.38}$$

where the sum over all $\{\vec{r}\}$ subspaces is replaced by sums over all chain configurations $\{L_i\}$ and all $R = \sum_{i=1}^{L} r_i$ configurations possible for a given $\{L_i\}$. Factor $F_\alpha[\{L_i\}, R_{\{L_i\}}]$ is a number of $\vec{r}$ subspaces for fixed chain configuration and fixed R when $\alpha < 1$, and for $\alpha = 1$ it is a number of $\vec{r}$ subspaces when only $\{L_i\}$ is fixed. Partition function for any subspace containing open QIM chains or kinked areas is given by

$$Z(\alpha, \{L_i\}) \;=\; 2^L \cosh^K \left[\frac{2J}{\alpha T}\right] \times \prod_{i=1}^{n} \prod_{j=1}^{l_i} \cosh^{N(l_i)} \left[\frac{E_j(\alpha, l_i)}{2T}\right] \;, \tag{2.39}$$

where $\{l_i\}$ $(i = 1, 2, \ldots, n)$ are the different lengths of the chains appearing in the chain configuration $\{L_i\}$, $N(l_i)$ stands for the number of chains of the length l_i, and T is temperature in units of $k_B = 1$. For example, the chain configuration $\{4, 4, 3, 3, 2, 2\}$ of Eq. (2.36) has $n = 3$, $\{l_i\} = \{4, 3, 2\}$ and $N(l_i) \equiv 2$. The term $Z_0(\alpha)$ is a contribution from subspaces with $r_{i+1} \equiv r_i$. Using exact solutions (2.18), available in these subspaces, one finds that

$$Z_0(\alpha) \;=\; \cosh\left[\frac{2J}{T} L(1-\alpha)\right] \times \sum_{S=\pm 1} \left(\prod_{q=0}^{L-1} \cosh \frac{E_q^S}{T} + S \prod_{q=0}^{L-1} \sinh \frac{E_q^S}{T} \right), \tag{2.40}$$

where the quasiparticle energies are:

$$E_q^+ \;=\; 2J \left\{ 1 + \alpha^2 + 2\alpha \cos\left(\frac{2q+1}{L}\pi\right) \right\}^{1/2}, \tag{2.41}$$

$$E_q^- \;=\; 2J \left\{ 1 + \alpha^2 + 2\alpha \cos\left(\frac{2q+1}{L}\pi + \frac{1}{L}\pi\right) \right\}^{1/2}. \tag{2.42}$$

Appearance of both sine and cosine hyperbolic functions in Z_0 (2.40) is due to the projection operators $\mathcal{P}$ introduced in section 2.1.2.

Combinatorial factor

To obtain numerical values of the partition function one has to get the explicit form of the combinatorial factor $F_\alpha[\{L_i\}, R_{\{L_i\}}]$. This can be done in a simple way only for $\alpha = 1$ when $C_{\vec{r}}(\alpha) = 0$, see Eq. (2.6). Then we have

$$F_{\alpha=1}[\{L_i\}, R_{\{L_i\}}] \equiv F_1[\{L_i\}] \ , \tag{2.43}$$

where $F_1[\{L_i\}]$ is the number of different $\vec{r}$ subspaces that can be obtained from a fixed chain configuration $\{L_i\}$. Now we can derive a formula for this combinatorial factor.

The chains can be put into the r_i string in any order and these of equal length are indistinguishable. Apart from chains, there are also r_i's belonging to the kinked areas which determine the actual string configuration. We have $K = L - \sum_{i=1}^{m} L_i$ of them, they are indistinguishable and can be distributed among m kinked areas. These degrees of freedom lead to a combinatorial factor

$$\frac{m!}{N(l_1)! \ldots N(l_n)!} \left(\begin{array}{c} K+m-1 \\ K \end{array} \right), \tag{2.44}$$

where $l_1, l_2, \ldots, l_n$ $(n \leq m)$ are the lengths of the chains without repetitions and $N(l_i)$ is a number of chains of the length l_i. After determining the length of the first chain L_1 and the size of its kink area A_1, we still need to fix the position of r_1. We have exactly $L_1 + A_1$ possibilities. Next, we have to sum up over all possible values of L_1 (which are $l_1, l_2, \ldots, l_n$), all possible sizes of the kink area A_1 (which are $1, 2, \ldots, K$) and multiply by a combinatorial factor (2.44) calculated for the remaining part of the string. The result is

$$F_1[\{L_i\}] \ = \ 2 \sum_{i=1}^{n} N(l_i) \frac{(m-1)!}{N(l_1)! \ldots N(l_n)!} \times \sum_{a=0}^{K} (l_i + a) \left(\begin{array}{c} K-a+m-2 \\ K-a \end{array} \right), \tag{2.45}$$

where the factor of 2 in front comes from the fact that $r_1 = \pm 1$. This number tells us how many times a given energy spectrum repeats itself among all subspaces when $\alpha = 1$. The binomial factor appearing in formula (2.45) needs to be generalized with Γ functions when $m = 1$ which gives:

$$\left(\begin{array}{c} K-a-1 \\ K-a \end{array} \right) \equiv \delta_{K,a}. \tag{2.46}$$

2.1.4 Compass ladder at finite temperature

Correlation functions and chain fragmentation

NN correlation functions can be easily derived at finite temperature from the partition function $\mathcal{Z}(\alpha,\beta,\gamma)$, if we substitute our initial Hamiltonian $\mathcal{H}(\alpha)$ given by Eq. (2.1) by

$$\mathcal{H}(\alpha,\beta,\gamma) = 2J\sum_{i=1}^{L}\left\{\gamma\sigma_{2i-1}^{x}\sigma_{2i}^{x} + (1-\alpha)\sigma_{2i-1}^{z}\sigma_{2i}^{z}\right\} + J\beta\sum_{i=1}^{L}\left(\sigma_{2i-1}^{z}\sigma_{2i+1}^{z} + \sigma_{2i}^{z}\sigma_{2i+2}^{z}\right) . \quad (2.47)$$

Then, after calculating the partition function, we recover spin correlations by differentiating $\mathcal{Z}(\alpha,\beta,\gamma)$ with respect to β and γ, and inserting $\gamma=\alpha$ and $\beta=1$ to the obtained correlations to derive the final results. Once again, this can be done in a simple way for small ladders. Correlation functions $\langle\sigma_{2i-1}^{x}\sigma_{2i}^{x}\rangle$ and $\langle\sigma_{2i-1}^{z}\sigma_{2i+1}^{z}\rangle$ for spin ladder (2.1) at $\alpha=1$ (quantum compass ladder) are shown in Fig. 2.7 for increasing temperature T. Other NN correlations vanish at $\alpha=1$ for trivial reasons.

Fig. 2.7 shows the qualitative difference between correlation functions of spin ladder (2.1) and those of periodic QIM chain (2.8) of length L, that appears in the ground subspaces $r_i \equiv r_{i+1}$. When all the subspaces are considered, thermal fluctuations gradually destroy the spin order along the legs and the $\langle\sigma_{2i-1}^{z}\sigma_{2i+1}^{z}\rangle$ correlations weaken. On the contrary, the $\langle\sigma_{2i-1}^{x}\sigma_{2i}^{x}\rangle$ correlations on the rungs are robust in the entire range of physically interesting temperatures $0<T<2J$, as the ZZ interactions destroying them are gradually suppressed with increasing T due to the increasing size of kinked areas.

The above result is qualitatively different from the QIM results shown by dashed lines in Fig. 2.7, where thermal fluctuations initially increase intersite correlations of z–th spin components along the ladder legs and reduce the influence of the transverse field acting on τ_i^x pseudospins due to spin interactions $2J\sigma_{2i-1}^{x}\sigma_{2i}^{x}$ on the rungs. In the latter case the low-temperature thermal fluctuation can enhance local spin ZZ correlations along the ladder legs at the cost of disorder in the direction of external field. This is because pseudospin interaction involves τ_i^z operators, not τ_i^x ones. Remarkably, in the full space, see solid lines in Fig. 2.7, the spin correlations are initially the same (at low T) as those for the QIM, but this changes when temperature $T\simeq 0.3J$ is reached and the two curves cross — then the rung correlations start to dominate. The crossing is caused by the growth of the kinked areas, as shown in Fig. 2.8, which are free of quantum fluctuations and therefore favor rung correlations of x–th spin components.

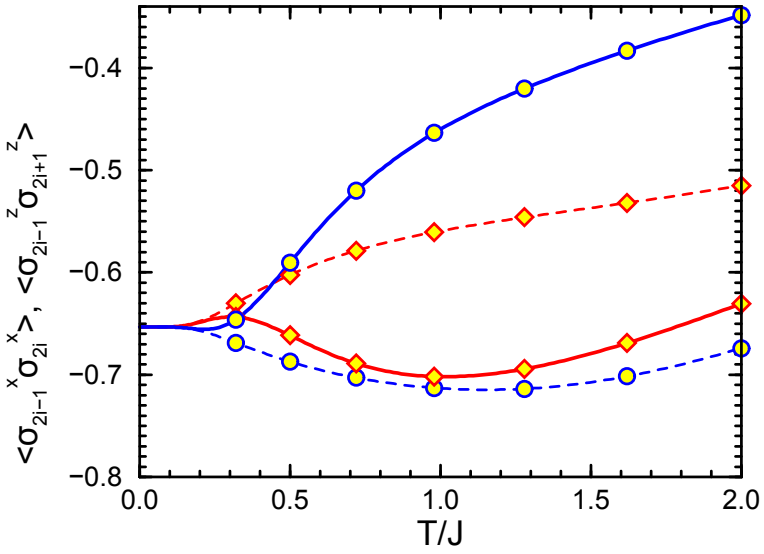

Figure 2.7: Nearest-neighbor correlation functions, $\langle \sigma^x_{2i-1}\sigma^x_{2i}\rangle$ on the rungs (diamonds and red lines) and $\langle \sigma^z_{2i-1}\sigma^z_{2i+1}\rangle$ along the ladder legs (circles and blue lines), calculated for the compass ladder ($\alpha = 1$) of $2L = 8$ spins for increasing temperature T, taking into account: (i) all subspaces (solid lines) for increasing temperature T, and (ii) only the subspace which contains the ground state $r_i \equiv -1$ (dashed lines).

Another interesting information on excitations in the quantum compass ladder is the evolution of the average chain configuration with increasing temperature. As we know from Sec. 2.1.3, every subspace can be characterized by the lengths of chains that appear in its r_i label. Chain configurations can in turn be characterized by: (i) the number of chains which are separated by kinks m, and (ii) the total size of kinked areas K. Thermodynamic averages of both quantities, $\langle m\rangle$ and $\langle K\rangle$, can be easily determined at $\alpha = 1$ even for a relatively large system using the combinatorial factor $F_1[\{L_i\}]$ (2.45) calculated in Sec. 2.1.3. In the limit of $T \to \infty$ one has:

$$\langle m\rangle_\infty = \frac{\sum_{\{L_i\}} F_1[\{L_i\}]\left(L - \sum_{j=1}^m L_j\right)}{\sum_{\{L_i\}} F_1[\{L_i\}]}, \tag{2.48}$$

$$\langle K\rangle_\infty = \frac{\sum_{\{L_i\}} F_1[\{L_i\}] m[\{L_i\}]}{\sum_{\{L_i\}} F_1[\{L_i\}]}, \tag{2.49}$$

where $m[\{L_i\}]$ is the number of $\{L_i\}$ in the chain configuration $L_1, L_2, \cdots, L_m$.

In Fig. 2.8 we show the average quantities $\langle m\rangle$ and $\langle K\rangle$ for ladders of $2L = 8$ (left) and

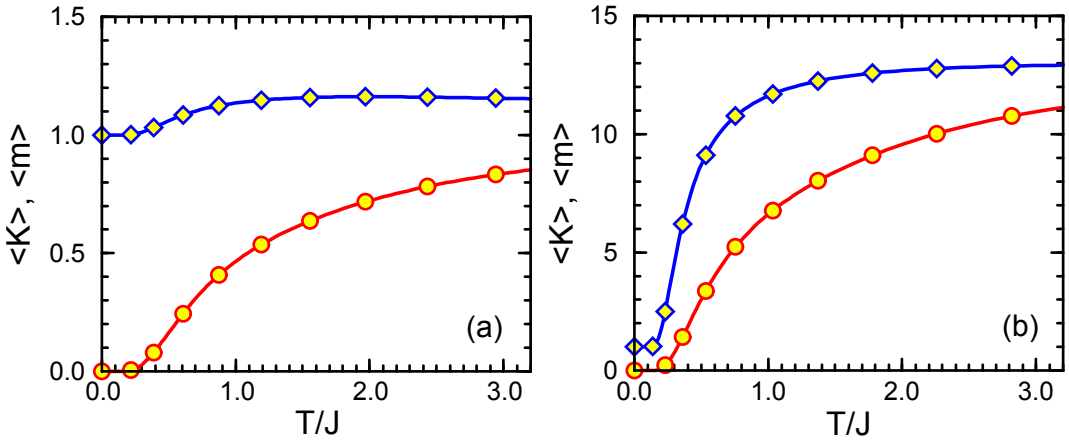

Figure 2.8: Average size of the kinked areas $\langle K\rangle$ (2.49) (circles and red lines) and the average number of chains $\langle m\rangle$ (2.48) (diamonds and blue lines) for the quantum compass ladder (2.1) (at $\alpha = 1$) consisting of: (a) $2L = 8$, and (b) $2L = 104$ spins. The mean size of kinked areas $\langle K\rangle$ increases monotonically with increasing temperature T to the asymptotic value $L/4$, see Eq. (2.50). The average number of chains $\langle m\rangle$ behaves differently, growing quickly to a maximal value at intermediate T and then decreasing slowly when $T \to \infty$ towards: (a) 1.125, and (b) $13 + 12 \times 10^{-15}$.

$2L = 104$ spins (right). In both cases the average number of chains $\langle m\rangle$ starts from 1 and the average size of the kinked areas $\langle K\rangle$ starts from 0, corresponding to a single chain without kinks in the ground state at $T = 0$. The number of chains $\langle m\rangle$ grows to a broad maximum in the intermediate temperature range and decreases asymptotically to a finite value. This non–monotonic behavior is due to the fact that the states with the highest energy, which become accessible when $T \to \infty$, do not belong to the subspaces with large number of chains. The mean value of kinks $\langle K\rangle$ follows $\langle m\rangle$ but increases monotonically in the entire range of T, and for finite T one finds that $\langle K\rangle < \langle m\rangle$. By looking at the current results one may deduce that in case of $T \to \infty$ and for large $L \gg 1$ both quantities approach

$$\langle m\rangle_\infty = \langle K\rangle_\infty = \frac{L}{4}\,. \tag{2.50}$$

This is an interesting combinatorial feature of the chain configurations which is not obvious when we look at the explicit form of the combinatorial factor $F_1[\{L_i\}]$ (2.45). Note that Eq. (2.50) gives an integer due to our choice of system sizes $2L$ considered here, being multiplicities of 8, i.e., L is a multiplicity of 4.

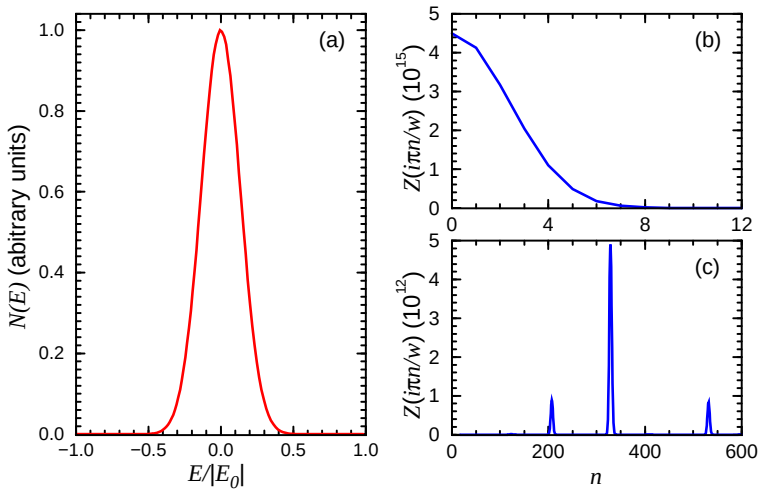

Figure 2.9: Relative density of states $N(E)$ (a) as a function of energy ratio E/E_0 and Fourier coefficients $\mathcal{Z}\left(2i\pi\frac{n}{w}\right)$ as functions of n for $0 \leq n \leq 12$ (b) and for $13 \leq n \leq 600$ (c) calculated for the ladder of $2L = 104$ spins. Relative density of states reminds a gaussian centered in zero with the width being roughly 0.15 of the spectrum width w. This follows from the gaussian behavior of $\mathcal{Z}\left(i2\pi\frac{n}{w}\right)$ coefficients for small n (panel (b)). Plot (c) reveals peaks in $\mathcal{Z}\left(i2\pi\frac{n}{w}\right)$ for $n = 208, 330, 533$, three order of magnitude weaker than for $n = 0$, corresponding with periodic condensations of the energy levels every $\Delta E = 1.28, 0.81, 0.50J$.

Spectrum of a large system

The combinatorial factor $F_1[\{L_i\}]$ given by Eq. (2.45) enables us to calculate the partition function $\mathcal{Z}(1)$ (2.38) for a large system when $\alpha = 1$. As a representative example we consider a ladder consisting of $2L = 104$ spins. Even though we can reduce Hamiltonian (2.1) to a diagonal form when $2L = 104$, as shown in previous paragraphs, it is still impossible to generate the full energy spectrum for practical reasons — simply because the number of eigenstates is too large. Instead, we can obtain the density of states in case of $\alpha = 1$ using the known form of the partition function (2.38) and of the combinatorial factor (2.45). Partition function for imaginary $1/T$ can be written as

$$\mathcal{Z}(ix) = \sum_{p=0}^{4^L-1} e^{-ixE_p} = \int_{E_0-\varepsilon}^{-E_0+\varepsilon} dE e^{-ixE}\rho(E) \ , \tag{2.51}$$

where

$$\rho(E) \equiv \sum_{p=0}^{4^L-1} \delta(E - E_p) \ , \tag{2.52}$$

and where sum is over all eigenenergies E_p of the ladder. Parameter E_0 is the energy of the ground state. Small and positive ε is introduced to formally include $\pm E_0$ into integration interval. Here we used the fact that ladder's spectrum is symmetric around zero at the compass point $\alpha = 1$ (see Fig. 2.2). Function $\rho(E)$ can be easily recognized as the density of states.

Using $x = 2\pi n/w$ in Eq. (2.51), with $w = 2(|E_0| + \varepsilon)$ standing for the length of the integration interval and n being integer, we easily recover the density of states $\rho(E)$ (2.52) in a form of the Fourier cosine expansion

$$\rho(E) = \frac{2}{w} \sum_{n=1}^{\infty} \mathcal{Z}\left(2i\pi\frac{n}{w}\right) \cos\left(2\pi\frac{n}{w}E\right) + \frac{1}{w}\mathcal{Z}(0) \ , \tag{2.53}$$

with amplitudes given by the partition function $\mathcal{Z}(ix)$.

In practice we cannot execute the sum above up to infinity. Therefore, it is convenient to define $\rho_c(E)$ which is given by the same Eq. (2.53) as $\rho(E)$ but where the sum has a cutoff for $n = c$. The heights of peaks in $\rho_c(E)$ are expected to grow in an unlimited way with increasing value of c, so it is convenient to define the normalized density of states $N(E)$ as

$$N(E) = \rho_c(E)/\rho_c(0) \ . \tag{2.54}$$

The results for the compass ladder ($\alpha = 1$) of $2L = 104$ spins are shown in Fig. 2.9. These are relative density of states $N(E)$ for cutoff $c = 600$ and Fourier coefficients $\mathcal{Z}\left(2i\pi\frac{n}{w}\right)$ for two intervals of n. Results obtained for lower cutoffs show that the overall gaussian shape of $N(E)$, shown in Fig. 2.9(a), does not change visibly if only $c > 8$. This allows us to conclude that the spectrum of the compass ladder becomes continuous when the size of the systems increases which is not the case for the Ising ladder ($\alpha = 0$). Higher values of n are investigated to search for more subtle effects than gaussian behavior of $N(E)$. These are found by looking at the amplitudes $\mathcal{Z}\left(2i\pi\frac{n}{w}\right)$ in high n regime [Fig. 2.9(c)], as the low n regime [Fig. 2.9(b)] encodes only the gaussian characteristic of the spectrum. One finds three sharp maxima of the amplitudes for $n = 208, 330, 533$ out of which the one with $n = 330$ has about five times higher intensity than the rest, but it is still 10^3 times weaker than the peak in $n = 0$. These values of n correspond with some periodic condensations of the energy levels

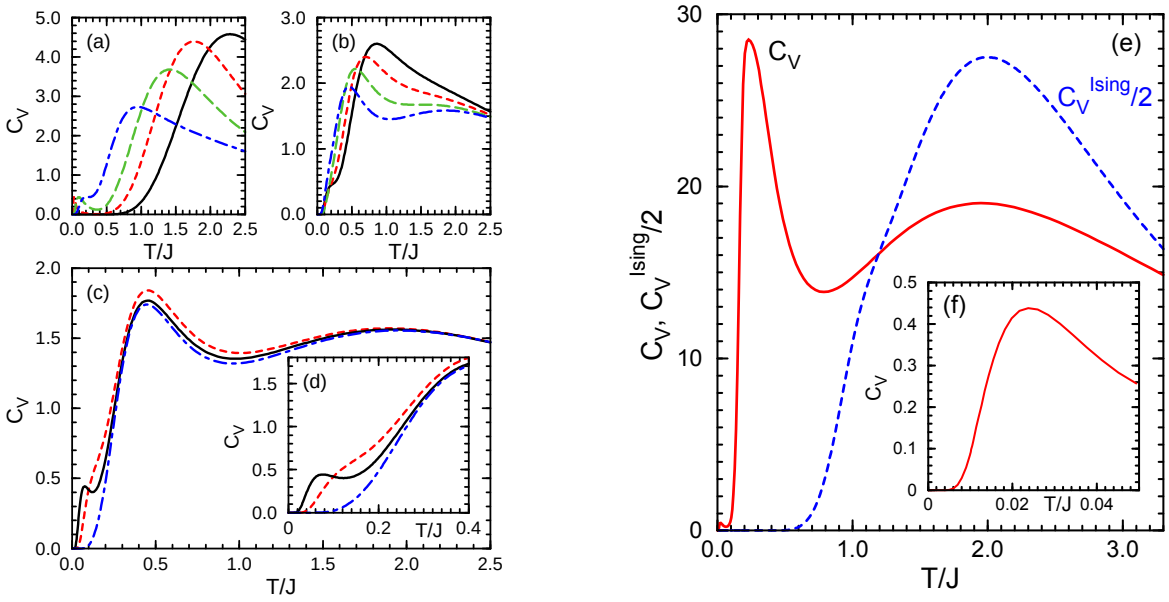

Figure 2.10: Panels (a)–(d): Evolution of heat capacity C_V for spin ladder (2.1) of $2L = 8$ spins, shown in Fig. 2.1, with increasing parameter α, equal to: (a) $\alpha = 0.00, 0.49, 0.69, 0.85$, (b) $\alpha = 0.87, 0.90, 0.94, 0.97$, and (c) $\alpha = 0.982, 0.988, 1.000$. In panels (a) and (b) lines from right to the left (black, red, green and blue) correspond with growing α. In panels (c) and (d) the values of C_V for growing α are shown by red, black and blue lines, respectively. Panel (d) shows the low temperature data of panel (c) with increased resolution. Panels (e)–(f): heat capacity C_V for the compass ladder of $2L = 104$ spins at $\alpha = 1$ as a function of temperature T (red line). Blue line shows heat capacity of the Ising ladder ($\alpha = 0$) of the same size.

with periods $\Delta E = 1.28, 0.81, 0.50J$ respectively which are visible in $N(E)$ only in vicinity of $E = \pm E_0$.

2.1.5 Heat capacity

From Ising to compass model

In this Section we analyze heat capacity to identify characteristic excitation energies in the compass ladder. We begin with complete results for the ladder consisting of $2L = 8$ spins shown in Fig. 2.1, where all chain configurations can be written explicitly. Using Eq. (2.38) for the partition function, one can next calculate all thermodynamic functions including average internal energy and the heat capacity.

Results for the heat capacity C_V for different values of α are shown in Fig. 2.10. These plots cover three characteristic intervals of α where the behavior of curves changes qualita-

tively by appearance or disappearance of certain maxima. The positions of these maxima correspond to possible excitation energy scales of the system that change at increasing α and their intensities reflect the number of possible excitations in a given energy interval. In case of $\alpha = 0$– Fig. 2.10(a), we see a single maximum at $\sim 2.2J$ which corresponds to flipping spins in an Ising spin ladder (or in a two-level system). Switching on the XX interactions and weakening the ZZ interactions on the rungs has two effects: (i) decreasing energy and intensities of the high–energy maximum, and (ii) appearance of a low–energy mode in every subspace with QIM chains which manifests itself as a peak with low intensity at low temperature T, see Fig. 2.10(a). At $\alpha \simeq 0.85$ this mode overlaps with modes of higher energies and until $\alpha \simeq 0.94$ there is a single peak again with a shoulder at high values of T, shown in Fig. 2.10(b). Then the excitation energies separate again and a broad peak appears for high T accompanied by a distinct maximum at $T \simeq 0.4J$.

In Fig. 2.10 we recognize the characteristic features for the QIM chains present in most of the subspaces which are influenced by the excitations mixing different subspaces. If we had only one subspace with $r_i \equiv -1$, i.e., the one containing the ground state, then we would have two maxima in C_V for all $0 \leq \alpha \leq 1$ — one of low intensity in the regime of low temperature T, and another one at high T, broad and intense. The small maximum corresponds with low–energy mode of QIM that disappears for certain $\alpha > 1$. This is not the case for other subspaces where QIM chains are fragmented and kinked areas are formed. In case of the $1\bar{1}\bar{1}\bar{1}$ subspace the low–energy peak in C_V vanishes at $\alpha \simeq 0.65$ and the high-energy peak persists and moves to higher temperatures with the increase of α. The situation is similar for the $11\bar{1}\bar{1}$ subspace but the peak disappears at $\alpha \simeq 0.75$ and in the classical subspace $1\bar{1}1\bar{1}$ we have only one maximum for any α. One can deduce now that the general rule is that the separation of peaks in heat capacity is reduced primarily by the growth of kinked areas and secondarily by the fragmentation of chains. This separation of energy scales is also visible in Fig. 2.2 where the spectra in different subspaces are shown; below certain α in all cases but (d), which is the classical subspace, the energy gap between the ground state and first excited state is smaller than other energy gaps appearing in the subspace.

The mixing of different subspaces in the partition function makes the peaks in C_V overlap which can result in reducing their number. This happens in Fig. 2.10(b); for solid ($\alpha = 0.87$) and dashed ($\alpha = 0.90$) curve we have only one maximum. For higher or lower α the energy scales remain separated which is due to fact that: (i) soft modes survive in most of subspaces for low α, and (ii) for high α the high–energy modes become even more robust and do not overlap with soft modes still present in subspaces with small kinked areas. The

last phenomenon characteristic for the ladder are excitations between $r_i \equiv -1$ and $r_i \equiv 1$ subspace in the vicinity of the QPT. This yields to the appearance of the new energy scale $\Delta(\alpha) = 4LJ(1-\alpha)$ at $\alpha \simeq 0.987$ which manifests itself as a small peak in heat capacity in low temperature. This maximum vanishes at $\alpha = 1$, as shown in Fig. 2.10(d).

Generic features at large L

After understanding the heat capacity in a small system of $L = 8$ spins (Sec. 2.1.5), we analyze a large system using the statistical analysis of Sec. 2.1.3. It is difficult to obtain a combinatorial factor $F_\alpha[\{L_i\}, R_{\{L_i\}}]$ in case of $\alpha < 1$ and likely even impossible in a general way without fixing L. Hence we focus on the compass ladder ($\alpha = 1$). For the compass ladder of $2L = 104$ spins considered in Sec. 2.1.4, one finds 2^{52} invariant subspaces. Although the eigenvalues can be found in each subspace, it is not possible to sum up over all subspaces for practical reasons and a statistical analysis is necessary. Therefore, the knowledge of the combinatorial factor $F_1[\{L_i\}]$, see Eq. (2.45), is crucial to calculate the partition function $\mathcal{Z}(1)$ (2.38). Fortunately, knowing it we only need to consider different chain configurations which are not very numerous — there are only 140854 of them. This means that on average each energy spectrum of the effective Hamiltonian repeats itself almost 32×10^9 times throughout all subspaces.

The statistical analysis of the compass ladder consisting of $2L = 104$ spins in terms of: (i) mean values of kinked areas $\langle K \rangle$ (2.49), and (ii) the number of chains $\langle m \rangle$ (2.48), was already presented in Fig. 2.8(b), while the energy spectrum was discussed in Sec. 2.1.4. Here we present the heat capacity C_V for the compass ladder of this size in Fig. 2.10 (e). At high temperature one finds a broad maximum centered at $T \simeq 2J$ which originates from dense excitation spectrum at the compass point ($\alpha = 1$), cf. the spectrum of the compass ladder with $2L = 8$ spins shown in Fig. 2.2. We remark that the broad maximum of Fig. 2.10 (e) has some similarity to broad maxima found in the specific heat (heat capacity) of spin glasses [71]. However, here the broad maximum in the heat capacity does not originate from disorder but solely indicates frustration, similar as in some other models with frustrated spin interactions [72]. We emphasize that the present results could be obtained only by developing a combinatorial analysis of a very large number of possible configurations of spin ladder, and due to the vanishing constant $C_{\vec{r}}(\alpha = 1) = 0$ (2.6) in the energy spectrum for the compass ladder. Unfortunately, the present problem is rather complex due to the quantum nature of spin interactions, but in case of the binomial 2D Ising spin glass an exact algorithm to

compute the degeneracies of the excited states could be developed recently [73].

The heat capacity C_V of Fig. 2.10 (f) at low temperature is qualitatively similar to the one obtained for $2L = 8$ spins, see Fig. 2.10(c), but the steep maximum at low T is here moved to lower temperature $T \simeq 0.2J$. The main difference between the heat capacity of $2L = 104$ spins and the case of $2L = 8$ spins is a small maximum appearing at very low $T \simeq 0.02J$, see inset. This peak originates from the low–energy modes in subspaces $r_i \equiv r_{i+1}$ which exist in sufficiently long chains described by the QIM. We also identified an additional (third) peak in the regime of rather low temperature $T \simeq 0.02J$ (shown in the inset). This maximum originates from the QIM (2.8) where the energies of the ground state and of the first excited state approach each other for increasing L, if only $\alpha \leq 1$. Thus, this lowest peak in the heat capacity obtained for the compass ladder of $2L = 104$ spins has to be considered as a finite size effect — for increasing system size it is shifted to still lower temperature T, and would thus disappear in the thermodynamic limit $L \to \infty$, in agreement with the qualitative change of low energy spectrum of the QIM.

2.1.6 Summary and conclusions

We have investigated an intriguing case of increasing frustration in a spin ladder (2.1) which interpolates between the (classical) Ising ladder and the frustrated compass ladder when the parameter α increases from $\alpha = 0$ to $\alpha = 1$. The ground state of the ladder was solved exactly in the entire parameter range by mapping to the QIM, and we verified that frustrated interactions on a spin ladder generate a QPT at $\alpha = 1$, when conflicting interactions ZZ along the ladder legs compete with 2XX ones along the rungs. At this point the spin correlations on the rungs $\langle \sigma^z_{2i-1} \sigma^z_{2i} \rangle = -1$ collapses to zero and the ground state becomes disordered. We have shown that the ground state of a finite ladder has then degeneracy 2, while the analysis of the energy spectra for increasing size suggests that the degeneracy increases to 4 in the thermodynamic limit. Note that in this limit $\alpha = 1$ becomes a quantum critical point for the QIM found in the ground subspace and the character of spectrum changes from discrete to continuous.

The present method of solving the energy spectrum in different subspaces separately elucidates the origin of the QPT found in the present spin ladder (2.1) at the point $\alpha = 1$, corresponding to the frustrated interactions in the compass ladder. We argue that this approach could help to find exact solutions in a class of quasi-1D models with frustrated spin interactions, but in some cases only the ground state and not the full spectrum can

be rigorously determined. For instance, this applies to a spin ladder with frustrated spin interactions between different triplet components on the rungs [74], where a first-order QPT with discontinuous spin correlations was found.

By performing a statistical analysis of different possible configurations of spin ladder (2.1) with PBCs we derived a partition function $\mathcal{Z}(\alpha)$ for a mesoscopic system of 104 spins. The calculation involves the classification of ladder subspaces into classes of chain configurations $\{L_i\}$ equivalent by symmetry operations and the determination of the combinatorial factor $F_\alpha[\{L_i\}, R_{\{L_i\}}]$. We have shown that this factor can be easily determined at the compass point ($\alpha = 1$), so the heat capacity of such a mesoscopic compass ladder could be found.

Summarizing, we demonstrated that spin ladder studied in this paper exhibits a QPT from a classical ordered to a quantum disordered ground state which occurs due to the level crossing, and is therefore of first order. It leads to a discontinuous change of spin correlations on the rungs when the interactions along the ladder legs and on the rungs become frustrated. Fortunately, the subspaces which are relevant for the QPT in the compass ladder considered here can be analyzed rigorously, which gives both the energy spectra and spin correlation functions by mapping the ladder on the quantum Ising model. The partition function derived above made it possible to identify the characteristic scales of excitation energies by evaluating the heat capacity for a mesoscopic system.

2.2 Quantum compass model on a square lattice

In this section we will present the study on the 2D QCM model, already introduced in the beginning of this chapter. The section is splitted into two parts: (*i*)– exact properties of the 2D QCM is based on Refs. [75, 76], and (*ii*) numerical studies of the QCM on small square clusters, contains results presented in Refs. [76, 77] together with some new, unpublished results. In the first part we will focus on special symmetries of the planar QCM, giving the spin transformations that bring the Hamiltonian into the block-diagonal (or reduced) form and confirming its self-duality. Next we will derive the equivalence relations between these diagonal blocks (or invariant subspaces) following from the translational invariance of the original QCM Hamiltonian and show the multiplet structure of the invariant subspaces for 4×4, 5×5 and 6×6 lattices. The study of symmetries will end on unveiling the hidden symmetry of the ground state of the QCM and its consequences for the four-point correlation functions using another spin transformation. Finally we will present a non-local MF approach to the QCM on infinite lattice suggested by the form of the reduced Hamiltonian employing

JW transformation, similarly as in Ref. [48]. We argue that such new approach is valuable as it respects the special symmetries of the QCM and leads to non-trivial long-range spin correlation functions.

In the second part of this section we will show the results of exact diagonalization (ED) techniques applied to the QCM for lattices of the sizes up to 6×6. Due to the complexity of the many-body problem this can be regarded as the state–of–the–art implementation of ED. The results include ground-state properties of the QCM such as: spin correlation functions and covariances of the local and non-local type, evolution of the energy levels as a functions of anisotropy, and entanglement entropy of a row in the lattice. Beyond the ground state, we study densities of states and heat capacities of the systems of different sizes in the isotropic point.

2.2.1 Exact properties of the two-dimensional compass model

Block-diagonal Hamiltonian

We consider the anisotropic ferromagnetic QCM for pseudospins 1/2 on a finite $L \times L$ square lattice with PBCs:

$$\mathcal{H}(\alpha) = -J \sum_{i,j=1}^{L} \left\{ (1-\alpha) X_{i,j} X_{i+1,j} + \alpha Z_{i,j} Z_{i,j+1} \right\}, \tag{2.55}$$

where $\{X_{i,j}, Z_{i,j}\}$ stand for Pauli matrices at site (i,j), i.e., $X_{i,j} \equiv \sigma^x_{i,j}$ and $Z_{i,j} \equiv \sigma^z_{i,j}$ components, interacting on vertical and horizontal bonds. The coupling constant J is positive and the sign factor -1 is introduced to provide comparable ground state properties for odd and even systems. In this section we set $J = 1$. Parameter $\alpha \in [0,1]$ changes the anisotropy of vertical and horizontal interactions. In case of L being even, this model is equivalent to the antiferromagnetic QCM. We can easily construct a set of $2L$ operators which commute with the Hamiltonian but anticommute with one another [42]: $P_i \equiv \prod_{j=1}^{L} X_{i,j}$ and $Q_j \equiv \prod_{i=1}^{L} Z_{i,j}$. Below we will use as symmetry operations all $R_i \equiv P_i P_{i+1}$ and Q_j to reduce the Hilbert space; this approach led to the exact solution of the compass ladder [65]. The QCM Eq. (1) can be

written in common eigenbasis of $\{R_i, Q_j\}$ operators using spin transformations of the form:

$$X_{i,j} = \prod_{p=i}^{L} \tilde{X}_{p,j}\,, \qquad \tilde{X}_{i,j} = X'_{i,j-1}X'_{i,j}\,, \tag{2.56}$$

$$Z_{i,j} = \tilde{Z}_{i-1,j}\tilde{Z}_{i,j}\,, \qquad \tilde{Z}_{i,j} = \prod_{q=j}^{L} Z'_{i,q}\,, \tag{2.57}$$

where $\tilde{Z}_{0,j} \equiv 1$ and $X'_{i,0} \equiv 1$. After writing the Hamiltonian $\mathcal{H}(\alpha)$ of Eq. (2.55) in terms of primed pseudospin operators one finds that the transformed Hamiltonian,

$$\mathcal{H}'(\alpha) = -(1-\alpha)H'_x - \alpha H'_z, \tag{2.58}$$

contains no $\tilde{X}_{L,j}$ and no $Z'_{i,L}$ operators so the corresponding $\tilde{Z}_{L,j}$ and $X'_{i,L}$ can be replaced by their eigenvalues q_j and r_i, respectively. The Hamiltonian $\mathcal{H}'(\alpha)$ is dual to the QCM $\mathcal{H}(\alpha)$ in the thermodynamic limit; we give here an explicit form of its x-part:

$$H'_x = \sum_{i=1}^{L-1}\left\{\sum_{j=1}^{L-2} X'_{i,j}X'_{i,j+1} + X'_{i,1} + r_i X'_{i,L-1}\right\} + P'_1 + \sum_{j=1}^{L-2} P'_j P'_{j+1} + rP'_{L-1}, \tag{2.59}$$

and the similar form for the z-part:

$$H'_z = \sum_{j=1}^{L-1}\left\{\sum_{i=1}^{L-2} Z'_{i,j}Z'_{i+1,j} + Z'_{1,j} + s_j Z'_{L-1,j}\right\} + Q'_1 + \sum_{j=1}^{L-2} Q'_i Q'_{i+1} + sQ'_{L-1}, \tag{2.60}$$

where $s_j = q_j q_{j+1}$, $s = \prod_{j=1}^{L-1} s_j$ and $r = \prod_{i=1}^{L-1} r_i$, and new nonlocal $P'_j = \prod_{p=1}^{L-1} X'_{p,j}$ and $Q'_i = \prod_{q=1}^{L-1} Z'_{i,q}$ operators originate from the PBCs. As we can see, the z-part H'_z (2.60) follows from H'_x (2.59) by the lattice transposition, replacing $X'_{i,j} \to Z'_{i,j}$ and $r_i \to s_j = q_j q_{j+1}$. Ising variables r_i and s_j are the eigenvalues of the symmetry operators $R_i \equiv P_i P_{i+1}$ and $S_j = Q_j Q_{j+1}$.

Instead of the initial $L \times L$ lattice of quantum spins, one finds here $(L-1) \times (L-1)$ internal quantum spins with $2(L-1)$ classical boundary spins, which gives $L^2 - 1$ degrees of freedom. The missing spin is related to the Z_2 symmetry of the QCM and makes every energy level at least doubly degenerate. Although the form of Eqs. (2.59, 2.60) is complex,

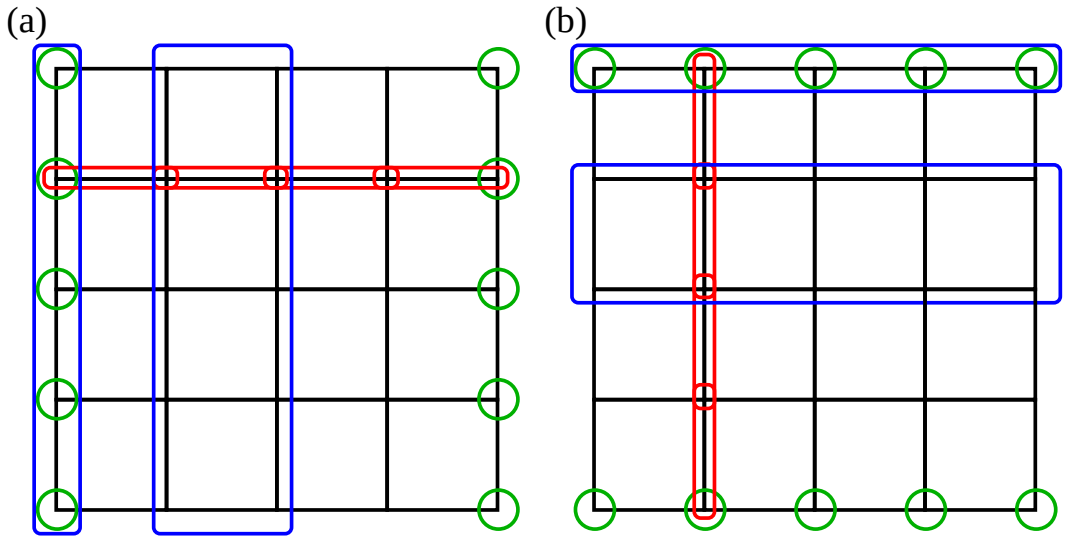

Figure 2.11: Panel (a): Schematic view of the x-part of the effective compass Hamiltonian H'_x (2.59): green circles are $X'_{i,j}$ spin operators acting along first and last column, blue frames symbolize non-local P'_j spin operator products along columns and red frames are NN compass bonds $X'_{i,j}X'_{i,j+1}$. Panel (b): Schematic view of H'_z (2.60): green circles are $Z'_{i,j}$ spin operators acting along first and last line, blue frames symbolize non-local Q'_i spin operator products along lines and red frames are NN compass bonds $Z'_{i,j}Z'_{i+1,j}$.

the size of the Hilbert space is reduced in a dramatic way by a factor 2^{2L-1} [66, 77] which makes it possible to perform easily exact (Lanczos) diagonalization of 2D $L \times L$ clusters up to $L = 6$.

Equivalent subspaces

The spin transformations defined by Eqs. (2.56) and (2.57) bring the QCM Hamiltonian (2.55) into the block-diagonal form of Eqs. (2.59, 2.60) with invariant subspaces labeled by the pairs of vectors $(\vec{r}, \vec{s})$ with $\vec{r} = (r_1, r_2, \ldots, r_{L-1})$ and $\vec{s} = (s_1, s_2, \ldots, s_{L-1})$. The original QCM of Eq. (2.55) is invariant under the transformation $X \leftrightarrow Z$, if one also transforms the interactions, $\alpha \leftrightarrow (1 - \alpha)$. This sets a relation between different invariant subspaces $(\vec{r}, \vec{s})$, i.e. after transforming $\alpha \leftrightarrow (1 - \alpha)$ the QCM Hamiltonian in subspaces $(\vec{r}, \vec{s})$ and $(\vec{s}, \vec{r})$ has the same energy spectrum. In general, we say that the two subspaces are equivalent if the QCM has in them the same energy spectrum. This relation becomes especially simple for $\alpha = \frac{1}{2}$ when for all r_i's and s_i's subspaces $(\vec{r}, \vec{s})$ and $(\vec{s}, \vec{r})$ are equivalent.

Now we will explore another important symmetry of the 2D compass model reducing the

number of nonequivalent subspaces — the translational symmetry. We note from Eq. (2.59) and (2.60) that the reduced Hamiltonians are not translationally invariant for any choice of $(\vec{r},\vec{s})$ even though the original Hamiltonian is. This means that translational symmetry must impose some equivalence conditions among subspace labels $(\vec{r},\vec{s})$. To derive them, let's focus on translation along the rows of the lattice by one lattice constant. Such translation does not affect the P_i symmetry operators, because they consist of spin operators multiplied along the rows, but changes Q_j into Q_{j+1} for all $j < L$ and $Q_L \to Q_1$. This implies that two subspaces $(\vec{r},q_1,q_2,\ldots,q_L)$ and $(\vec{r},q_L,q_1,q_2,\ldots,q_{L-1})$ are equivalent for all values of $\vec{r}$ and $\vec{q}$. Now this result must be translated into the language of $(\vec{r},\vec{s})$ labels, with $s_j = q_j q_{j+1}$ for all $j < L$. This is two-to-one mapping because for any $\vec{s}$ one has two $\vec{q}$'s such that $\vec{q}_+ = (1, s_1, s_1 s_2, \ldots, s_1 s_2 \ldots s_{L-1})$ and $\vec{q}_- = -\vec{q}_+$ differ by global inversion. This sets additional equivalence condition for subspace labels $(\vec{r},\vec{s})$: two subspaces $(\vec{r},\vec{u})$ and $(\vec{r},\vec{v})$ are equivalent if two strings $(1, u_1, u_1u_2, \ldots, u_1u_2\ldots u_{L-1})$ and $(1, v_1, v_1v_2, \ldots, v_1v_2\ldots v_{L-1})$ are related by translations or by a global inversion. For convenience let us call this property of the two vectors a TI-relation. Lattice translations along the columns set the same equivalence condition for $\vec{r}$ labels. Thus full equivalence conditions for subspace labels of the QCM are:

- For $\alpha = \frac{1}{2}$ two subspaces $(\vec{r},\vec{s})$ and $(\vec{u},\vec{v})$ are equivalent if $\vec{r}$ is TI-related with $\vec{u}$ and $\vec{s}$ with $\vec{v}$ or if $\vec{r}$ is TI-related with $\vec{v}$ and $\vec{s}$ with $\vec{u}$.

- For $\alpha \neq \frac{1}{2}$ two subspaces $(\vec{r},\vec{s})$ and $(\vec{u},\vec{v})$ are equivalent if $\vec{r}$ is TI-related with $\vec{u}$ and $\vec{s}$ with $\vec{v}$.

We have verified that no other equivalence conditions exist between the subspaces by numerical Lanczos diagonalizations for lattices of sizes up to 6×6, so we can change all *if* statements above into *if and only if* ones.

Multiplets of equivalent subspaces: examples

For the finite square clusters of the sizes 4×4, 5×5 and 6×6 we used the reduced form of the compass Hamiltonian to reduce the dimensionality of the Hilbert space and apply exact diagonalization techniques to get the ground-state and thermodynamic properties of the QCM. For this purpose we needed to create a list of inequivalent subspaces for $L = 4, 5, 6$ to save time and computational effort.

According to the previous discussion let's denote all inequivalent $\vec{r}$ configurations for our

systems. For $L = 4$ these fall into four TI–equivalence classes:

$$\{[-++{+}],\ \ [--{+}{+}],\ \ [-+{-}{+}],\ \ [---{-}]\}$$

the number of different $\vec{q}$ labels that can be constructed out of each class is equal to the power of the class divided by two. For 4×4 system these are $\{4,2,1,1\}$. For $\vec{p}$ labels we have exactly the same set of classes so the subspace structure can be characterized by following diagrams

$$\begin{array}{cccc} 16 & 8 & 4 & 4 \\ 8 & 4 & 2 & 2 \\ 4 & 2 & 1 & 1 \\ 4 & 2 & 1 & 1 \end{array} \qquad\qquad \begin{array}{cccc} 16 & 16 & 8 & 8 \\ & 4 & 4 & 4 \\ & & 1 & 2 \\ & & & 1 \end{array} \tag{2.61}$$

where each number symbolize an equivalence class of subspaces in anisotropic (left) and isotropic (right) cases. The numbers are equal to the power of each class divided by two. As we see, the right diagram can be obtained from the left by leaving diagonal numbers untouched, erasing subdiagonal numbers and doubling the upper part.

For 5×5 we have again four TI–equivalence classes:

$$\{[-++++{+}],[--+++{+}],[-+-++{+}],[----{-}]\}$$

with half–powers $\{5,5,5,1\}$. This yields to the subspace diagrams:

$$\begin{array}{cccc} 25 & 25 & 25 & 5 \\ 25 & 25 & 25 & 5 \\ 25 & 25 & 25 & 5 \\ 5 & 5 & 5 & 1 \end{array} \qquad\qquad \begin{array}{cccc} 25 & 50 & 50 & 10 \\ & 25 & 50 & 10 \\ & & 25 & 10 \\ & & & 1 \end{array} \tag{2.62}$$

Finally, for our largest system the TI–equivalence classes read:

$$\begin{array}{l} \{[-+++{+}{+}],\ \ [--++{+}{+}],\ \ [-+-+{+}{+}], \\ [--++{-}{+}],\ \ [---+{+}{+}],\ \ [-++-{+}{+}], \\ [+-+-{+}{-}],\ \ [-----{-}]\} \end{array}$$

with half–powers $\{6,6,6,6,3,3,1,1\}$, yielding to following anisotropic diagram:

$$\begin{array}{cccccccc}
36 & 36 & 36 & 36 & 18 & 18 & 6 & 6 \\
36 & 36 & 36 & 36 & 18 & 18 & 6 & 6 \\
36 & 36 & 36 & 36 & 18 & 18 & 6 & 6 \\
36 & 36 & 36 & 36 & 18 & 18 & 6 & 6 \\
18 & 18 & 18 & 18 & 9 & 9 & 3 & 3 \\
18 & 18 & 18 & 18 & 9 & 9 & 3 & 3 \\
6 & 6 & 6 & 6 & 3 & 3 & 1 & 1 \\
6 & 6 & 6 & 6 & 3 & 3 & 1 & 1
\end{array}$$

The isotropic diagram can be obtained using the known procedure. These examples show that the number of inequivalent subspaces N stays the same for the systems of sizes $L = 2l$ and $L = 2l+1$ (with $l = 1, 2, 3, \dots$) and is directly related to the number n of TI–equivalence classes of the binary string of the length L. We have:

$$N = \begin{cases} n^2 & for \qquad \alpha \neq \frac{1}{2}, \\ \frac{1}{2}n(n+1) & for \qquad \alpha = \frac{1}{2}. \end{cases} \tag{2.63}$$

The most numerous TI–equivalence class for the $L \times L$ system consists of the binary strings which transform into themselves after L translations, so carrying highest number of possible pseudomomenta. This implies that largest subspace equivalence class contains $2L^2$ subspaces in anisotropic and $4L^2$ subspaces in isotropic case. Knowing that the total number of subspaces is $2 \times 2^{2(L-1)}$ one can estimate that $N > 2^{2(L-1)}/L^2$ for $\alpha \neq \frac{1}{2}$ and $N > 2^{2L-3}/L^2$ for $\alpha = \frac{1}{2}$.

Hidden order

Due to the symmetries of the QCM Eq. (2.55) only $\langle Z_{i,j}Z_{i,j+d}\rangle$ and $\langle X_{i,j}X_{i+d,j}\rangle$ spin correlations are finite ($d \geq 1$). This suggests that the entire spin order concerns *pairs of spins* from one row (column) which could be characterized by four–point correlation functions of the dimer-dimer type. Indeed, examining such quantities for finite QCM clusters via Lanczos diagonalization we observed certain surprising symmetry: for any α two dimer-dimer $\langle XXXX\rangle$ correlators are equal, no matter whether we place them either along one row or one column, as long as the distance between them is the same (see left panel of Fig. 2.12). This property turns out to be a special case of a more general relation between correlation

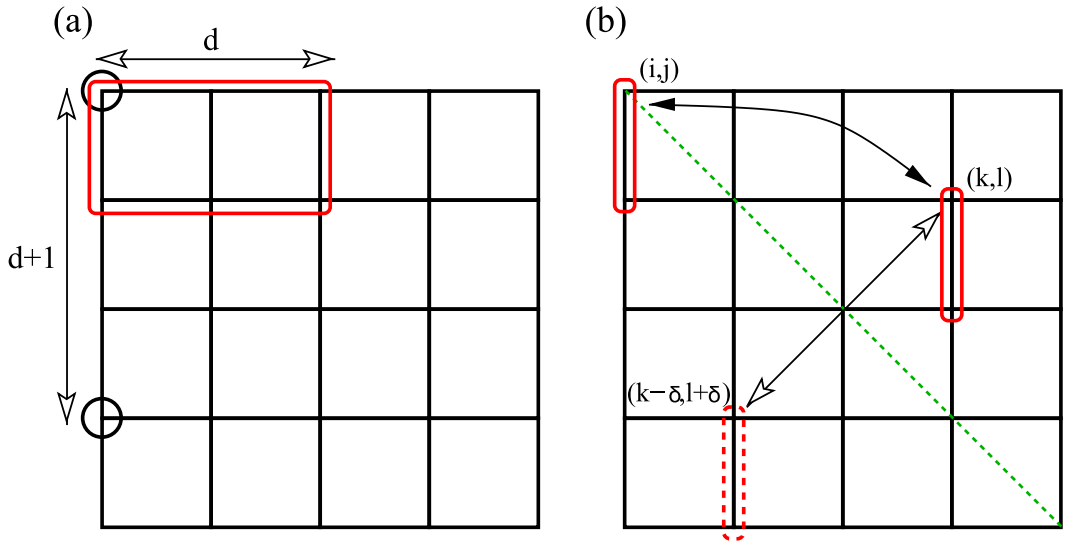

Figure 2.12: Example of application of the proved identities in two cases: panel (a) — Eq. (2.70) long range correlation function $\langle X_{i,j}X_{i+d+1,j}\rangle$ along the column (circles) is equal to the $2d$–point $\langle XX\ldots X\rangle$ correlation function along the row (red frame of length d), panel (b) — Eq. (2.69) for two chosen dimers at (i,j) and (k,l) (solid frames), correlations between them are the same as between dimers at (i,j) and $(k-\delta,l+\delta)$ (dashed frame). Green dashed line marks the plane of the mirror reflection transforming site (k,l) into $(k-\delta,l+\delta)$.

functions of the QCM which we prove below.

We will prove that in the ground state of the QCM for any two sites (i,j) and (k,l) and for any $0<\alpha<1$:

$$\langle X_{i,j}X_{i+1,j}X_{k,l}X_{k+1,l}\rangle \equiv \langle X_{i,j}X_{i+1,j}X_{l-\delta,k+\delta}X_{l-\delta+1,k+\delta}\rangle, \tag{2.64}$$

where $\delta=j-i$. To prove Eq. (2.64) let us transform again the effective Hamiltonian (2.59) in the ground-state subspace ($r_i\equiv s_i\equiv 1$) introducing new spin operators

$$Z'_{i,j}=\tilde{Z}_{i,j}\tilde{Z}_{i,j+1}, \qquad X'_{i,j}=\prod_{r=1}^{j}\tilde{X}_{i,r}, \tag{2.65}$$

with $i,j=1,\ldots,L-1$ and $\tilde{Z}_{i,L}\equiv 1$. This yields

$$\tilde{H}_x=\sum_{i=1}^{L-1}\sum_{j=1}^{L-1}\tilde{X}_{i,j}+\prod_{i=1}^{L-1}\prod_{j=1}^{L-1}\tilde{X}_{i,j}+\sum_{i=1}^{L-1}\prod_{j=1}^{L-1}\tilde{X}_{i,j}+\sum_{i=1}^{L-1}\prod_{j=1}^{L-1}\tilde{X}_{j,i}, \tag{2.66}$$

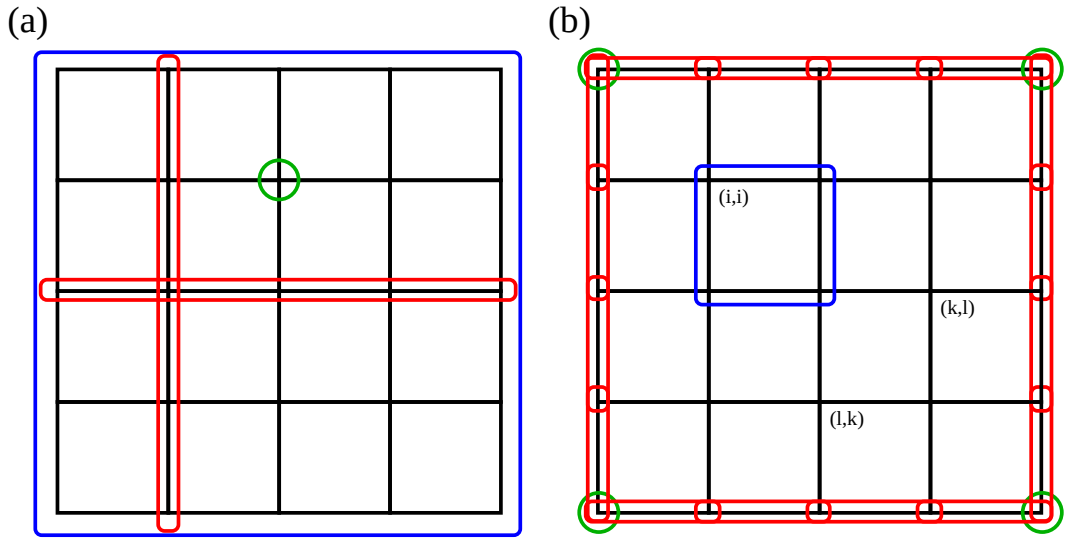

Figure 2.13: Panel (a): Schematic view of the x-part of the reduced ground-state subspace Hamiltonian $\tilde{H}_x$ (2.66): green circles are $\tilde{X}_{i,j}$ spin operators acting on every site, blue frame symbolize non-local product of all $\tilde{X}_{i,j}$ operators products and red frames are products of $\tilde{X}_{i,j}$ along all lines and columns. Panel (b): Schematic view of $\tilde{H}_z$ (2.67): green circles in the corners stand for $\tilde{Z}_{i,j}$ spin operators related to the site (i,j), red frames are $\tilde{Z}\tilde{Z}$ operator products acting on the boundaries of the lattice, and blue square stands for one of the plaquette $\tilde{Z}\tilde{Z}\tilde{Z}\tilde{Z}$ spin operators. The exemplary three sites in the identity (2.69) are: (i,i), (k,l) and (l,k).

and

$$\tilde{H}_z = \sum_a \left\{ \sum_b \tilde{Z}_{a,b} + \sum_{i=1}^{L-2} \left(\tilde{Z}_{a,i}\tilde{Z}_{a,i+1} + \tilde{Z}_{i,a}\tilde{Z}_{i+1,a} \right) \right\} + \sum_{i=1}^{L-2}\sum_{j=1}^{L-2} \tilde{Z}_{i,j}\tilde{Z}_{i,j+1}\tilde{Z}_{i+1,j}\tilde{Z}_{i+1,j+1}, \tag{2.67}$$

where $a = 1, L-1$ and $b = 1, L-1$. Due to the spin transformations (2.56,2.57,2.65), $\tilde{X}_{i,j}$ operators are related to the original bond operators by $X_{i,j}X_{i+1,j} = \tilde{X}_{i,j}$, which implies that

$$\langle X_{i,j}X_{i+1,j}X_{k,l}X_{k+1,l}\rangle = \langle \tilde{X}_{i,j}\tilde{X}_{k,l}\rangle. \tag{2.68}$$

Because of the PBC, all original $X_{i,j}$ spins are equivalent, so we choose $i = j$. The x-part (2.66) of the Hamiltonian is completely isotropic. Note that the z-part (2.67) would also be isotropic without the boundary terms (see Fig. 2.13); the effective Hamiltonian in the ground subspace has the symmetry of a square. Knowing that in the ground state we have

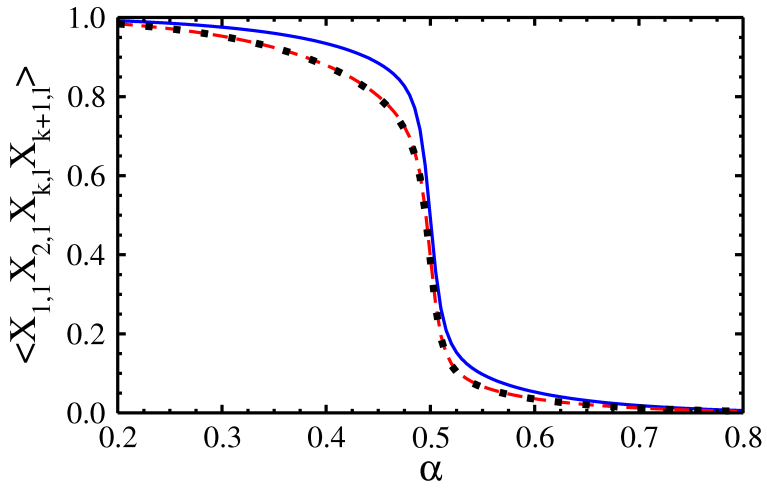

Figure 2.14: Dimer-dimer correlations$\langle X_{1,1}X_{2,1}X_{k,l}X_{k+1,l}\rangle$ for $L = 6$ and $0.2 < \alpha < 0.8$: $(k,l) = (1,2)$, $(1,3)$ and $(1,4)$ are shown by solid, dashed and dotted line.

only Z_2 degeneracy, one finds

$$\langle \tilde{X}_{i,i}\tilde{X}_{k,l}\rangle \equiv \langle \tilde{X}_{i,i}\tilde{X}_{l,k}\rangle, \tag{2.69}$$

for any i and (k,l). This proves the identity (2.64) for $\delta = 0$; $\delta \neq 0$ case follows from lattice translations along rows.

The nontrivial consequences of Eq. (2.69) are: (i) *hidden dimer order* in the ground state of the QCM — dimer correlation functions in two *a priori* nonequivalent directions in the QCM are robust for X-components for $\alpha < \frac{1}{2}$ (Fig. 2.14) and for Z-components for $\alpha > \frac{1}{2}$ (not shown), and (ii) long range two-site $\langle X_{i,j}X_{i+d+1,j}\rangle$ correlations along the columns which are equal to the multi-site $\langle XX\ldots X\rangle$ correlations involving two neighboring rows, see right panel of Fig. 2.12. The latter comes from symmetry properties of the transformed Hamiltonian (2.66,2.67) applied to the multi-site correlations:

$$\langle \tilde{X}_{i,i}\tilde{X}_{i,i+1}\ldots\tilde{X}_{i,i+d}\rangle = \langle \tilde{X}_{i,i}\tilde{X}_{i+1,i}\ldots\tilde{X}_{i+d,i}\rangle. \tag{2.70}$$

Non-local mean field approach

The x-part of the Hamiltonian obtained from Eq. (2.59) in case of open boundaries reads:

$$H'_x = \sum_{i=1}^{L-1} \left\{ \sum_{j=1}^{L-2} X'_{i,j} X'_{i,j+1} + X'_{i,1} + r_i X'_{i,L-1} \right\}, \tag{2.71}$$

and similarly for the z-part. In the ground-state subspace ($r_i \equiv 1$) this resembles the original QCM Eq. (2.55) but with linear boundary terms, which should not affect the ground state properties in the thermodynamic limit and can be regarded as symmetry breaking fields, resulting in finite values of $\langle X'_{i,j} \rangle$ and $\langle Z'_{i,j} \rangle$. Omitting the boundary terms in H'_x and H'_z and putting infinite L we recover the 2D QCM written in nonlocal primed spin operators. Now we can construct a MF splitting of the 2D lattice taking $\langle Z' \rangle \equiv \langle Z'_{i,j} \rangle$ as a Weiss field into (ferromagnetic) Ising chains in transverse field representing each row i:

$$\mathcal{H}'_i(\alpha) = -\sum_j \left\{ (1-\alpha) X'_{i,j} X'_{i,j+1} + 2\alpha \langle Z' \rangle Z'_{i,j} \right\}. \tag{2.72}$$

In analogy to the compass ladder [65], a simple chain Hamiltonian can be solved by Jordan-Wigner transformation for each i:

$$Z'_{i,j} = 1 - 2c^\dagger_{i,j} c_{i,j}, \tag{2.73}$$

$$X'_{i,j} = \left(c^\dagger_{i,j} e^{-i\frac{\pi}{4}} + c_{i,j} e^{i\frac{\pi}{4}} \right) \prod_{r<j} (1 - 2c^\dagger_{i,r} c_{i,r}), \tag{2.74}$$

introducing fermion operators $\{c^\dagger_{i,j}\}$. The diagonalization of the free fermion Hamiltonian can be completed by performing first a Fourier transformation (from $\{j\}$ to $\{k\}$) and next a Bogoliubov transformation (for $k > 0$):

$$\gamma^\dagger_k = \alpha^+_k c^\dagger_k + \beta^+_k c_{-k}, \qquad \gamma^\dagger_{-k} = \alpha^-_k c^\dagger_k + \beta^-_k c_{-k}, \tag{2.75}$$

where $\{\alpha^\pm_k, \beta^\pm_k\}$ are eigenmodes of the Bogoliubov-de Gennes equation for the eigenvalues $\pm E_k$ (with $E_k > 0$). The resulting ground state is a vacuum of $\gamma^\dagger_k$ fermion operators: $|\Phi_0\rangle = \prod_{k>0} (\alpha^+_k + \beta^+_k c^\dagger_{-k} c^\dagger_k)|0\rangle$, which can serve to calculate correlations and the order parameter of the QCM in the MF approach. In agreement with numerical results (not shown), the only nonzero long range two-site spin correlation functions are: $\langle X_{i,j} X_{i+d,j} \rangle$ and $\langle Z_{i,j} Z_{i,j+d} \rangle$. For

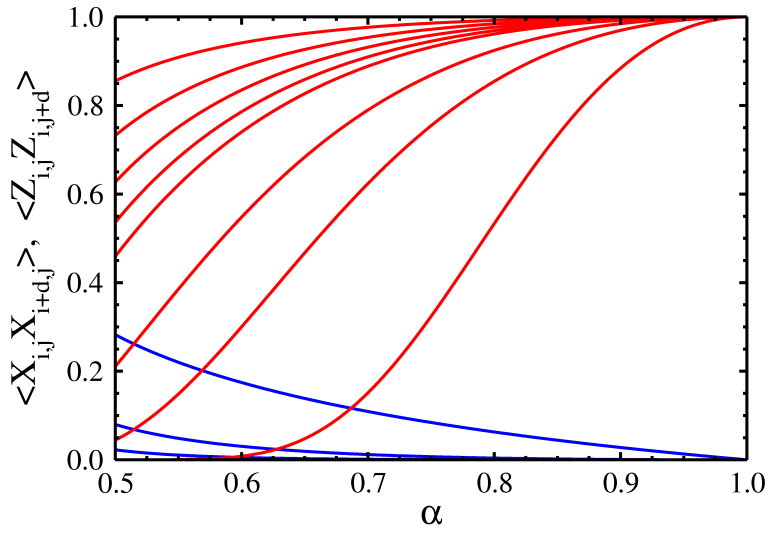

Figure 2.15: Long range spin correlations of the 2D QCM Eq. (2.55) obtained in the MF approach for $\alpha \geq \frac{1}{2}$. Lines starting from 1 at $\alpha = 1$ are the $\langle Z_{i,j}Z_{i,j+d}\rangle$ correlations (2.77) for $d = 1, 2, 3, 4, 5, 10, 20, 80$, while lines starting from 0 at $\alpha = 1$ are the $\langle X_{i,j}X_{i+d,j}\rangle$ correlations (2.76) with $d = 1, 2, 3$; both in descending order.

$d > 1$ they can be represented as follows:

$$\langle X_{i,j}X_{i+d,j}\rangle = \langle X'_{i,j}X'_{i,j+1}\rangle^d, \tag{2.76}$$

$$\langle Z_{i,j}Z_{i,j+d}\rangle = \langle Z'_{i,j}Z'_{i,j+1}\ldots Z'_{i,j+d-1}\rangle^2. \tag{2.77}$$

Having solved the self-consistency equation for $\langle Z'\rangle = (1 - 2\langle n\rangle)$, with

$$\langle n\rangle = \frac{1}{L}\sum_{k>0}\left\{\left(\alpha_k^-\right)^2 + \left(\beta_k^+\right)^2\right\}, \tag{2.78}$$

one can easily obtain $\langle X'_{i,j}X'_{i,j+1}\rangle$ (2.76) for increasing α:

$$\langle X'_{i,j}X'_{i,j+1}\rangle = \frac{2}{L}\sum_{k>0}\left\{\cos k\,\left[\left(\alpha_k^-\right)^2 + \left(\beta_k^+\right)^2\right] + \sin k\,(\alpha_k^-\beta_k^- - \alpha_k^+\beta_k^+)\right\}. \tag{2.79}$$

The nonlocal $\langle Z'_{i,j}Z'\ldots Z'_{i,j+d-1}\rangle$ correlations (2.77) are more difficult to find but they can

be approximated by

$$\langle Z'_{i,j} Z'_{i,j+1} \dots Z'_{i,j+d-1} \rangle = \prod_{k>0} \left\{ \left(\alpha_k^+\right)^2 \left(1 - 2\frac{d}{L}\right)^2 + \left(\beta_k^+\right)^2 \right\}, \tag{2.80}$$

where $L \to \infty$ and $k = (2l-1)\frac{\pi}{L}$ with $l = 1, 2, \dots, \frac{L}{2}$. This approximation is valid as long as $d \ll L$. One finds that the long range $\langle Z_{i,j} Z_{i,j+d} \rangle$ correlations in Z-ordered phase at $\alpha \geq \frac{1}{2}$ show the absence of the Ising-like long range order for $\alpha < 1$ (Fig. 2.15) — they decrease slowly with growing distance d or decreasing α. In contrast, the $\langle X_{i,j} X_{i+d,j} \rangle$ correlations are significant only for nearest neighbors ($d = 1$) and close to $\alpha = \frac{1}{2}$.

The advantage of this nonlocal MF approach for the QCM Eq. (1) over the standard one, which takes $\langle Z \rangle$ as a Weiss field, is that we do not break the $\{P_i, Q_j\}$ and Z_2 symmetries of the model. What more, thanks to numerical and analytical results we know that order parameter of the QCM is given by $\langle H_z \rangle$ [46] — the quantity behaving more like $\langle Z' \rangle$ rather than $\langle Z \rangle$ (having $\langle Z \rangle > 0$ would mean long range magnetic order !). Another interesting feature of the Hamiltonian (2.55) is that it describes all nonlocal compass excitations over the ground state, while the local ones manifest themselves by directions of symmetry breaking fields. These nonlocal column (row) flips are especially interesting from the point of view of topological quantum computing [42] because they guarantee that the system is protected against local perturbations.

2.2.2 Numerical studies of compass model on finite square clusters

There is no exact solution for the 2D compass model but the latest Monte Carlo data [49] prove that the model exhibits a phase transition at finite temperature both in quantum and classical version with symmetry breaking between x and z part of the Hamiltonian. In this section we suggests a scenario for a phase transition with increasing cluster size by the behavior of spin-spin correlation functions and von Neumann entropy of a single column in the ground state obtained via Lanczos algorithm and specific heat calculated using Kernel Polynomial Method (KPM) [78].

The Hamiltonian of the quantum compass model on a square $L \times L$ lattice is given by Eq. (2.55). Ground-state energies and energy gap of the model given by (2.55) has been already calculated for different values of α and for $L \in [2, 5]$ using ED and for higher L using Green's function Monte Carlo method [46]. Our approach will be based on Lanczos algorithm and KPM [78] which will let us calculate the densities of states and the partition functions

for square lattices of the sizes up to $L = 6$. We start by applying Lanczos algorithm to determine spectrum width which is needed for KPM calculations. The resulting few lowest energies that we get from the Lanczos recursion can be compared with the density of states to check if the KPM results are correct. One should be aware that the spectra of odd systems are qualitatively different from those of even ones. For the even systems operator S defined as $S = \prod_{i,j=1}^{L} \frac{1}{2}\{1 - (-1)^{i+j}\}\sigma_{i,j}^{y}$, anticommutes with the Hamiltonian (2.55). This means that for every eigenvector $|v\rangle$ satisfying $\mathcal{H}(\alpha)|v\rangle = E(\alpha)|v\rangle$ we have another eigenvector $|w\rangle = S|v\rangle$ that satisfies $\mathcal{H}(\alpha)|w\rangle = -E(\alpha)|w\rangle$. This proves that even values of L spectrum of $\mathcal{H}(\alpha)$ is symmetric around zero but for odd L's this does not hold; S no longer anticommutes with the Hamiltonian. To obtain a symmetric spectrum in this case we would have to impose open boundary conditions. We would like to emphasize that both Lanczos and KPM calculation for 6×6 lattice (2^{36} - dimensional Hilbert space) would be impossible without using the symmetry operators and reduced Hamiltonians given by Eqs. (2.59) and (2.60) in the subsection (2.2.1).

Ground-state properties and energy levels structure

In Fig. 2.16(a) we compare NN correlations $\langle X_{i,j}X_{i+1,j}\rangle$as functions of α obtained via Lanczos algorithm for clusters of the sizes $L = 3, 4, 5, 6$. Curves for finite clusters converge to certain final functions with infinite slope at $\alpha = 1/2$ but not a step function which would mean completely classical behavior. This result shows that even in large L limit the 2D compass model preserves quantum correction even though it chooses ordering in one direction [49]. Looking at the inset of Fig. 2.16(a) we can see longer–range correlations of the form $C_r(\alpha) \equiv \langle X_{i,j}X_{i+r,j}\rangle$(for the symmetry reasons any other two–point correlation functions involving $X_{i,j}$ operators must be zero in the ground state) for the $L = 6$ system and $r = 1, 2, 3$. Their behavior is very similar to the NN correlations in the sector of $\alpha \leq 1/2$ but for $\alpha > 1/2$ they are strongly suppresed and effectively behave more classically.

In Fig. 2.16(b) we show gound–state covariances of the bond operators $b_{i,j}^{x} \equiv X_{i,j}X_{i+1,j}$ and $b_{i,j}^{z} \equiv Z_{i,j}Z_{i,j+1}$ outgoing from one site and covariances of whole x and $z-$part of the Hamiltonian:

$$H_x = \sum_{i,j=1}^{L} X_{i,j}X_{i+1,j}, \qquad H_z = \sum_{i,j=1}^{L} Z_{i,j}Z_{i,j+1}, \tag{2.81}$$

normalized by total number of terms in H_xH_z i.e., L^4. All covariances are of maximal

magnitude at $\alpha = 1/2$ and get suppressed when system size increases. In case of bond covariances supression is not total and we have some finite covariance in whole range of α with cusp at $\alpha = 1/2$ indicating singular behavior at this point. This means that locally vertical and horizontal bonds cannot be factorized despite the fact that the system chooses only one direction of ordering. On the other hand, the normalized non–local covariance of H_x and H_z tends to vanish for all α in the thermodynamic limit meaning that in the long–range vertical and horizontal bonds behave as independent. We believe that this allows the system to have directionally ordered phase for $L \to \infty$.

Fig. 2.16(c) shows the results of full, brute-force, diagonalization of the 4×4 system (impossible without using symmetries); all negative-energy levels for $0 \leq \alpha \leq 1/2$. Full spectrum for can be constructed from the plot 2.16(c) by the mirror reflections with respect to $\alpha = 1/2$ and $E_n = 0$ axes. The structure of energy levels undergoes the evolution from the ladder-like classical excitation spectrum at $\alpha = 0$ to the discrete-continuum structure at $\alpha = 1/2$. Excited states at $\alpha = 0$, being defected classical AF chains with energy determined by the number of defects, stay rigid until $\alpha \approx 0.2$ in the sense that states with less defects always lie below the states with more defects. Lowest lying states are less susceptible to this mixing, caused by ransverse terms in H_z, and remain separate utnil $\alpha = 1/2$. Even at this point the mixing involves only singly and doubly defected states. From the form of compass Hamiltonian (2.55) one can easily infer the relation between the slope of the energy level E_n and preferred ordering direction in the state $|\Psi_n\rangle$:

$$\frac{1}{J}\frac{d}{d\alpha}E_n(\alpha) = \langle\Psi_n(\alpha)|\, H_x - H_z\, |\Psi_n(\alpha)\rangle\,, \tag{2.82}$$

which means that states ordered by H_x are related with energy levels with positive slope and the others are related with energy levels with negative slope. Zero slope indicates that the state has no preferred ordering direction; this happens to the ground state at $\alpha = 1/2$ and the anticipated symmetry breaking between H_x and H_z implies that in the thermodynamic limit the lowest energy level will have a cusp at this point because any infinitesimal deviation from $\alpha = 1/2$ must lead to strictly positive or negative slope of $E_0\,(\alpha = 1/2 \pm \varepsilon)$.

Another interesting quantity that can be calculated in the ground state is the von Neumann entropy of a chosen subsystem. This entropy tells us to what extent the full wave function of the system cannot be factorized as the wave function of the subsystem times the wave function of the rest. In case of QCM on square lattice the most promising choice of a subsystem would be a single column or a line of the lattice. To calculate von Neumann

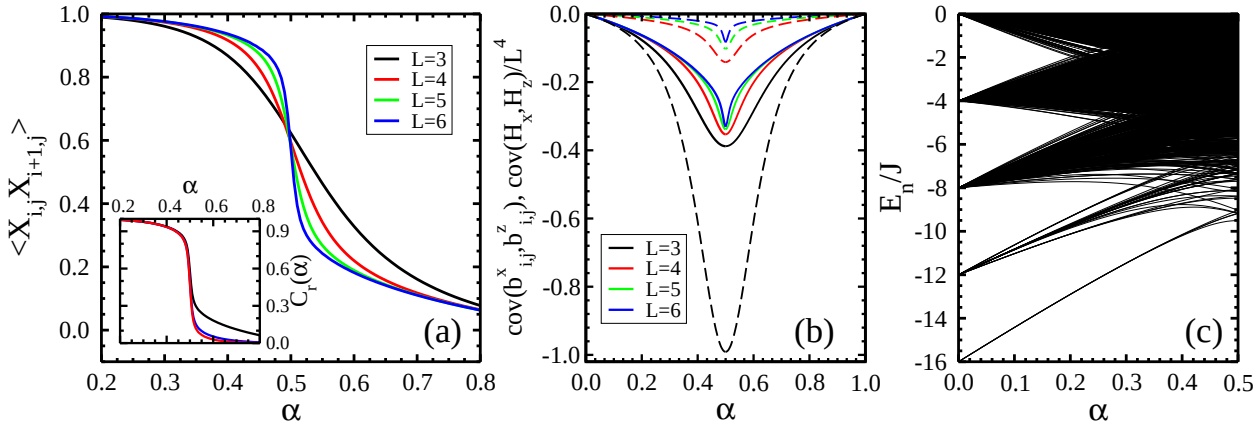

Figure 2.16: Panel (a): spin–spin correlations $\langle X_{i,j}X_{i+1,j}\rangle$ for nearest neighbors with $L = 3, 4, 5, 6$ showed with black, red, green and blue lines respectively and long range correlations (inset) $C_r(\alpha) \equiv \langle X_{i,j}X_{i+r,j}\rangle$ for $L = 6$ with $r = 1, 2, 3$ showed with red, blue and red lines. Panel (b): non–local ground–state covariances of the x and $z-$part of the compass Hamiltonian $\mathrm{cov}(H_x, H_z)/L^4$ (dashed lines) and local ground–state covariances $\mathrm{cov}(b^x_{i,j}, b^z_{i,j})$ of the bond operators $b^x_{i,j} \equiv X_{i,j}X_{i+1,j}$ and $b^z_{i,j} \equiv Z_{i,j}Z_{i,j+1}$ (solid lines) for different cluster sizes L. Panel (c): Full energy spectrum for the $L = 4$ system in the region of $\alpha < 1/2$ and $E_n < 0$.

entropy of a column we need to use its reduced density matrix ρ_L, defined as a partial trace of a full density matrix:

$$\rho = |\Psi_0\rangle \langle\Psi_0|, \tag{2.83}$$

taken over the spins outside the column. This definition, however true, is not very practical. For spin $s = 1/2$ systems one can derive a simpler formula [54]:

$$\rho_L = \frac{1}{2^L} \sum_{\mu_1,..,\mu_L} \langle \sigma_1^{\mu_1} ... \sigma_L^{\mu_L} \rangle \, \sigma_1^{\mu_1} ... \sigma_L^{\mu_L}, \tag{2.84}$$

where $\mu_i = 0, x, y, z$, $\sigma_i^0 = 1$ and $\sigma_i^{\mu_i}$ are the spins taken from one column of a square cluster. After diagonalizing ρ_L, which is of the size $2^L \times 2^L$, one can easily calculate von Neumann entropy as:

$$S_L = -\mathrm{Tr}\rho_L \log_2 \rho_L. \tag{2.85}$$

For the symmetry reasons, described in details in previous section, Eq. (2.84) simplifies greatly as only the x–component spin operators multiplied along the columns can give non-zero ground-state average and their number must be even. Thus, for $L \leq 6$ systems, the

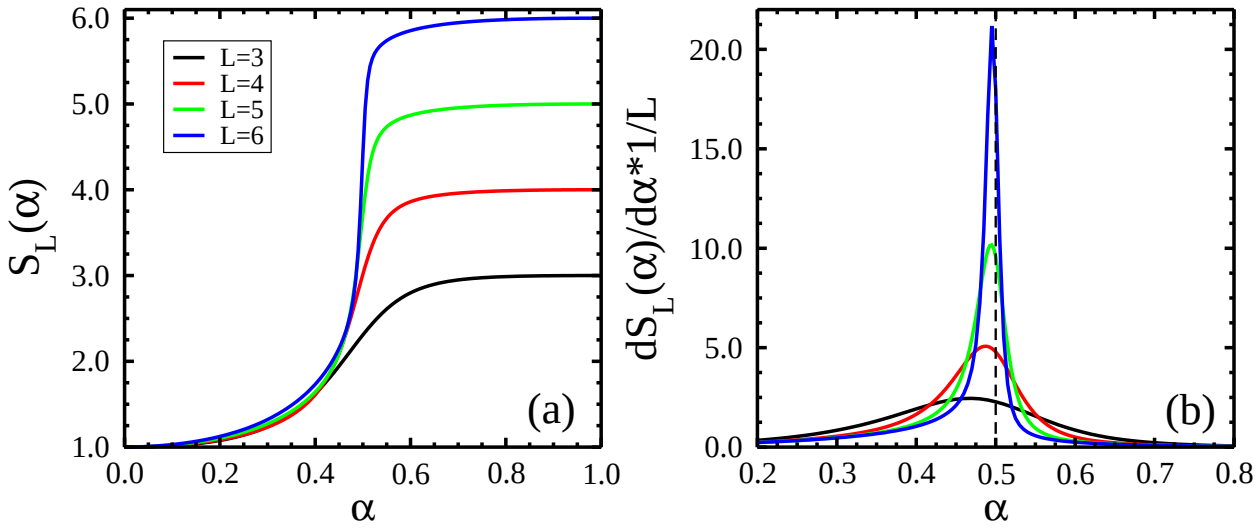

Figure 2.17: Panel (a): von Neumann entropy $S(L, \alpha)$ of a column in the lattice of the size $L = 3, 4, 5, 6$ as a function of α. Panel (b): derivative of $S(L, \alpha)$ with respect to α normalized by L.

ρ_L matrix can be constructed with two–point, four–point and single six–point correlation functions at most. Again, the reduced form of the compass Hamiltonian simplifies getting the ground state but we have to remember that ρ_L is expressed in terms of original spins.

The results of von Neumann entropy calculations for a column of the length L belonging to the cluster of the size $L \times L$ is given in Fig. 2.17(a). We can see that for $\alpha = 0$ the entropy $S_L(\alpha)$ is finite as we expect from the product state. On the other hand, the system at $\alpha = 0$ is purely classical and the Hamiltonian (2.55) describes a set of non–interacting Ising columns. Why is the ground state not a product of columnar states? This result follows from the choice of basis based on the reduced form of the compass Hamiltonian given by Eqs. (2.59) and (2.60). Because of the spin transformations (2.56) and (2.57) the ground state from the subspace $r_i \equiv s_i \equiv 1$ found here is a superposition of two column-product states with equal weights and gives $S_L(0) = 1$. This stays in agreement with the known fact that the von Neumann entropy *depends* on the choice of basis and this dependence comes precisely from the partial trace of the density matrix ρ. For that reason we should always think of the most natural basis for a given problem.

For $0 < \alpha < 1$ the subspace $r_i \equiv s_i \equiv 1$ is the most natural one because it is the only subspace with a ground state (up to global two–fold degeneracy). For $\alpha = 0$ or 1 the choice of the eigenbasis of σ_i^x or σ_i^z operators seems to be much more natural which implies $S_L(0) = S_L(1) = 0$ so the plot in the Fig. 2.17(a) is valid only away from these points.

The upper limit for $S_L(\alpha)$ is always L which can be easily proved by taking a state with all components equal. As we can see in Fig. 2.17(a) this limit is reached for $\alpha \to 1$ and before we have a region of abrupt change in $S_L(\alpha)$ with slope growing with increasing L. This brings us to the Fig. 2.17(b) where we show the behavior of derivative of $S_L(\alpha)$ with respect to α normalized by L. Because of the normalization the area under the plot is constant and equal to 1. As we can see the curve tends to a delta function centered around $\alpha = 1/2$ for a growing system size. This proves that there is a quantum phase transition of the second order at $\alpha = 1/2$ in the thermodynamic limit because second derivative of von Neumann entropy is discontinuous there, which stays in analogy to the classical entropy and classical phase transition.

Specific heat and density of states

The main benefit for us is that after the transformation the Hamiltonian of $L \times L$ compass model ($\alpha = 1/2$) turns into 2^{2L-1} spin models, each one on $(L-1) \times (L-1)$ lattice. In fact, the number of *different* models is much lower than 2^{2L-1}; most of resulting Hamiltonians differ only by a similarity transformation as showed in the previous section (2.2.1). For example, in case of the 5×5 system we find out that only 10 out of 512 Hamiltonians are different; their two lowest energies, obtained using Lanczos algorithm, and degeneracies are given in Table 2.1. In fact, these energies are known with much higher precision (10^{-6}) than that given in Table 2.1, and we also get quite good estimation for the highest energies. This gives us a starting point for KPM calculations.

Kernel Polynomial Method is based on the expansion into the series of Chebyshev polynomials [78]. Chebyshev polynomial of the n-th degree is defined as $T_n(x) = \cos[n \arccos x]$ where $x \in [-1, 1]$ and n is integer. Further on we are going to calculate T_n of the Hamiltonian so first we need to renormalize it so that its spectrum fits the interval $[-1, 1]$. This can be done easily if we know the width of the spectrum. Our aim is to calculate the renormal-

Table 2.1: Ground state energy E_0 and first excited state energy E_1 (in the units of J) and their degeneracies d for 10 nonequivalent subspaces of the 5×5 compass model (2.55) at $\alpha = 1/2$.

n	1	2	3	4	5	6	7	8	9	10
E_0	-14.54	-14.31	-14.30	-14.22	-13.75	-13.67	-13.52	-13.45	-13.22	-12.79
E	-13.80	-13.15	-12.91	-12.50	-12.86	-12.99	-13.26	-12.67	-12.88	-12.30
d	2	20	20	20	50	100	50	100	100	50

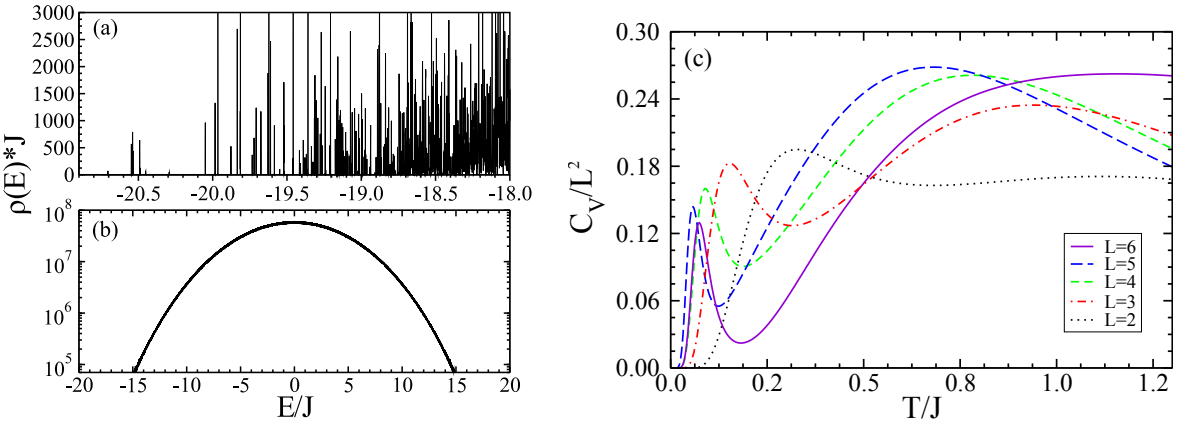

Figure 2.18: Panel (a): density of states for the 6×6 compass cluster at $\alpha = 1/2$ in the low energy region— lowest lying peaks agree with results of Lanczos recursion, excitation spectrum is discrete. Panel (b): full density of states for the same system in the logarithmic scale— parabolic behavior indicates dense gaussian spectrum of high–energy excitation. Panel (c): specific heats C_V/L^2 as functions of temperature T/J for $\alpha = 1/2$ for the compass clusters of the sizes $L = 2, 3, 4, 5, 6$ shown as: black, red, green, blue and violet lines.

ized density of states $\tilde{\rho}(E)$ given by $\tilde{\rho}(E) = (1/D)\sum_{n=0}^{D-1} \delta(E - \tilde{E}_n)$, where the sum is over eigenstates of $\mathcal{H}(\alpha)$ and D is the dimension of the Hilbert space. The moments μ_n of the expansion of $\tilde{\rho}(E)$ in basis of Chebyshev polynomials can be expressed by

$$\mu_n = \int_{-1}^{1} T_n(E)\tilde{\rho}(E)dE = \frac{1}{D}\mathrm{Tr}\{T_n(\tilde{\mathcal{H}})\}\,. \tag{2.86}$$

Trace can be efficiently estimated using stochastic approximation:

$$\mathrm{Tr}\,\{T_n(\tilde{\mathcal{H}})\} \approx \frac{1}{R}\sum_{r=1}^{R} \langle r|T_n(\tilde{\mathcal{H}})|r\rangle\,, \tag{2.87}$$

where $|r\rangle$ $(r = 1, 2, \ldots, R)$ are randomly picked complex vectors with components $\chi_{r,k}$ $(k = 1, 2, \ldots, D)$ satisfying $\langle\chi_{r,k}\rangle = 0$, $\langle\chi_{r,k}\chi_{r',l}\rangle = 0$, $\langle\bar{\chi}_{r,k}\chi_{r',l}\rangle = \delta_{r,r'}\delta_{k,l}$ (average is taken over the probability distribution). This approximation converges very rapidly to the true value of the trace, especially for large D. Action of the $T_n(\tilde{\mathcal{H}})$ operator on a vector $|r\rangle$ can be determined recursively using the following relation between Chebyshev polynomials: $T_n(\tilde{\mathcal{H}})|r\rangle = \{2\tilde{\mathcal{H}}\,T_{n-1}(\tilde{\mathcal{H}}) - T_{n-2}(\tilde{\mathcal{H}})\}|r\rangle$. We can also use the relation $2T_m(x)T_n(x) = T_{m+n}(x) + T_{m-n}(x)$ to get moments μ_{2n} from the polynomials of the degree n. Finally the

required function,

$$\tilde{\rho}(E) \approx \frac{1}{\pi\sqrt{1-E^2}} \left\{ g_0\mu_0 + 2\sum_{n=1}^{N-1} g_n\mu_n T_n(E) \right\}, \tag{2.88}$$

can be reconstructed from the N known moments, where g_n coefficients come from the integral kernel we use for better convergence. Here we use Jackson kernel. Choosing the arguments of $\tilde{\rho}(E)$ as being equal to $E_k = \cos[(2k-1)\pi/2N']$ $(k = 1, 2, \ldots, N')$ we can change the last formula into a cosine Fourier series and use Fast Fourier Transform algorithms to obtain rapidly $\tilde{\rho}(E_k)$. This point is crucial when N and N' are large, which is the case here; our choice will be $N = 20000$ and $N' = 2N$. Using this procedure we can get the density of states for 4×4, 5×5 and 6×6 systems. For $L = 5$ we obtain 10 energy spectra for 10 nonequivalent subspaces — these can be summed up with proper degeneracy factors (see Sec. 2.2.1 and Table 2.1) to get the final density of states $\tilde{\rho}(E)$ and next the partition function via rescaling and numerical integration. For $L = 6$ the number of nonequivalent subspaces is 36 and so is the number of energy spectra.

In Fig. 2.18(a) and 2.18(b) we can see the density of states $\rho(E)$ (without normalization) for $L = 6$ system. Achieved resolution is such that one can distinguish single low–lying energy states and the positions of peaks agree with the results of Lanczos algorithm (see panel (a)). In addition we get information about degeneracy of the energy levels encoded in the area below the peaks. This required very time–consuming calculations as the size of Hilert space was above 30 million. In Fig. 2.18(b) we present an overall view of full density of states in the logarithmic scale exhibiting gaussian behavior. Note different orders of magnitude in Figs. 2.18(a) and 2.18(b). Both plots show that the spectrum of the compass model in the thermodynamic limit can be discrete in the lowest and highest–energy region and continuous in the center which agrees with the existence of ordered phase above $T = 0$ [49].

In the panel (c) of Fig. 2.18 we show the specific heats C_V/L^2 for the compass $L \times L$ clusters calculated from the densities of states $\rho(E)$. The curves exhibit two–peak structure similar to the one observed for a compass ladder (see Fig. 2.10) but in contrary to the ladder case, the low–temperature peak seems to vanish when $L \to \infty$ and specific heat develops a gap before the high–temperature peak. Effectively, the specific heat curve in the thermodynamic limit would be rather the one of classical Ising ladder with a single, broad peak in high temperature and zero specific heat until certain T_0 (see Fig. 2.10 (e)) than the one for a compass ladder with robust low–energy excitations. This means that the thermal behavior

of the 2D QCM is mostly classical and once more agrees with the presence of ordered phase for finite T in the thermodynamic limit.

2.2.3 Summary and conclusions

On the example of the QCM, we argue that for certain class of the pseudospin models, which are not SU(2) symmetric, the properties can be uniquely determined by discrete symmetries like parity. In this case conservation of spin parities in rows and columns, for x and z-components of spins, makes the system in the ground state behave according to a nonlocal Hamiltonian (2.59,2.60). In the ground state most of the two-site spin correlations vanish and the two-dimer correlations exhibit the nontrivial hidden order. For a finite system, the low-energy excitations are the ground states of the QCM Hamiltonians in different invariant subspaces which, as we argue, become degenerate with the ground state in the thermodynamic limit, leading to degeneracy d being exponential in the linear system size L ($d = 2^{2L-1}$). The invariant subspaces can be classified by lattice translations — the reduction of the Hilbert space achieved in this way is important for future numerical studies of the QCM and will play a role for spin models with similar symmetries. Finally, the nonlocal Hamiltonian containing symmetry breaking terms suggests the MF splitting respecting conservation of parity and leading to the known physics of one-dimensional quantum Ising model describing correlation functions and the order parameter of the QCM.

The reduced QCM Hamiltonian turned out to be very useful for the state-of-the-art implementations of the ED techniques and gives the access to the system sizes unavailable otherwise. In contrast to the point-group or translational symmetries often explored for such models, spin transformations lead to spin Hamiltonian again which makes it particularly easy to implement. Although QCM has no sign problem and can be treated with powerful quantum Monte Carlo methods, ED gives most complete solution: the ground-state wave function giving the access to all possible correlators and measures of entanglement. Using Lanczos and full diagonalization techniques we showed the behavior of all two-point correlation functions for different system sizes and full structure of energy levels as functions of anizotropy parameter α, indication discrete-continuum nature of the spectrum of the QCM. By calculating derivative with respect to α of the von Neumann entropy of a single column of a square lattice, being the characteristic, classical subsystem of the model, we proved that there is a second order quantum phase transition in the isotropic point $\alpha = 1/2$ separating two perpendicular, nematically ordered phases. The continuous, rather than first order,

character of the phase transition is confirmed by the behavior of NN spin correlation functions, proportional to the nematic order parameter, which remain continuous up to $L = 6$. This stays in odds with early conclusions about the phase transition in 2D QCM [45]. Using Kernel Polynomial Method we gained the access to the full density of state function $\rho(E)$ for system sizes excluding full diagonalization, i.e., for $L = 5, 6$. The behavior of $\rho(E)$ for $L = 6$ confirms discrete-continuum nature of the spectrum observed for smaller system size and remains in agreement with the existence of ordered phase in finite temperature. Specific heat of the system calculated from the $\rho(E)$ for growing L evolves to the curve characteristic for a classical Ising ladder with a single, broad peak in high and a gap in low temperature. We argue that this behavior exhibits a classical behavior of the QCM at finite temperature and confirms the existence of the ordered phase.

Chapter 3

Kugel–Khomskii model

Recent interest and progress in the theory of SO superexchange models was triggered by the observation that orbital degeneracy drastically increases quantum fluctuations which may suppress long-range order in the regime of strong competition between different types of ordered states near the quantum critical point [27]. The simplest model of this type is the Kugel-Khomskii (KK) model introduced long ago [5] for $KCuF_3$, a strongly correlated system with a single hole within degenerate e_g orbitals at each Cu^{2+} ion. Kugel and Khomskii showed that many-body effects could then give rise to orbital order stabilized by a purely electronic superexchange mechanism. A similar situation occurs in a number of compounds with active orbital degrees of freedom, where strong on-site Coulomb interactions localize electrons (or holes) and give rise to SO superexchange [4, 25, 26]. The orbital superexchange may stabilize the orbital order by itself, but in e_g systems it is usually helped by the orbital interactions which follow from the Jahn-Teller distortions of the lattice [5, 79–81]. For instance, in $LaMnO_3$ these contributions are of equal importance and both of them are necessary to explain the observed high temperature of the structural transition [80]. Also in $KCuF_3$ the lattice distortions play an important role and explain its strongly anisotropic magnetic and optical properties [81–84]. The latest theoretical and experimental results for this compound show that another types of interactions, like direct orbital exchange driven by a combination of electron–electron interactions and ligand distortions [85] or dynamical Dzyaloshinsky-Moriya interaction [86], are necessary to explain structural phase transition in $KCuF_3$ at $T_{JT} \simeq 800K$ and peculiarities in spin dynamics [87]. The compound is believed to the best realization of 1D Heisenberg model above the Nèel temperature $T_N = 39K$ [85, 88] characterized by spinon excitations [89].

While the coexisting A-type AF (A-AF) order and the orbital order is well established in $KCuF_3$ below T_N [90] and this phase is reproduced by the SO d^9 superexchange model [91], the model poses an interesting question by itself. Which types of coexisting spin and orbital order (or disorder) are possible when its microscopic parameters are varied? So far, it was only established that the long-range AF order is destroyed by strong quantum fluctuations [28, 91] and it has been shown that instead certain spin disordered phases with valence-bond (VB) correlations stabilized by local orbital correlations are favored [25, 27]. However, the phase diagram of the Kugel-Khomskii d^9 model is unknown — it was not studied systematically beyond the MF approximation and certain simple variational wave functions and it remains an outstanding problem in the theory [27].

To establish reliable results concerning short-range order in the crossover regime between phases with long-range AF or FM order, we developed a *cluster MF approach* which goes beyond the single site mean field in the SO system [92] and is based on an exact diagonalization of a cluster coupled to its neighbors by MF terms. The cluster is chosen to be sufficient for investigating both AF phases with four sublattices and VB states, with spin singlets either along the c axis or within the ab planes. This theoretical method is motivated by possible SO entanglement [32] which is particularly pronounced in the 1D SU(4) [or SU(2)$\otimes$SU(2)] SO models [93] and occurs also in the models for perovskites with AF spin correlations on the bonds, where in some cases the Goodenough-Kanamori rules are violated [3]. In the perovskite vanadates such entangled states play an important role in their optical properties [94], in the phase diagram [95] and in the dimerization of FM interactions along the c axis in the C-AF phase of YVO_3 [96, 97]. Below we shall investigate whether entangled states could play a role in the present Kugel-Khomskii model for a bilayer, 2D and 3D lattices with nearly degenerate e_g orbitals. Thereby we establish exotic type of SO mean field to capture joint quantum SO fluctuations, and investigate signatures of entangled states in this phase.

3.1 Derivation of the Kugel–Khomskii model

For realistic parameters the late transition metal oxides or fluorides are strongly correlated and electrons localize in the $3d$ orbitals [98, 99], leading to Cu^{2+} ions with spin $S = 1/2$ in d^9 configuration. The examples of such systems are: $KCuF_3$ with 3D cubic lattice, $K_3Cu_2F_7$ representing bilayer compounds and K_2CuF_4 and also $La_2CuO_4$with 2D square lattice. The virtual charge excitations lead then to superexchange which involves also orbital degrees of freedom in systems with partly filled degenerate orbitals. We consider here a model with two

active and nearly degenerate e_g orbitals,

$$|x\rangle \equiv (x^2 - y^2)/\sqrt{2}, \qquad |z\rangle \equiv (3z^2 - r^2)/\sqrt{6}\,, \tag{3.1}$$

while t_{2g} orbitals do not contribute and are filled with electrons. They do not couple to e_g's by hopping through fluorine and hence can be neglected. In what follows we investigate an electronic model and neglect coupling to the lattice distortions arising due to Jahn-Teller effect.

The Hamiltonian for d^9 systems contains: holes' kinetic energy H_t with hopping amplitude t, electron-electron interactions $H_{\rm int}$, with on-site Hubbard U and Hund's exchange coupling J_H, as well as crystal-field splitting term H_z playing a role of external orbital field E_z acting on e_g orbitals:

$$H_{e_g} = H_t + H_{\rm int} + H_z. \tag{3.2}$$

Because of the shape of the two e_g orbitals Eq. (3.1), the effective hopping elements are direction dependent and change depending on the direction of the bond $\langle ij\rangle$. The only non-vanishing $(dd\sigma)$ hopping element in the c direction connects two $|z\rangle$ orbitals [79], while the elements in the ab planes satisfy Slater-Koster relations. Taking the effective $(dd\sigma)$ hopping element t for two z orbitals on a bond along the c axis as a unit, H_t is given by

$$\begin{aligned} H_t &= \frac{t}{4}\sum_{\langle ij\rangle\|ab}\Big\{3d^\dagger_{ix\sigma}d_{jx\sigma} + d^\dagger_{ix\sigma}d_{jz\sigma} \pm \sqrt{3}(d^\dagger_{iz\sigma}d_{jx\sigma} + d^\dagger_{ix\sigma}d_{jz\sigma}) + \text{H.c.}\Big\} \\ &+ t\sum_{\langle ij\rangle\|c}(d^\dagger_{iz\sigma}d_{jz\sigma} + \text{H.c.}), \end{aligned} \tag{3.3}$$

where $d^\dagger_{ix\sigma}$ and $d^\dagger_{iz\sigma}$ are creation operators for a hole in x and z orbital with spin $\sigma =\uparrow,\downarrow$, and the in-plane x–z hopping depends on the phase of $|x\rangle$ orbital involved in the hopping process along the bond $\langle ij\rangle$ and is included in the alternating sign of the terms $\propto\sqrt{3}$ between a and b cubic axes. The bonds along c direction are absent in case of a 2D system. The on-site electron-electron interactions are described by [100]:

$$\begin{aligned} H_{\rm int} &= U\sum_{i\alpha} n_{i\alpha\uparrow}n_{i\alpha\downarrow} + (U-3J_H)\sum_{i\sigma} n_{ix\sigma}n_{iz\sigma} + (U-2J_H)\sum_{i\sigma} n_{ix\sigma}n_{iz\bar\sigma} \\ &- J_H\sum_{i\sigma} d^\dagger_{ix\sigma}d_{ix\bar\sigma}d^\dagger_{iz\bar\sigma}d_{iz\sigma} + J_H\sum_i (d^\dagger_{ix\uparrow}d^\dagger_{ix\downarrow}d_{iz\downarrow}d_{iz\uparrow} + H.c.). \end{aligned} \tag{3.4}$$

Here $n_{i\alpha\sigma}$ stands for the hole density operator in orbital $\alpha = x, z$ with spin σ, and $\bar{\sigma} = -\sigma$. This Hamiltonian is rotationally invariant in the orbital space and describes the multiplet structure of d^{n+1}or d^{n-1} ions in charge excitations $d_i^n d_j^n \rightleftarrows d_i^{n-1} d_j^{n+1}$. Here we use it for d^8 ions excited in a Mott insulator with d^9 ionic configuration ($n = 9$). We assumed the wave function to be real which gives the same amplitude J_H for Hund's exchange interaction and for pair hopping term between $|x\rangle$ and $|z\rangle$ orbitals.

The last term of the H_{e_g} Hamiltonian lifts the degeneracy of the two e_g orbitals

$$H_z = -\frac{1}{2} E_z \sum_{i\sigma} (n_{ix\sigma} - n_{iz\sigma}), \tag{3.5}$$

and favors hole occupancy of x (z) orbitals when $E_z > 0$ ($E_z < 0$). It can be associated with a uniaxial pressure along the c axis or a crystal field splitting induced by a static Jahn-Teller effect.

The typical energies for the Coulomb U and Hund's exchange J_H elements can be deduced from the atomic spectra or found using density functional theory with constrained electron densities. Earlier studies performed within the local density approximation (LDA) gave rather large values of the interaction parameters [99]: $U = 8.96$ eV and $J_H = 1.19$ eV. More recent studies used the LDA with on-site Coulomb interaction treated within the LDA+U scheme and gave somewhat reduced values [101]: $U = 7.5$ eV and $J_H = 0.9$ eV. However, both parameter sets give rather similar values of Hund's exchange parameter,

$$\eta = \frac{J_H}{U}, \tag{3.6}$$

being close to 0.13 or 0.12, i.e., within the expected range $0.1 < \eta < 0.2$ for strongly correlated late transition metal oxides. Note that the physically acceptable range which follows from Eq. (3.4) is much broader, i.e., $0 < \eta < 1/3$. The upper limit follows from the condition $(U - 3J_H) > 0$ for the energy of the high-spin excitations.

The value of effective intersite ($dd\sigma$) hopping element t is more difficult to estimate. It follows from the usual effective process via the oxygen orbitals described by a t_{pd} hopping, and the energy difference between the $3d$ and $2p$ orbitals involved in the hopping process, so-called charge-transfer energy [79]. A representative value of $t \simeq 0.65$ eV may be derived from the realistic parameters [99] of CuO_2 planes in La_2CuO_4. Taking in addition $U = 7.5$ eV, one finds the superexchange constant between hole $S = 1/2$ spins within $|x\rangle$ orbitals in a single CuO_2 plane, $J_x = (9/4)t^2/U \simeq 0.127$ eV, which reproduces well the experimental

value in La_2CuO_4, as discussed in Ref. [91].

Thanks to $t \ll U$ we can safely assume that the ground state is insulating at the filling of one hole localized at each Cu^{2+} ion. In the atomic limit ($t = 0$ and $E_z = 0$) we have large 4^N-fold degeneracy as the hole can occupy either x or z orbital and have up or down spin. This high degeneracy is lifted due to effective superexchange interactions between spins and orbitals at NN Cu ions i and j which act along the bond $\langle ij \rangle$. They originate from the virtual transitions to the excited states, i.e., $d_i^9 d_j^9 \rightleftharpoons d_i^{10} d_j^8$, and are generated by the hopping term Eq. (3.3). Hence, the effective SO model can be derived from the atomic limit Hamiltonian containing interaction Eq. (3.4) and the crystal-field term Eq. (3.5), treating the kinetic term Eq. (3.3) as a perturbation. Taking into account the full multiplet structure of the excited states for the d^8 configuration [91], one gets the corrections of the order of J_H to the Hamiltonian which results for the degenerate excited states (at $J_H = 0$). Calculating the energies of the excited d^8 states we neglected their dependence on the crystal-field splitting E_z. This assumption is well justified as the deviation from the equidistant spectrum at $E_z = 0$ become significant only for $|E_z|/J_H > 1$ and in case of La_2CuO_4 one finds $|E_z|/J_H \approx 0.27$. For systems close to orbital degeneracy, which we are interested in, this ratio is even smaller.

The derivation which follows Ref. [91] leads to the SO model, with the Heisenberg Hamiltonian for the spins coupled to the orbital problem, as follows:

$$\begin{aligned} \mathcal{H} &= -\frac{1}{2} J \sum_{\langle ij \rangle || \gamma} \left\{ (r_1 \, \Pi_t^{(ij)} + r_2 \, \Pi_s^{(ij)}) \left(\frac{1}{4} - \tau_i^\gamma \tau_j^\gamma \right) + (r_2 + r_4) \, \Pi_s^{(ij)} \left(\frac{1}{2} - \tau_i^\gamma \right) \left(\frac{1}{2} - \tau_j^\gamma \right) \right\} \\ &- E_z \sum_i \tau_i^c . \end{aligned} \tag{3.7}$$

Here $\gamma = a, b, c$ labels the direction of a bond $\langle ij \rangle$ in the bilayer or 3D system, while $\gamma = a, b$ for a monolayer (2D lattice). The energy scale is given by the superexchange constant, $J = \frac{4t^2}{U}$, and the orbital operators at site i are given by $\vec{\tau}_i = \{\tau_i^a, \tau_i^b, \tau_i^c\}$. The terms proportional to the coefficients $\{r_1, r_2, r_4\}$ refer to the charge excitations to the upper Hubbard band [91] which occur in the $d_i^9 d_j^9 \rightleftharpoons d_i^9 d_j^{10}$ processes and depend on Hund's exchange parameter η Eq. (3.6) via the coefficients:

$$r_1 = \frac{1}{1 - 3\eta}, \qquad r_2 = \frac{1}{1 - \eta}, \qquad r_4 = \frac{1}{1 + \eta}. \tag{3.8}$$

The model Eq. (3.7) depends thus on two parameters: (i) Hund's exchange coupling η Eq. (3.6), and (ii) the crystal-field splitting E_z/J, see Eq. (3.5). The operators Π_{ij}^s and Π_{ij}^t

stand for projections of spin states on the bond $\langle ij \rangle$ on a singlet (Π_{ij}^{s}) and triplet (Π_{ij}^{t}) configuration, respectively,

$$\Pi_{s}^{(ij)} = \left(\frac{1}{4} - \mathbf{S}_i \cdot \mathbf{S}_j \right), \quad \Pi_{t}^{(ij)} = \left(\frac{3}{4} + \mathbf{S}_i \cdot \mathbf{S}_j \right), \tag{3.9}$$

for spins $S = 1/2$ at both sites i and j, and τ_i^{γ} (with $\gamma = a, b, c$ standing for a direction in the real space) represent e_g orbital degrees of freedom and can be expressed in terms of Pauli matrices $\{\sigma_i^x, \sigma_i^y, \sigma_i^z\}$ in the following way:

$$\tau_i^{a,b} \equiv \frac{1}{4}(-\sigma_i^z \pm \sqrt{3}\sigma_i^x), \quad \tau_i^c \equiv \frac{1}{2}\sigma_i^z. \tag{3.10}$$

The matrices $\{\sigma_i^{\gamma}\}$ act in the orbital space (and have nothing to do with the physical spin $\mathbf{S}_i$ present in this problem). Note that $\{\tau_i^{\gamma}\}$ operators are not independent because they satisfy the local constraint, $\sum_{\gamma} \tau_i^{\gamma} \equiv 0$.

In Fig. 3.1 (a)-(d) we present typical orbitals configurations with ferro-orbital (FO) order and alternating orbital (AO) order considered in the e_g orbital models [11, 27]. In the next sections we shall analyze their possible coexistence with spin order in the bilayer d^9 SO model Eq. (3.7). As we can see, the maximal (minimal) value of the orbital operators τ_i^{γ} is related with orbital taking shape of a clover (cigar) with symmetry axis pointing along the direction γ.

3.2 Bilayer Kugel–Khomskii model

In analogy to the models introduced for bilayer manganite $La_{2-x}Sr_xMn_2O_7$ [102, 103], we consider here a model for $K_3Cu_2F_7$ bilayer compound. The bilayer $K_3Cu_2F_7$ system is known since twenty years [104], but its magnetic properties were reported only recently [105]. We shall address the orbital order and magnetic correlations realized in this system below. The purpose of this section is to analyze a spin-orbital KK model for a bilayer, consisting of two *ab* layers connected by interlayer bonds along the *c* axis. This choice is motivated by an expected competition of the long-range AF order with VB-like states. One of them, a VB phase with spin singlets on the interlayer bonds (VBz phase), is stabilized by large crystal field E_z which favors occupied $3z^2 - r^2$ orbitals (by holes). We shall investigate the range of stability of this and other phases, including the A-AF phase similar to the one found in $KCuF_3$.

The section is organized as follows. In Sec. 3.2.1 we present phase diagram of the bilayer KK model obtained in a single-site MF approximation. Next we argue that quantum fluctuations and intrinsic frustration of the superexchange near the orbital degeneracy motivate the solution of this model in a better MF approximation based on an embedded cubic cluster, which we introduce in Sec. 3.2.2. It leads to MF equations which were solved self-consistently in an iterative way, as described in Sec. 3.2.3. In the next subsections we present two phase diagrams obtained from the MF analysis using Bethe-Peierls-Weiss cluster method: (i) the phase diagram which follows from factorization of spin and orbital degrees of freedom in Sec. 3.2.4, and (ii) the one obtained when also on-site joint SO order parameter is introduced, see Sec. 3.2.5. The latter approach gives nine different phases, and we describe characteristic features of their order parameters in Sec. 3.2.6. We introduce bond correlation functions in Sec. 3.2.7, and concentrate their analysis on the regime of almost degenerate e_g orbitals, focusing on the proximity of the plaquette VB (PVB) and entangled SO (ESO) phases. Finally, we quantify the SO entanglement using on-site and bond correlations, see Sec. 3.2.8, which modifies significantly the phase diagram of the model with respect to the one obtained when spin and orbital operators are disentangled. General discussion and summary are presented in Sec. 3.2.9.

3.2.1 Single–site mean–field approach

The bilayer SO d^9 model Eq. (3.7) poses a difficult many-body problem which cannot be solved exactly. The only simple limits are either $|E_z| \to \infty$ or $\eta \to (1/3)^-$ which we discuss below. In the first case the dominant term is the crystal field $\propto E_z$ and, depending on its sign, we get uniform orbital configuration $\tau_i^c \equiv \pm 1/2$ and $\tau_i^{a,b} \equiv \mp 1/4$. After inserting these classical expectation values into the Hamiltonian Eq. (3.7) we are left with the spin part which has purely Heisenberg form.

We will show below that in the bilayer geometry of the lattice the single-site MF approximation predicts long-range ordered G-AF phases at $\eta = 0$ known from the 3D SO d^9 model [27], see Fig. 3.1(d). For negative $E_z \to -\infty$ and FO order of z orbitals shown in Fig. 3.1(c), we get an AF coupling in the c direction and a weaker AF coupling in the ab planar directions (in the regime of small η). For positive $E_z \to \infty$ one finds instead the FO order of x orbitals shown in Fig. 3.1(d), and two ab planes decouple, so we are left with the AF Heisenberg model on two independent 2D square lattices. In this case and the spins exhibit either G-AF, see Fig. 3.1(d) or C-AF order (not shown). Ferromagnetism is obtained in the

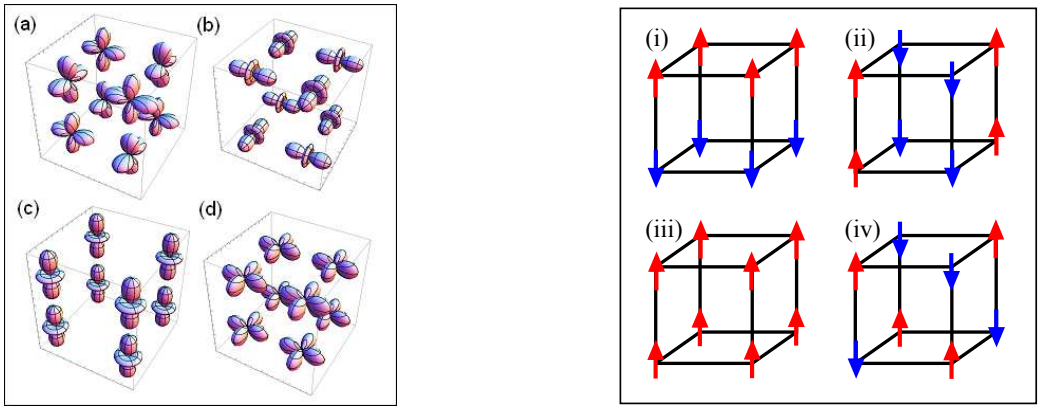

Figure 3.1: Left panel: schematic view of four representative orbital configurations of a bilayer lattice shown on a cubic cluster: (a) AO order with $\langle \tau_i^{a(b)} \rangle = 1/2$ changing from site to site and $\langle \tau_i^c \rangle = -1/4$, obtained for $E_z < 0$, (b) AO order with $\langle \tau_i^{a(b)} \rangle = -1/2$ changing from site to site and $\langle \tau_i^c \rangle = -1/4$, obtained for $E_z > 0$, (c) FO order with occupied z orbitals and $\langle \tau_i^c \rangle = -1/2$ (cigar-shaped orbitals), and (d) FO order with occupied x orbitals and $\langle \tau_i^c \rangle = 1/2$ (clover-shaped orbitals). Right panel: schematic view of four representative spin configurations of a bilayer lattice showed on a cubic cluster: (i) A-AF configuration, (ii) C-AF configuration, (iii) FM configuration and (iv) G-AF configuration. Arrows stand for up or down spins.

present model for any E_z if η is sufficiently large, i.e., when the superexchange is dominated by terms proportional to r_1 which favor formation of spin triplets on the bonds accompanied by AO order depicted in Figs. 3.1(a) and 3.1(b).

In what follows we will show the simplest, single-site MF approximation of the Hamiltonian Eq. (3.7) and the resulting phase diagram. After averaging over spins, the Hamiltonian, originally expressed in terms of bond operators, can be then written in a form of the orbital problem given below:

$$\mathcal{H}_{\rm MF} = \frac{1}{2} J \sum_{i,\gamma} \left\{ \tau_i^\gamma \tau_{i+\gamma}^\gamma (\chi^\gamma - \xi^\gamma) + \tau_i^\gamma \xi^\gamma - \frac{1}{4}(\chi^\gamma + \xi^\gamma) \right\} - E_z \sum_i \tau_i^c, \qquad (3.11)$$

with sum running over all sites and cubic axes $\gamma = a, b, c$. Here we adopted a shorthand notation in $\tau_{i+\gamma}^\gamma$with $i + \gamma$ meaning the nearest neighbor of site i in the direction γ.

The quantities

$$\chi^\gamma = \left\{ \begin{array}{ccc} r_1 \Pi_t^\gamma + r_2 \Pi_s^\gamma & if & \gamma = a, b \\ \frac{1}{2}(r_1 \Pi_t^\gamma + r_2 \Pi_s^\gamma) & if & \gamma = c \end{array} \right\}, \quad \xi^\gamma = \left\{ \begin{array}{ccc} (r_2 + r_4) \Pi_s^\gamma & if & \gamma = a, b \\ \frac{1}{2}(r_2 + r_4) \Pi_s^\gamma & if & \gamma = c \end{array} \right\} \qquad (3.12)$$

are the parameters obtained by averaging over spin operators. The coefficients 1/2 in the χ^γ and ξ^γ terms along the c axis follow from the bilayer geometry of the lattice. We assumed that the spin order, determining χ^γ and ξ^γ, depends only on the direction γ and not on site i. This is sufficient to investigate the phases with either AF or FM long-range order. More precisely, these are spin-singlet and spin-triplet projectors $\Pi^\gamma_{s(t)} \equiv \Pi^{s(t)}_{i,i+\gamma}$ Eqs. (3.9) that are independent of i. As far as only a single site is concerned the spins cannot fluctuate at zero temperature and the projectors can be replaced by their average values:

$$\Pi^\gamma_s = \frac{1}{4} - \langle \mathbf{S}_i \cdot \mathbf{S}_{i+\gamma} \rangle, \quad \Pi^\gamma_t = \frac{3}{4} + \langle \mathbf{S}_i \cdot \mathbf{S}_{i+\gamma} \rangle. \tag{3.13}$$

The values of the projectors depend on the assumed spin order. Here we consider four different spin configurations: (i) G-AF - antiferromagnet in all three directions shown in Fig. 3.1(d), (ii) C-AF - antiferromagnet in the ab planes with FM correlations in the c direction (not shown), (iii) A-AF - AF phase with FM order in the ab planes and AF correlations in the c direction depicted in Fig. 3.1(a), (iv) FM phase (not shown). The numerical values of the spin projection operators in these phases are listed in Table 3.1.

After fixing spins, the MF approximation involves the well-know decoupling for the orbital operators:

$$\tau^\gamma_i \tau^\gamma_{i+\gamma} \simeq \langle \tau^\gamma_i \rangle \tau^\gamma_{i+\gamma} + \tau^\gamma_i \langle \tau^\gamma_{i+\gamma} \rangle - \langle \tau^\gamma_i \rangle \langle \tau^\gamma_{i+\gamma} \rangle. \tag{3.14}$$

The last step is to define sublattices for the orbitals. The most reasonable choice would be to assume AO order meaning that neighboring orbitals are always rotated by $\pi/2$ in the ab plane with respect to each other. To implement this structure into the MF Hamiltonian we define new direction $\bar{\gamma}$ as follows: $\bar{\gamma} = b, a$ for $\gamma = a, b$ and $\bar{\gamma} = c$ for $\gamma = c$. Using $\bar{\gamma}$ we can

Table 3.1: Mean values of triplet Π^γ_t and singlet Π^γ_s projection operators Eqs. (3.13) for a bond $\langle ij \rangle$ along the axis γ in different phases with long-range magnetic order which occur in the MF phase diagram, see Fig. 3.1.

phase	$\Pi^{a(b)}_t$	Π^c_t	$\Pi^{a(b)}_s$	Π^c_s
G-AF	1/2	1/2	1/2	1/2
C-AF	1/2	1	1/2	0
A-AF	1	1/2	0	1/2
FM	1	1	0	0

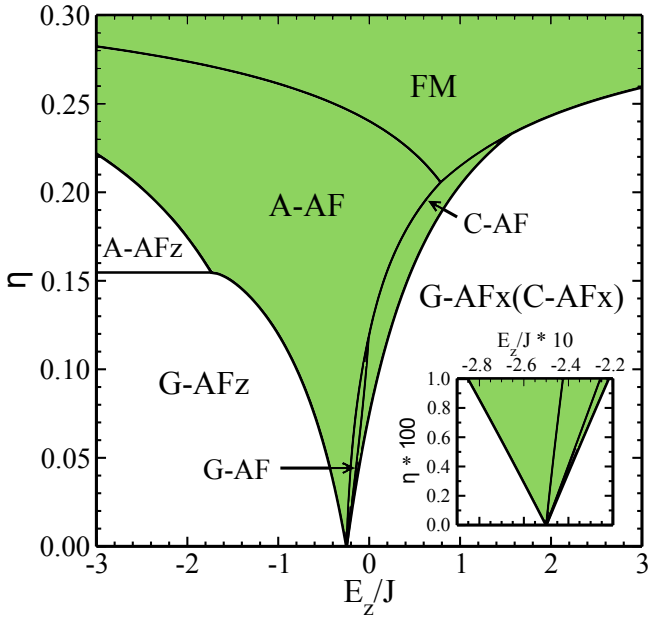

Figure 3.2: Phase diagram of the bilayer KK model obtained in the single-site MF approximation. In this approach the G-AFx and C-AFx phases have exactly the same energy. Shaded green area indicates phases with AO order while the remaining phases are accompanied by FO order with fully polarized x or z orbitals. The magnified area around the multicritical point at $E_z = -0.25J$ and $\eta = 0$ is shown in the inset.

now easily define staggered orbital order parameter of C-type, i.e. C-AO order:

$$t_i^\gamma \equiv \langle \tau_i^\gamma \rangle = \langle \tau_{i\pm\gamma}^{\bar{\gamma}} \rangle. \tag{3.15}$$

The final single-site MF Hamiltonian can be written in the same form for any site so in what follows we will not use site index i anymore. The desired formula is:

$$\mathcal{H}_{\mathrm{MF}}^{(0)} = \sum_\gamma \Theta^\gamma \tau^\gamma + f(t_a, t_c) = \alpha\sigma^z + \beta\sigma^x + f(t_a, t_c), \tag{3.16}$$

with

$$\Theta^\gamma = \frac{1}{2}\xi^\gamma + t^{\bar{\gamma}}(\chi^\gamma - \xi^\gamma) - E_z\delta_{\gamma c}, \tag{3.17}$$

and

$$f(t_a, t_c) = -\frac{1}{8}\sum_\gamma \left\{(\chi^\gamma + \xi^\gamma) + 4t^\gamma t^{\bar{\gamma}}(\chi^\gamma - \xi^\gamma)\right\}. \tag{3.18}$$

For convenience we set $J = 1$ in the above definitions; note that the energy scale can easily be recovered by replacing E_z by E_z/J. As we can see the MF Hamiltonian is very simple and can be written in terms of two Pauli matrices $\{\sigma^x, \sigma^z\}$ with

$$\alpha = \frac{1}{2}\left(\Theta^c - \frac{1}{2}\Theta^a - \frac{1}{2}\Theta^b\right), \quad \beta = \frac{\sqrt{3}}{4}\left(\Theta^a - \Theta^b\right). \tag{3.19}$$

Solving the 2×2 eigenproblem we obtain self-consistency equations for the order parameters t^a and t^c:

$$t^a = \frac{1}{4\Delta}\left(\alpha - \sqrt{3}\beta\right), \quad t^c = -\frac{1}{2\Delta}\alpha, \tag{3.20}$$

where $\Delta = \sqrt{\alpha^2 + \beta^2}$ and the ground state energy given by:

$$E_0 = -\Delta + f(t^a, t^c). \tag{3.21}$$

The solution of self-consistency equations is very elegant and entertaining so we are not going to present it here (the results are given in the Appendix B). It turns out that all four phases considered here can appear as orbitally uniform, i.e., having FO order with orbitals being either perfect clovers or perfect cigars everywhere, or as phases with AO order between two sublattices. The phase diagram presented in Fig. 3.1 was obtained by purely energetic consideration and shows the boarder lines between phases with the lowest energies for given η and E_z. This diagram is surprisingly complex taking into account the simplicity of the single-site approach; it reveals seven different phases. For $\eta = 0$ we have only two AF phases: (i) G-AFz for $E_z < -1/4J$ and (ii) G-AF for $E_z > -1/4J$, with a different but uniform orbital configuration (FO order) which involves either cigar-shaped z orbitals in the G-AFz phase, see Fig. 3.1(c), or clover-shaped x orbitals in the G-AF, see Fig. 3.1(d). Because of the planar orbital configuration in the latter G-AF phase one finds no interplane exchange coupling and thus the spin order along the c axis is undetermined and this phase is degenerate with the C-AF one.

For higher η the number of phases increases abruptly by three phases with AO configurations, as shown in Figs. 3.1(ii) and 3.1(iv): the A-AF, C-AF and G-AF phase respectively. Surprisingly, the AO version of the G-AF phase is connected neither to z nor to x FO order in an antiferromagnet, excluding the multicritical point at $(E_z/J, \eta) = (-0.25, 0)$, and disappears completely for $\eta \approx 0.118$. The C-AF phase stays on top of uniform $G(C)$-AF

phase, lifting the degeneracy of the above phases at relatively large η and then gets replaced by the FM phase which always coexists with AO order. One can therefore conclude that the $G(C)$-AF degeneracy is most easily lifted by turning on the orbital alternation.

On the opposite side of the diagram the G-AFz phase is completely surrounded by A-AF phases: for $\eta > (2/\sqrt{3} - 1)$ the G-AFz phase turns into orbitally uniform A-AFz independently of the value of E_z (interorbital triplet excitations dominate then on the bonds in the ab planes), and for smaller η into the A-AF phase with AO order. In the A-AF phase the AF correlations in the c direction survive despite the overall FM tendency when η grows. This follows from the orbitals' elongation in the c direction present for $E_z < 0$, which would cause interplane singlet formation if we were not working in single-site MF approximation, see Sec. III. In the present case it favors either the G-AFz or A-AF(z) configuration with uniform or alternating orbitals depending on the values of E_z/J and η. Finally, the FM phase is favorable for any E_z if only η is sufficiently close to 1/3 which only confirms that the single-site MF approximation is sound and realistic with this respect.

The central part of the presented diagram is the most frustrated one judging by the number of competing phases with long-range spin order. This behavior is consistent with that found in the 3D SO d^9 model in the regime of $E_z \simeq 0$ and finite η [27]. Four of these phases could be expected by looking at the phase diagram of the 3D model: two G-AF phases, the A-AF phase and the FM phase [27]. Note, however, that in the phases stable in the central part of the phase diagram, namely in the A-AF, C-AF and FM phase, the occupied orbitals alternate. While the FM phase is not surprising in this respect and obeys the Goodenough-Kanamori rule of having FM spin order accompanied by the AO order, in the A-AF one finds an example that both spin and orbital order could in principle alternate between the two ab planes. This finding suggests that in this central part of the phase diagram one may expect either other VB-type phases or even states with more complex SO disorder. Such ordered or disordered phases require a more sophisticated approach that treats explicitly quantum fluctuations on the bonds, either variational wave functions [27, 34], or the embedded cluster approach which we explain below in Sec. 3.2.2.

3.2.2 Cluster mean–field Hamiltonian

Now we introduce a more sophisticated approach which goes beyond the single-site MF approximation of Sec. 3.2.1. In what follows we use a cluster MF approach with a cube depicted in Fig. 3.3. It contains eight sites coupled to its neighbors along the bonds in ab

planes by the MF terms. This choice is motivated by the form of the Hamiltonian with different interactions along the bonds in three different directions — the cube is the smallest cluster which does not break the symmetry between the a and b axes and contains equal numbers of a, b and c bonds. After dividing the entire bilayer square lattice into identical cubes which cover the lattice, the Hamiltonian (3.7) can be written in a cluster MF form as follows,

$$\mathcal{H}_{\mathrm{MF}} = \sum_{C_m \in \mathcal{C}} (\mathcal{H}_m^{\mathrm{int}} + \mathcal{H}_m^{\mathrm{ext}}), \tag{3.22}$$

where the sum runs over the set of cubes $\mathcal{C}$, with individual cube labeled by $C_m \in \mathcal{C}$. Here $\mathcal{H}_m^{\mathrm{int}}$ contains all bonds from $\mathcal{H}_m$ belonging to the cube C_m and the crystal field terms $\propto E_z$ on the cube's sites, i.e., it depends only on the operators on the sites inside the cube, while $\mathcal{H}_m^{\mathrm{ext}}$ contains all bonds outgoing from the cube m and connecting neighboring clusters, making them correlated.

The basic idea of the cluster MF approach is to approximate $\mathcal{H}_m^{\mathrm{ext}}$ by $\tilde{\mathcal{H}}_m^{\mathrm{ext}}$ containing only operators from the cube m. This can be accomplished in many different ways depending on which phase we wish to investigate. Our choice will be to take $\tilde{\mathcal{H}}_m^{\mathrm{ext}}$ of the following form,

$$\tilde{\mathcal{H}}_m^{\mathrm{ext}} = \frac{1}{2} \sum_{\substack{\gamma=a,b \\ i \in C_m}} \{ S_i^z a_i^\gamma + S_i^z \tau_i^\gamma b_i^\gamma + \tau_i^\gamma c_i^\gamma + d_i^\gamma \}, \tag{3.23}$$

containing spin field S_i^z breaking SU(2) symmetry, orbital field τ_i^γ, and SO field $S_i^z \tau_i^\gamma$. Coefficients $\{a_j^\gamma, b_j^\gamma, c_j^\gamma, d_j^\gamma\}$ are the Weiss fields and should be fixed self–consistently depending on E_z and η. Our motivation for such expression is simple: if orbital degrees of freedom are fixed then the problem reduces to the Heisenberg model which has long–range ordered AF phase — that is why we take S_i^z field, the orbitals are present in the Hamiltonian so taking τ_i^γ is the simplest way of treating them on equal footing to describe possible orbital order. Finally, we introduce also SO field $S_j^z \tau_j^\gamma$ because we believe that in some phases spins and orbitals alone do not suffice to describe the symmetry breaking and these operators can act together.

The standard way to seek for a solution is to write self-consistency equations for the Weiss fields. This can be done in a straightforward fashion: we take the operator products from $\mathcal{H}_m^{\mathrm{ext}}$ and divide them into a part depending only on O_i operators from the cube m, and on O_j ones — from a neighboring cube n. Then we use the well known MF decoupling for such

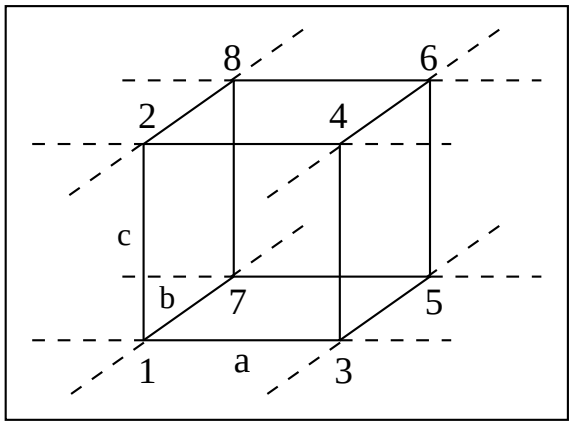

Figure 3.3: Schematic view of the cubic cluster (solid lines) used in the cluster mean-field approach of Sec. 3.2.2, with vertices labeled $i = 1, \cdots, 8$ and bond directions $\gamma = a, b, c$. Dashed lines stand for the outgoing MF terms in the a and b direction which act on the cluster.

operator products,

$$O_i O_j = \langle O_i \rangle O_j + O_i \langle O_j \rangle - \langle O_i \rangle \langle O_j \rangle = O_i \langle O_j \rangle - \frac{1}{2} \langle O_i \rangle \langle O_j \rangle + O_j \langle O_i \rangle - \frac{1}{2} \langle O_i \rangle \langle O_j \rangle, \quad (3.24)$$

and write it in a symmetric way. Now the first two terms can be included into $\tilde{\mathcal{H}}_m^{\rm ext}$ and the last two into $\tilde{\mathcal{H}}_n^{\rm ext}$. This procedure can be applied to all operator products in $\mathcal{H}_m^{\rm ext}$ and full $\tilde{\mathcal{H}}_m^{\rm ext}$ can be recovered in the form given by Eq. (3.23). Repeating this for all clusters leads to a Hamiltonian describing a set of commuting cubes interacting in a self–consistent way. After using Eq. (3.24) on the Hamiltonian Eq. (3.7) we obtain the formulas for the Weiss fields:

$$\begin{aligned}
a_i^\gamma &= \frac{1}{2}(r_2 + r_4) u_i^\gamma + \frac{1}{4}(r_2 - r_1) s_i^\gamma, && (3.25)\\
b_i^\gamma &= -(r_4 + r_1) u_i^\gamma - \frac{1}{2}(r_2 - r_1) s_i^\gamma, && (3.26)\\
c_i^\gamma &= \frac{1}{4}(3r_1 - r_4) t_i^\gamma + \frac{1}{8}(r_2 + r_4), && (3.27)\\
d_i^\gamma &= -\frac{1}{2}(r_1 + r_4) u_i^\gamma u_{m,i}^\gamma - \frac{1}{4}(r_2 - r_1)(s_i u_i^\gamma + s_i^\gamma u_{m,i}^\gamma) \\
&- \frac{1}{16}(r_2 + r_4)(t_{m,i}^\gamma - t_i^\gamma) + \frac{1}{8}(r_4 - 3r_1) t_i^\gamma t_{m,i}^\gamma - \frac{1}{32}(3r_1 + 2r_2 + r_4), && (3.28)
\end{aligned}$$

where the order parameters at site i are:

$$s_i \equiv \langle S_i^z \rangle \quad , \qquad t_{m,i}^{\gamma} \equiv \langle \tau_i^{\gamma} \rangle \, , \qquad u_{m,i}^{\gamma} \equiv \left\langle S_i^z \left(\frac{1}{2} - \tau_i^{\gamma} \right) \right\rangle . \tag{3.29}$$

Note that $\{s_i, t_{m,i}^{\gamma}, u_{m,i}^{\gamma}\}$ are the mean values of operators at site i belonging to the cluster m, and $\{s_i^{\gamma}, t_i^{\gamma}, u_i^{\gamma}\}$ are the mean values of the same operators at sites neighboring with i in the direction γ. The geometry of a bilayer implies that each site i has one neighbor along the axis a and another one along the axis b, and these sites belong to different cubes.

The next crucial step is to impose a condition that $\{s_i^{\gamma}, t_i^{\gamma}, u_i^{\gamma}\}$ are related to the order parameters obtained on the internal sites of the considered cluster. The simplest solution is to assume that all clusters have identical orbital configuration; $t_i^{\gamma} = t_{m,i}^{\gamma}$, spin configuration is in agreement with a type of global magnetic order we want to impose; $s_i^{\gamma} = \pm s_i$ and spin orbital configuration is as if spin and orbitals were factorized, i.e., $u_i^{\gamma} = \pm u_{m,i}^{\gamma}$. This solution has one disadvantage: if a or b direction is favored in the orbital configuration of the cube then this broken symmetry will imply a global symmetry breaking in the lattice which is not expected for the form of the Hamiltonian Eq. (3.7). Therefore, a state with lower energy is expected when two neighboring cubes differ in orbital (and SO) configuration by the interchange of a and b direction, i.e.,

$$s_i^{\gamma} = \pm s_i, \qquad t_i^{\gamma} = t_{m,i}^{\bar{\gamma}}, \qquad u_i^{\gamma} = \pm u_{m,i}^{\bar{\gamma}} \tag{3.30}$$

with $\bar{\gamma}$ being the complementary direction in the ab plane to γ, i.e., $(\gamma, \bar{\gamma}) = (a, b), (b, a)$. This relation gives the same results as the previous one in case when the (a, b) symmetry in the cube is not broken, but keeps the whole system (a, b) symmetric in the other case. Here we again treat the SO field as factorized but surprisingly it turns out that this does not prevent SO entanglement to occur, see below. We have also tried to impose relations between u_i^{γ} and $u_{m,i}^{\gamma}$ which have nothing to do with spin and orbital sectors alone but this only resulted in the lack of convergence of self–consistency iterations.

3.2.3 Self–consistent iterative procedure

The self–consistency equations cannot be solved exactly because the effective cluster Hilbert space is too large even if we use total $\mathcal{S}^z$ conservation in the considered cluster m (then the largest subspace dimension is $d = 17920$) and because of their non–linearity. The way out is to use Bethe–Peierls–Weiss method, i.e., set certain initial values for the order parameters

$\{s_i, t^{\gamma}_{m,i}, u^{\gamma}_{m,i}\}$ and next employ Lanczos algorithm to diagonalize $\mathcal{H}_{\rm MF}$ Eq. (3.22). Below we present results obtained by self-consistent calculations of phases with broken symmetry or with spin disorder. In order to determine the ground state one recalculates mean values of spin, orbital and SO fields given by Eqs. (3.29) and determines new order parameters. This procedure is continued until convergence (of energy and order parameters) is reached. The iteration process can be very slow due to the number of order parameters which is 24 (three per site) for the cube but we have overcome this problem by *imposing* certain symmetry breaking on the cluster. We implement it in the following way: after each iteration we calculate $\{s_i, t^{\gamma}_{m,i}, u^{\gamma}_{m,i}\}$ only for one site $i = 1$ and the remaining coefficients are fixed assuming certain symmetries of the phase we are searching for.

For simplicity let us enumerate the vertices $i = 1, \cdots, 8$ in the cubic cluster as shown in Fig. 3.3. To obtain G-AF phases we assume that

$$s_i = \left\{ \begin{array}{ll} s_1 & if \quad i \in A \\ -s_1 & if \quad i \in B \end{array} \right\}, \tag{3.31}$$

for a two-sublattice structure, where $A = \{1, 4, 5, 8\}$ and $B = \{2, 3, 6, 7\}$ see Fig. 3.3. In the FM case it is enough to put $s_i \equiv s_1$ and in case of FM order within the planes and AF between them (in the A-AF phase) we use instead: $s_i = (-1)^{i-1} s_1$. In the orbital sector we can impose a completely uniform configuration with $t^{\gamma}_{m,i} \equiv t^{\gamma}_{m,1}$, which can however lead to non–uniform configuration of the whole system because neighboring clusters are rotated by $\pi/2$ with respect to each other, or we can produce a phase with AO order taking

$$t^{\gamma}_{m,i} = \left\{ \begin{array}{ll} t^{\gamma}_{m,1} & if \quad i \in A \\ t^{\bar{\gamma}}_{m,1} & if \quad i \in B \end{array} \right\}, \tag{3.32}$$

with $(\gamma, \bar{\gamma}) = (a, b), (b, a)$. Other choices would be to take the above equation either with $A = \{1, 2, 5, 6\}$ and $B = \{3, 4, 7, 8\}$ or with $A = \{1, 3, 5, 7\}$ and $B = \{2, 4, 6, 8\}$. More generally speaking, every choice of orbital sublattices is good as long as the total MF wave function does not violate the symmetry between directions a and b. The sublattices for SO field are constructed as if $u^{\gamma}_{m,1}$ could be expressed as $u^{\gamma}_{m,i} = s_i(\frac{1}{2} - t^{\gamma}_{m,i})$.

3.2.4 Phase diagram with disentangled spin and orbital operators

The zero–temperature phase diagram of the present bilayer d^9 SO model Eq. (3.7) depends on parameters (E_z, η), and was obtained by comparing ground state energies for different sublattices formed by $\{s_i, t^\gamma_{m,i}, u^\gamma_{m,i}\}$ mean fields. In this way we determined the ground state with the lowest energy and its order parameters. We begin with the phase diagram of Fig. 3.4 obtained by assuming that SO operators may be factorized into spin and orbital parts, i.e., $u^\gamma_{m,i} \equiv s_i(1/2 - t^\gamma_{m,i})$ or:

$$\langle S^z_i \tau^\gamma_i \rangle \equiv \langle S^z_i \rangle \langle \tau^\gamma_i \rangle. \tag{3.33}$$

Next we report the phase diagram (in Sec. 3.2.5), where we include $u^\gamma_{m,i}$ calculated following the definition in Eq. (3.29). Comparing these two schemes allows us to determine which phases cannot exist without SO entanglement.

The low–η part of the diagram in Fig. 3.4 is dominated by three phases: VBz for negative E_z, PVB for E_z close to zero and G-AF for positive E_z. The VBz phase with ordered interlayer valence bonds for occupied z orbitals and spin singlets, see Fig. 3.4(c), has replaced the G-AFz phase obtained before in Sec. 3.2.1. Both phases exhibit uniform FO order, i.e., $t^c_{m,i}$ is close to $-1/2$ for all i which means that orbitals take the shape of cigars aligned along the c bonds, see Fig. 3.1(c). One finds that quantum fluctuations which could be included within the present approach select the VBz phase and magnetization vanishes due to the singlets formation. For higher values of $E_z \simeq 0$ also a different phase is found: the plaquette VB (PVB) phase with singlets formed on the bonds in a or b direction of the cluster, see Fig. 3.4(b). This phase breaks the a–b symmetry of the model locally but the global symmetry is preserved thanks to the $\pi/2$ rotation of neighboring clusters, see Eq. (3.30). The orbitals are again uniform within the cluster with $t^a_{m,i}$ or $t^b_{m,i}$ close to $-1/2$, meaning that they take the shape of cigars pointing in the direction of the singlets. For high positive values of E_z the ground state is the G-AF phase with long–range AF order and FO order of x occupied orbitals, i.e., $t^c_{m,i}$ close to $1/2$, see Fig. 3.1(d). This means that orbitals are indeed of the x type and take the shape of four–leaf clovers in the ab plane with lobes pointing along a and b directions which makes the two planes very weakly coupled.

The FO order in the VBz and G-AF phases agrees with the limiting configurations for $E_z \to \pm\infty$ described earlier. The first of them is a quantum phase with local singlets, in contrast to the G-AFz one found already in Sec. 3.2.1 and in the 3D SO d^9 model [27]. If we consider now the VBz phase and increase η, we pass through the VBm phase (where "m" stands for mixed orbital configuration) and reach the A-AF phase with non–zero global

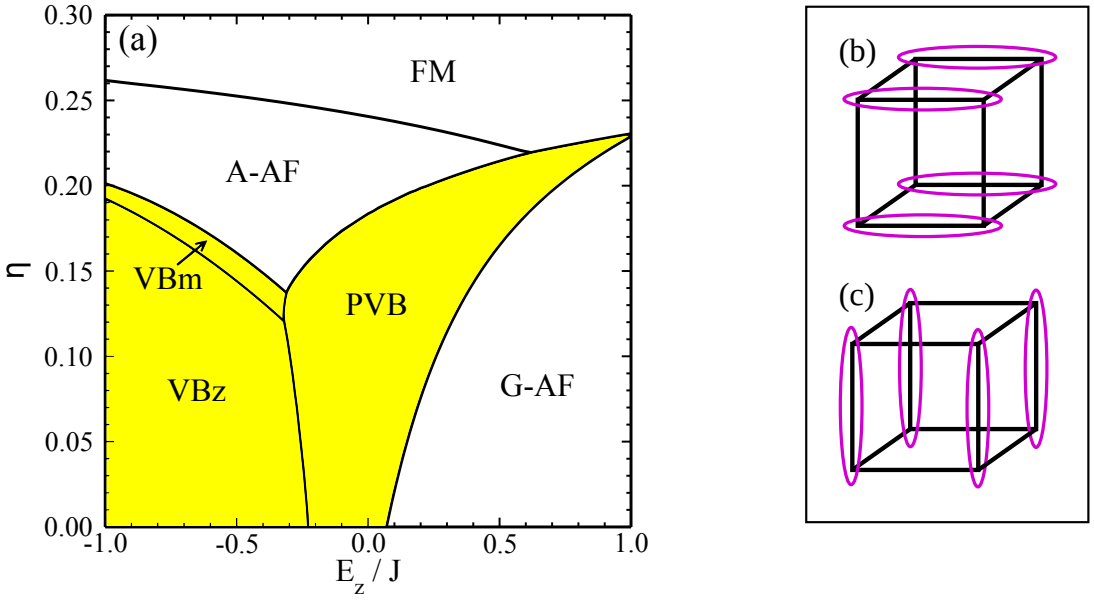

Figure 3.4: Panel (a): phase diagram of the bilayer KK model Eq. (3.22) obtained using cluster MF method with factorized SO operators. Valence-bond phases with spin disorder are stable in the yellow area. Panels (b), (c): schematic view of the two singlet phases on a cube realized in the KK model: (a) plaquette valence bond (PVB) configuration with singlets in ab planes and (b) VBz phase with singlets along the c axis.

magnetization such that spins order ferromagnetically in the ab planes and antiferromagnetically between them (along c axis), see Fig. 3.1(i). We believe that this regime of the phase diagram is of relevance for the spin and orbital correlations in $K_3Cu_2F_7$ and discuss it also in Sec. 3.2.9. The orbital order is of the AO type with $t^c_{m,i}$ close to zero, positive or negative depending on the value of E_z, see Figs. 3.1 (a) and 3.1 (b). The VBm phase occurs when the orbitals in the VBz phase start to deviate from the uniform configuration and ends when the global magnetization appears, accompanied by the change of the orbital order. The first transition is of second order, being the only second order phase transition in the phase diagram of Fig. 3.4 (a).

The presence of both A-AF phases on top of the VBz can be understood qualitatively as follows: in the VBz phase AF spin coupling is strong only within the singlets, so if η is increased the weak in-plane spin correlations can easily switch to FM ones, while AF correlations will still survive between the planes. The last phase of the diagram is the FM phase with AO order, similar to the AO order in the A-AF phase. Due to the absence of thermal and quantum fluctuations the magnetization in this phase is constant and maximal. The FM phase appears for any E_z, if only η is sufficiently close to 1/3, which agrees qualitatively

with the previous discussion of the exact limiting configurations and with the phase diagram found before in the single-site MF approach, see Fig. 3.2. This demonstrates that this phase is insensitive to quantum fluctuations on the bonds in the considered cubic cluster.

Comparing Fig. 3.4 (a) to the MF phase diagram of Fig. 3.2 we can immediately recognize the main difference: the existence of the VBz and PVB phases. These phases contain spin singlets on the bonds and do not follow from the single-site MF approach. Another difference is the lack of sharp transitions between AO and FO order within one phase; these transitions are smoothened by spin fluctuations absent in the single-site mean field and perfect FO configurations are now available only for extremely high values of $|E_z|$.

3.2.5 Phase diagram with spin-orbital field

When the SO mean field is not factorized but calculated according to its definition given in Eq. (3.29), one finds the modified phase diagram displayed in Fig. 3.5. We would like to emphasize that this non-factorizability cannot be included within the single-site MF approach because there all spin fluctuations are absent. Of course, one can imagine that we take the $S_i^z\langle S_{i+\gamma}^z\rangle$ decoupling in the pure-spin sector and $S_i^x\langle S_{i+\gamma}^x\rangle$ decoupling in the SO sector of the Hamiltonian Eq. (3.7) leading to the fluctuating spins but this would break both the magnetization conservation and homogeneity of the spin-spin interactions included into the Kugel-Khomskii model.

In addition to the phases obtained in the phase diagram of Fig. 3.4, we get here also the following phases: ESO, EPVB and PVB-AF (the VBm phase is still stable between the VBz and A-AF ones but within a much smaller area). The first two above phases are formed in the highly frustrated region of the phase diagram where both E_z and η are moderate. ESO stands for entangled SO phase and is characterized by relatively high values of SO order parameters, especially for high η values when other order parameters are close to zero. This phase contains singlets along the bonds parallel to the c axis, its magnetization vanishes and the orbital configuration is uniform. One can say that this is the VBz phase with weakened orbital order transformed into uniform SO order for the same spin and orbital sublattices. EPVB stands for entangled PVB phase and resembles it, but has in addition finite non–uniform SO fields, and weak global AF order. A different type of phase with SO entanglement is the PVB-AF phase connecting PVB and G-AF in a smooth (as it will be shown below) way but only if η is large enough. In contrast to the direct PVB-to-G-AF transition, passing through the PVB-AF involves second order phase transitions and the

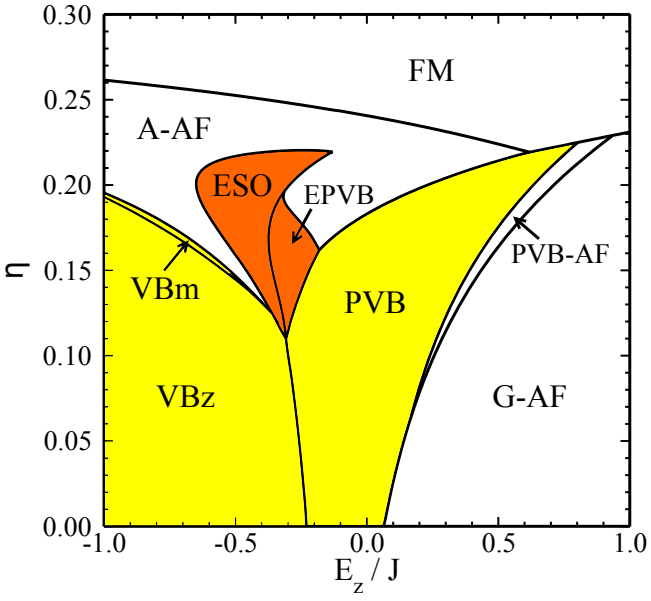

Figure 3.5: The phase diagram of the cluster MF Hamiltonian Eq. (3.22) of the KK model for a bilayer, with independent spin, orbital and SO mean fields. Valence-bond phases with spin disorder are stable in the yellow area, and phases with SO entanglement are indicated by orange shading.

same happens in case of the EPVB connecting the ESO and PVB phases. Similarly to the previous diagram, the transition from the VBz to VBm phase is of the second order while the other transitions produce discontinuities in order parameters (see Sec. 3.2.6) and correlation functions (see Sec. 2.1.2).

Finally, we should also point out that the G-AF/C-AF degeneracy found in Fig. 3.2 is lifted in the cluster approach and the C-AF phase does not appear in any of the two phase diagrams presented in Figs. 3.4 and 3.5. Another interesting feature of the phase diagrams are points of high degeneracy where different phases have the same ground-state energies. In case of the single-site MF diagram this quantum critical point is found at $(E_z = -1/4J, \eta = 0)$, where six phases meet. The use of cluster MF method which includes singlet phases lifts this point upwards along the border line between VBz and PVB to $(E_z, \eta) \approx (-0.3J, 0.11)$ in case of Fig. 3.5. This means that singlet formation acts against interaction frustration caused by Hund's exchange coupling and moves the most frustrated region of phase diagram to finite-η regime. This shows once again that the simple single-site approach is not sufficient to describe correctly the properties of the bilayer d^9 SO model.

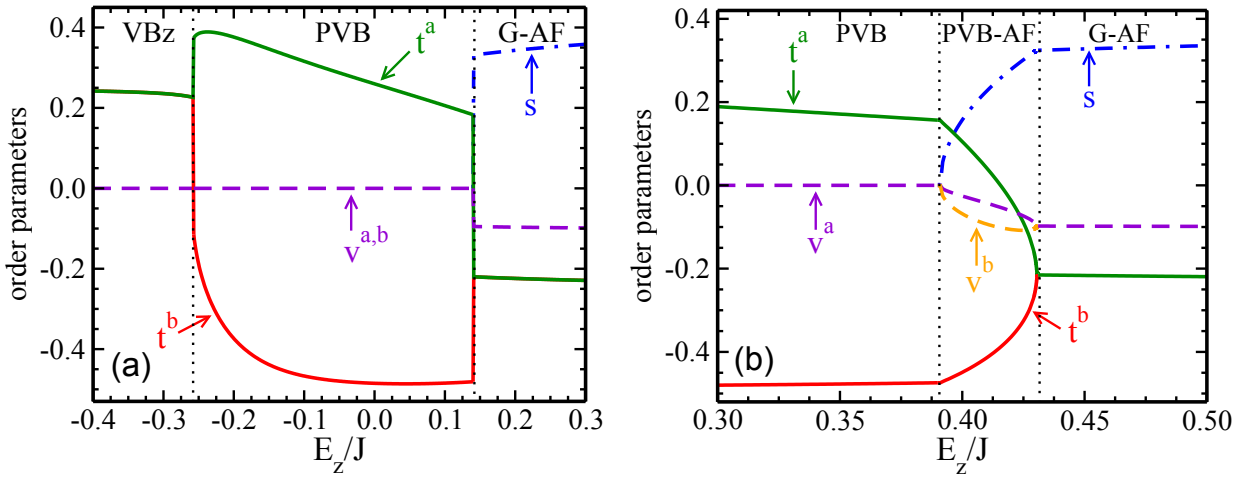

Figure 3.6: Panel (a): order parameters $\{s, t^{a,b}, v^{a,b}\}$ for $\eta = 0.05$ and $-0.4 < E_z/J < 0.3$ in the VBz, PVB and G-AF phase, from left to right. Panel (b): order parameters $\{s, t^{a,b}, v^{a,b}\}$ for $\eta = 0.15$ and $0.3 < E_z/J < 0.5$ in the PVB, PVB-AF and G-AF phase, from left to right.

3.2.6 Order parameters

The ground state is characterized by order parameters obtained directly during the self–consistency iterations in each phase: spin, orbital and SO order parameters, $\{s_1, t^{a,b}_{m,1}, u^{a,b}_{m,1}\}$. We focus here on orbital and spin order in the configurations showed in the phase diagram of Fig. 3.5 (for study of the SO order parameters see Ref. [106]). One can investigate the behavior of order parameters along different cuts of the phase diagram of Fig. 3.5 and determine from it types of phase transitions. Below we present a few representative results. For this purpose we first choose $\eta = 0.05$ and start within the VBz phase, where by increasing E_z one gets first into the PVB and next to G-AF phase, see Fig. 3.6(a). For $\eta = 0.15$ there are even more phases and one passes through the A-AF, ESO, EPVB, PVB, and AF-PVB phases, before reaching finally the G-AF phase, see Figs. 3.6(b) and 3.7(a). We also investigated the dependence of order parameters on Hund's exchange coupling — we fixed $E_z = -0.72J$, started in the VBz phase and increased η to get to the VBm and A-AF phases — these results are shown in Figs. 3.7(b).

In what follows we use shorthand notation for the order parameters,

$$\{s, t^{a,b}, v^{a,b}\} \equiv \{s_1, t^{a,b}_{m,1}, v^{a,b}_{m,1}\}. \tag{3.34}$$

In Fig. 3.6(a) we displayed the order parameters for increasing E_z in phases VBz, PVB and G-AF (separated by dotted lines in the plot). The sublattice magnetization s is non–zero

only in the G-AF phase because the remaining phases are of the VB crystal type, with spin singlets oriented either along the c direction or in the ab planes. In the G-AF phase the spin order grows stronger for increasing E_z when the orbital fluctuations weaken and spin fluctuations present in the G-AF phase reduce s from the classical value of $1/2$.

Consider now decreasing values of E_z in Fig. 3.6. Both orbital order parameters remain equal and close to $-1/4$ in the G-AF phase until the (first order) transition to the PVB phase occurs, where orbital configuration changes abruptly and becomes anisotropic. In this case the a–b symmetry was broken in such a way that that spin singlets point in the PVB phase in b direction, in agreement with the directional orbitals (cigars). This explains the robust orbital order with t^b being close to $-1/2$ in most of the PVB phase. The global symmetry is not broken as the VB singlets form here a checkerboard pattern in the ab plane, with AO order of directional orbitals along the a and b axis in the neighboring plaquettes. The transition to the VBz phase is discontinuous (first order) in the orbital sector too: t^a grows constantly while decreasing E_z down to $0.4J$, drops slightly close to the transition point and jumps to $1/4$ in the VBz phase, t^b grows quickly to $t^b \approx 0.125$ while approaching the transition and then jumps to the value of t^a. Qualitatively this means that close to the above transition the orbital cigars pointing along the b axis change gradually into a shape very similar to clover orbitals lying in the bc plane and then suddenly the lobes along the b direction disappear and we are left with the pure VBz phase.

Figure 3.6(b) shows that the transition between the PVB and G-AF phases can have a completely different character than described above. The difference comes from a higher value of η which is now equal to 0.15, enhancing the FM channel of superexchange and leading to the intermediate PVB-AF phase and eventually to a smooth transition from the PVB to G-AF phase. In the PVB-AF phase staggered magnetization s grows continuously from zero (in the PVB) to a finite value in the G-AF phase and remains saturated there. This means that planar singlets in the PVB phase decay gradually and spins get partially "synchronized" with orbitals, moving toward uniform configuration. This mechanism of the PVB-to-G-AF transition is absent for low values of η — we anticipate that the enhanced FM component of interactions reduces spin fluctuations which makes the correlations between spins and orbitals possible.

In Fig. 3.7(a) we focus on the complementary regime of the phase diagram, $\eta = 0.15$ and negative E_z. In this regime we describe three different consecutive phase transitions between the phases: ESO, EPVB and PVB. Note that the ESO phase has predominantly z orbitals accompanied by fluctuations, i.e., $t^c \simeq -0.4$ and $t^a = t^b$, and may be seen as an

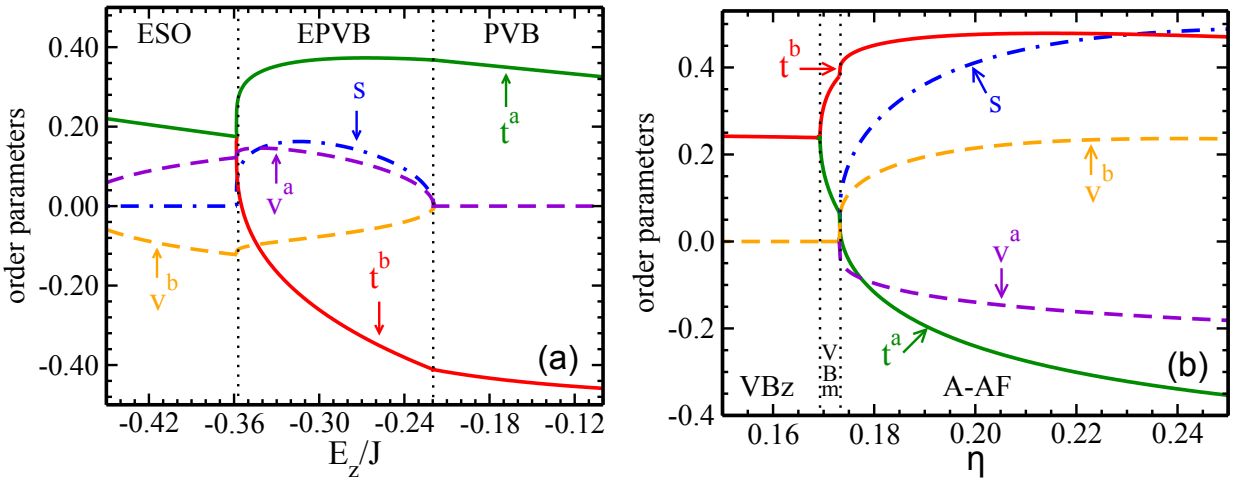

Figure 3.7: Panel (a): order parameters $\{s, t^{a,b}, v^{a,b}\}$ for $\eta = 0.15$ and $-0.39 < E_z/J < -0.1$ in the ESO, EPVB and PVB phases, from left to right. Panel (b): order parameters $\{s, t^{a,b}, v^{a,b}\}$ for $E_z = -0.72J$ and $0.15 < E_z/J < 0.25$ in the VBz, VBm and A-AF phases, from left to right.

extension of the VBz phase. On the contrary, the second quantum EPVB phase which occurs in the phase diagram of Fig. 3.5 may be seen as a precursor of the PVB phase characterized by finite staggered magnetization s which grows smoothly from the zero values at the phase borders meaning that we have a wedge of antiferromagnetism between two VB configurations. The EPVB phase seems to be similar to PVB-AF in a sense that non-uniform orbital order accompanies finite AF magnetization.

Next Fig. 3.7(b) shows the behavior of order parameters for $E_z = -0.72J$ and η changing in an interval allowing us to study the transitions from the VBz to VBm phase, and between the VBm and A-AF phase. In this case all the phases can be described by the same spin and orbital sublattices because VBz is uniform in the orbital sector and has no long–range magnetic order so it can be described both in terms of the PVB and A-AF type of ordering. Global magnetization appears only in the A-AF phase jumping from the zero value in the VBm and growing with increasing η. Transition from the VBz to VBm phase is continuous in both spin and orbital sectors.

The orbital order parameters $t^{a,b}$ bifurcate in Fig. 3.7(b) at $\eta \simeq 0.169$ from the isotropic value $t^a = t^b \simeq 1/4$ and the orbital anisotropy grows in the VBm phase to give AO order in the A-AF phase, and next shows a discontinuity at the second transition. The final AO order can be described by clover orbitals with symmetry axes alternating between a and b directions from site to site. Relatively big, negative value of t^a means that the clovers' lobes

are elongated in the a or b direction, perpendicular to their axes. The elongation depends also on the value of E_z: the $E_z \to -\infty$ limit corresponds to pure cigars, while for $E_z \to \infty$ one gets pure clover-like orbitals. This tendency is especially visible in the FM phase which is not limited in horizontal direction of the phase diagram. Consequently, the VBm phase can be regarded as a crossover regime between orbitally uniform VBz and alternating A-AF phases. This resembles to some extent the PVB-AF phase described earlier but we want to emphasize the main difference between these phases: the VBm phase does not need non–factorizable SO mean field to appear while the PVB-AF one needs it (compare Figs. 3.4 and 3.5). The question of SO non–factorizability will be addressed in more details below, see Sec. 3.2.8.

3.2.7 Nearest-neighbor correlations

Studying order parameters in different phases we get complete information about symmetry broken or disordered phases of the system, but this alone does not justify the use of the cluster MF method as order parameters can in principle be obtained using standard single-site MF approximation, see Sec. 3.2.1. The advantage of the cluster method becomes evident when we investigate correlation functions on the bonds belonging to the considered cube. The most obvious ones are the spin–spin correlations $\langle \mathbf{S}_i \cdot \mathbf{S}_j \rangle$ or orbital–orbital correlations $\langle \tau_i^\gamma \tau_j^\gamma \rangle$. Although one could in principle invent several other bond correlation functions, the above ones have the most transparent physical meaning because they enter the Hamiltonian (together with correlations of the SO type, not shown here– see Ref. [106]). For the same reason we will only consider orbital correlation functions for different bond direction $\gamma = a, b, c$. For symmetry reasons it is enough to consider only one chosen vertex, e.g. vertex number 1 in Fig. 3.3. For convenience we will use the following notation:

$$C_s^\gamma \equiv \langle \mathbf{S}_1 \cdot \mathbf{S}_i \rangle, \qquad C_t^\gamma \equiv \langle \tau_1^\gamma \tau_i^\gamma \rangle \tag{3.35}$$

where the bond $\langle 1i \rangle || \gamma$ and $i \in \{2, 3, 7\}$ which gives all nonequivalent NN correlations along $\gamma = a, b, c$ (see Fig. 3.3).

In what follows we will present the numerical results for bond correlations $\{C_s^\gamma, C_t^\gamma\}$ along different cuts of the phase diagram of Fig. 3.5. For all two–panel plots each panel describes correlation of one type: upper panel — spin correlations, bottom one — orbital correlations. For each panel different line characters and colors indicate different direction γ: solid red line stands for $\gamma = c$, dashed green line for $\gamma = a$ and dashed–dotted blue line for $\gamma = b$. In

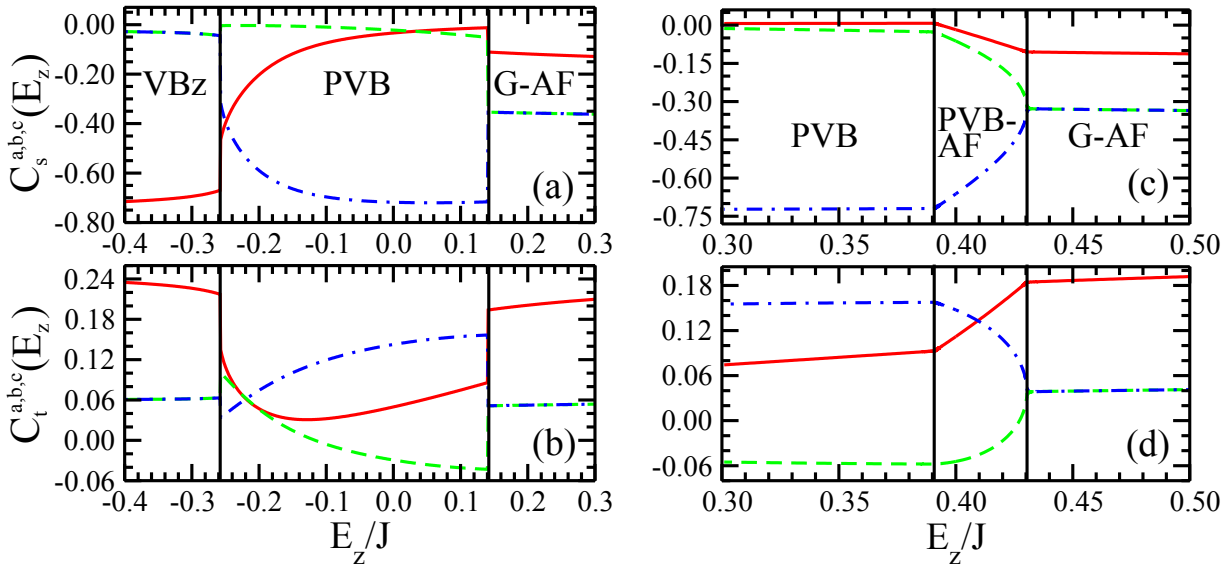

Figure 3.8: Panels (a)–(b): NN correlations for $\eta = 0.05$ and $-0.4 < E_z/J < 0.3$ in the VBz, PVB and G-AF phases. (a) Spin correlations: solid red line — C_s^c, dashed green line — C_s^a and dashed–dotted blue line — C_s^b. (b) Orbital correlations: solid red line — C_t^c, dashed green line — C_t^a and dashed–dotted blue line — C_t^b. Panels (c)–(d): NN correlations for $\eta = 0.15$ and $0.3 < E_z/J < 0.5$ in the PVB, PVB-AF and G-AF phases. (c) Spin correlations: solid red line — C_s^c, dashed green line — C_s^a and dashed–dotted blue line — C_s^b. (d) Orbital correlations: solid red line — C_t^c, dashed green line — C_t^a and dashed–dotted blue line — C_t^b.

order to investigate the effects of quantum fluctuations we focus the discussion on two types of quantum phases: (i) singlet phases (PVB and VBz phase), and (ii) entangled SO phases (ESO and EPVB phase).

Singlet phases

We begin with bond correlation functions for $\eta = 0.05$ and $-0.4 < E_z/J < 0.3$ in the VBz, PVB and G-AF phase. The C_s^c function stays close to $-3/4$ in the VBz phase while the other spin correlations are almost zero as one can expect in the interlayer singlet phase, see Fig. 3.8(a). After the first transition at $E_z \simeq -0.26J$ the situation changes — now the singlets are in b direction and C_s^b gets close to $-3/4$ when E_z increases. After the second transition at $E_z \simeq 0.14J$ all the spin correlations take finite negative values with C_s^c relatively weakest, keeping the symmetry between a and b direction. This is in agreement with the spin order in the G-AF phase discussed in Sec. 3.2.6.

The orbital correlation functions in the VBz and G-AF phases behave as if the orbitals were frozen in a uniform configuration with $t^c = \pm 1/2$ and $t^{a,b} = \mp 1/4$ whereas in the PVB phase their behavior is more nontrivial; the dominant C_t^b is quite distant from its maximal value 1/4 and the difference between C_t^a and C_t^c is also visible, especially close to the G-AF phase, see Fig. 3.8(b). This result is due to quantum fluctuations: perfect VBz and G-AF configurations are the exact eigenstates of the Hamiltonian, at least in the limit of large $|E_z|$, while perfect PVB state cannot be obtained exactly in any limit and gets easily destabilized by varying E_z. It is peculiar that the spin configuration is almost nonsensitive to the orbital splitting E_z and the singlets stay rigid in the regime of spin disordered phases, i.e., below the transition to the G-AF phase.

Figures 3.8(c)–3.8(d) present the bond correlations for a gradual transition between the PVB and G-AF phases, with an intermediate PVB-AF phase for $\eta = 0.15$ and $0.3 < E_z/J < 0.5$. By decreasing E_z, i.e., looking from right to left, we can see the in–plane spin correlation bifurcating smoothly at the transition to the PVB-AF phase and evolving monotonically to the values characteristic of the PVB phase, see Fig. 3.8 (c). The interplane spin correlations C_s^c stay relatively weak everywhere which is obvious in both PVB and G-AF phase and hence not so surprising in the intermediate PVB-AF phase.

In the orbital sector we can see here very similar behavior to the one observed in Fig. 3.8(b)— again the order is far from the perfect PVB phase but C_t^c is close to the classical value of 1/16 obtained for the plane perpendicular to two directional orbitals along the b axis, while C_t^a is almost exactly opposite and C_t^b stays below 1/4, see Fig. 3.8(d). This shows some kind of universality at the transition from the PVB to G-AF phase which is independent of the intermediate phase.

Phases with entangled spin-orbital order

Consider now negative values of E_z and intermediate η, where unexpected and qualitatively new entangled phases occur in the phase diagram of Fig. 3.5. We display bond correlation functions in Fig. 3.9(a)–3.9(b) in two neighboring highly frustrated and entangled phases, the ESO and EPVB phase — the latter one turns into the PVB phase when E_z is increased. The relevant parameter range for $\eta = 0.15$ is $-0.45 < E_z/J < -0.1$. On the first glance this plot shows that the transitions between the ESO and EPVB as well as between the EPVB and PVB phases are of the second order. In the spin sector one observes weakening singlet order in the ESO phase with C_s^c getting far from $-3/4$ and practically vanishing in-plane

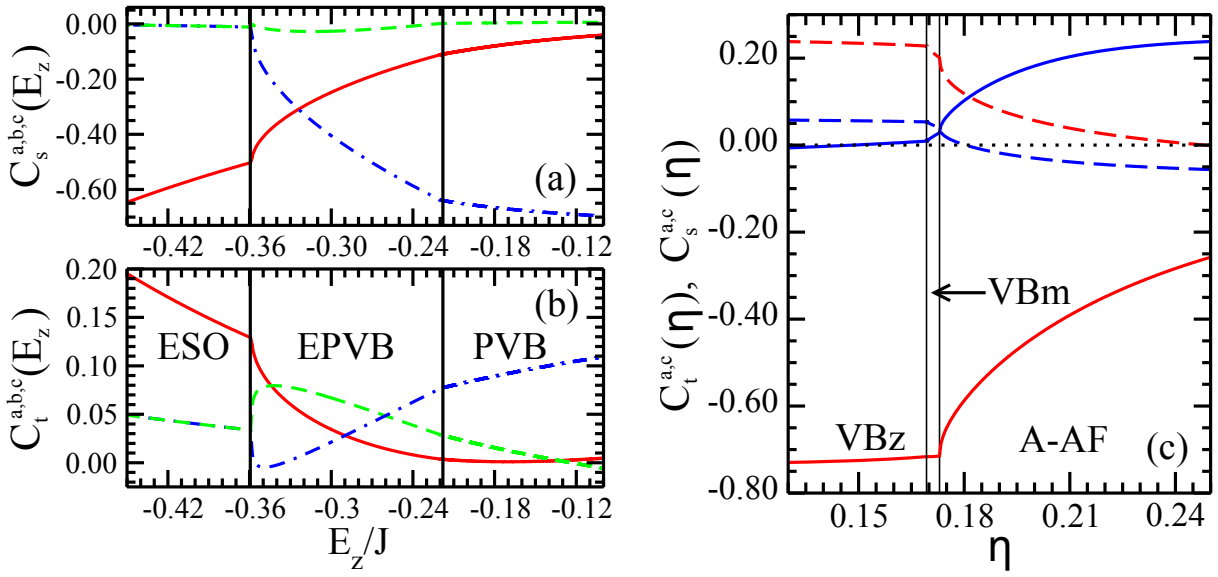

Figure 3.9: Panels (a)–(b): NN correlations for $\eta = 0.15$ and $-0.45 < E_z/J < -0.1$ in the ESO, EPVB and PVB phases. (a) Spin correlations: solid red line — C_s^c, dashed green line — C_s^a and dashed–dotted blue line — C_s^b. (b) Orbital correlations: solid red line — C_t^c, dashed green line — C_t^a and dashed–dotted blue line — C_t^b. Panel (c): NN correlations for $E_z = -0.72J$ and $0.10 < \eta < 0.25$ in the VBz, VBm and A-AF phases. Correlations along the c axis: solid red line — C_s^c, dashed red line — C_t^c. Correlations within ab plane: blue solid line — C_s^a , blue dashed line — C_t^a.

correlations $C_s^{a,b}$, see Fig. 3.9(a). After the first transition (at $E_z \simeq -0.36J$) C_s^b grows rapidly toward negative values while C_s^c goes to zero much more gently and C_s^a stays close to zero. This means that in the EPVB phase we have relatively strong AF order in the bc plane inside the cluster, turning into the ac plane order on neighboring cubes. This gives finite magnetization s shown in Fig. 3.7(a). When approaching the second transition (at $E_z \simeq -0.22J$) C_s^c weakens and C_s^b gets closer to $-3/4$ and this is continued within the PVB phase.

In the orbital sector we can find other differences between entangled and disentangled phases, see Fig. 3.9(b). In the ESO phase the C_t^c drops considerably when approaching the first transition; this is in contrast with the VBz phase where C_t^c stays almost constant until the transition occurs. The behavior of in-plane correlation functions $C_t^{a,b}$ becomes somewhat puzzling within the EPVB phase: after bifurcation at the transition point C_t^b drops to zero and slowly recovers to become dominant in the PVB phase, while C_t^a stays dominant in certain region of the EPVB phase even though the spin correlations in the$a$ direction vanish.

Only C_t^c gradually drops to zero throughout all three phases.

In the last figure, Fig. 3.9(c), we display bond correlation functions in the VBz, VBm and A-AF phases for $E_z = -0.72J$ and $0.10 < \eta < 0.25$. All three phases exhibit a tendency towards AO order with two sublattices which does not violate the a–b symmetry inside the cube; for this reason we show only correlations along the c and a direction. The plots prove that the transition from the VBz to VBm phase is of the second order while the transition from the VBm to A-AF phase produces no discontinuities in correlations either, but the behavior of order parameters (see Fig. 3.7(b)) is here slightly discontinuous. In the spin sector we observe first (at $\eta < 0.17$) that robust singlets along the c axis with $C_s^c \simeq -0.7$ are gradually weakened under increasing η and weak FM correlations occur in the VBz phase close to the first phase transition to the VBm order. We suggest that this regime of parameters could correspond to $K_3Cu_2F_7$, where the magnetic properties indicate interplanar singlets are formed in the VBz and VBm phases, accompanied by weak FM correlations in the ab planes [105].

Note that the changes in spin correlations with increasing η become fast only after leaving the VBm phase. In the orbital sector perfect VBz order dies out quickly already in the VBm regime, both on the bonds along the c and a axes. After entering the A-AF phase, C_t^c vanishes exponentially while C_t^a crosses zero and gradually falls to negative values. This behavior is in agreement with that shown in Fig. 3.7(b) saying that t^c remains close to zero in the A-AF phase and the negative C_t^a confirms AO order in ab planes.

3.2.8 Spin–orbital entanglement

The essence of spin-orbital entanglement observed in the cluster MF approach is SO non-factorizability. This feature can have either on-site or bond character, the latter was introduced in Ref. [32]. We emphasize that on-site entanglement which occurs when spin-orbit coupling is finite [107], occurs also in the present superexchange model as shown below. We define the on-site entanglement as non-separability of the order parameters, i.e., spin and orbital operators are entangled when $v^\gamma \neq st^\gamma$, while the entanglement is being of bond type when $C_{st}^\gamma \neq C_s^\gamma C_t^\gamma$, with:

$$v^\gamma \equiv \langle S_1^z \tau_1^\gamma \rangle \,, \qquad C_{st}^\gamma \equiv \langle (\mathbf{S}_1 \cdot \mathbf{S}_i) \tau_1^\gamma \tau_i^\gamma \rangle. \tag{3.36}$$

The first quantity can be easily calculated out of the SO mean field as $v^\gamma = \frac{1}{2} s_1 - u_{m,1}^\gamma$. Therefore we analyze in this Section the numerical results for the covariances motivated by

the above discussion which are defined as follows:

$$r^{\gamma} = v^{\gamma} - st^{\gamma}, \qquad R^{\gamma} = C^{\gamma}_{st} - C^{\gamma}_{s} C^{\gamma}_{t}. \tag{3.37}$$

In case of r^{γ} we consider only $\gamma = a, b$ as the on-site covariance satisfy the local constraint,

$$r^{c} = -r^{a} - r^{b}, \tag{3.38}$$

while for R^{γ} we shall present the data for $\gamma = a, b, c$. In order to quantify the above non-factorizability and to recognize whether it is strong or weak in a given phase, it is necessary to establish first the minimal and maximal values of R^{γ} and r^{γ}. Simple algebraic considerations give the following inequalities: the bond covariances $|R^{\gamma}| < 0.25$ in singlet phases, $|R^{\gamma}| < 0.125$ in phases with magnetic order, and the on-site covariances $|r^{\gamma}| < 0.25$ everywhere.

First of all, the numerical results show that both bond and on-site SO entanglement quantified by Eqs. (3.37) is small in the regime of weak Hund's exchange coupling. This feature is illustrated in Fig. 3.10(a) for the VBz, PVB and G-AF phases at $\eta = 0.05$ and $-0.4 < E_z/J < 0.3$. The $r^a = r^b$ curves show no on-site SO entanglement ($r^{\gamma} = 0$) in both VBz and PVB phases, while it is finite in the G-AF phase ($r^a = r^b < 0$) and gradually approaches zero with increasing E_z. We emphasize that this on-site non-factorizability is minute, being one order of magnitude smaller than its maximal value, and does not play any important role for the stability of the G-AF ground state. This is confirmed by the fact that G-AF phase exists in the same region of parameters in both phase diagrams: factorizable (Fig. 3.4) and non-factorizable one (Fig. 3.5), and occurs even in the single-site MF approximation (Fig. 3.2). It is interesting to note that the in-plane bond entanglement $R^{a,b}$ takes relatively high values in the G-AF phase. This is clearly an effect of quantum fluctuations; the perfect (classical) G-AF phase of Fig. 3.2 has a uniform frozen x orbital configuration with $t^c = 1/2$ which suppresses any non-factorizability. As the on-site entanglement, also the bond SO entanglement vanishes gradually for high values of $E_z \to \infty$.

At the border line between the VBz and PVB phases we noticed a considerable increase of R^c and less pronounced growth of R^b which seem to be induced by the transition as $R^{b,c}$ drop quickly for higher values of E_z. In the VBz phase we expect all the SO covariances to be zero for the same reasons as in the G-AF phase and this also applies to the perfect PVB phase. In Fig. 3.10(a), however, the VBz and PVB phases are dominated by the critical behavior which distorts perfect orderings.

Also in the regime of higher Hund's exchange interaction $\eta = 0.15$ the SO covariances in

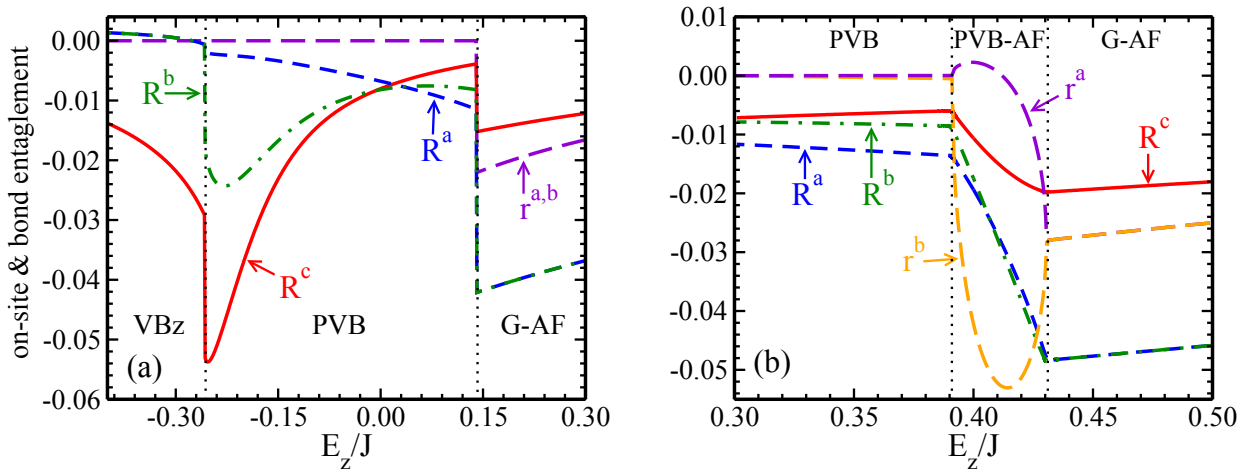

Figure 3.10: Evolution of on-site r^γ and bond R^γ entanglement parameters with increasing E_z for: (a) $\eta = 0.05$ and $-0.4 < E_z < 0.3$ in the VBz, PVB and G-AF phases; (b) $\eta = 0.15$ and $0.3 < E_z/J < 0.5$ in the PVB, PVB-AF and G-AF phases.

the PVB, PVB-AF and G-AF phases are small in the range of their stability, see Fig. 3.10(b) for $0.3 < E_z/J < 0.5$. In the PVB phase all the covariances take small values showing that the PVB type of order has no serious quantum fluctuations in this parameter range. The on-site covariances $\{r^a, r^b\}$ bifurcate from the zero value at the first transition and this emergence of non-factorizability stabilizes here the intermediate PVB-AF phase (compare Figs. 3.4 and 3.5) and persists in the G-AF phase where they overlap again ($r^a = r^b$). In the regime of PVB-AF phase we observe also almost linear decrease of the in-plane $R^{a,b}$ staying close to each other and a smaller drop of R^c. Although these quantities are all small, the order parameters (see Fig. 3.6(b)) are small too, so we conclude that SO entanglement is qualitatively important here. The minimum of all R^γ is located at the second transition indicating that highly entangled states play a role also at the onset of the G-AF phase.

Figure 3.11(a) shows SO entanglement in the most exotic part of the phase diagram where the ESO, EPVB and PVB phases compete, i.e., for $\eta = 0.15$ and $-0.45 < E_z/J < -0.1$. The on-site SO covariances $\{r^a, r^b\}$ take high, opposite values in both the ESO and EPVB phase, with maximum (minimum) at the transition line between them. Comparing to other phases $r^{a,b}$ values are highest in the ESO and EPVB phases, and comparing the two phase diagrams shown in Figs. 3.4 and 3.5, we recognize that SO entanglement is a constitutive feature of both ESO and EPVB states. We emphasize that the on-site SO entanglement is strong and complementary in the ESO phase on the bonds along the a and b direction ($r^a = -r^b$), while it vanishes between the ab planes ($r^c = 0$). These results indicate SO fluctuations in

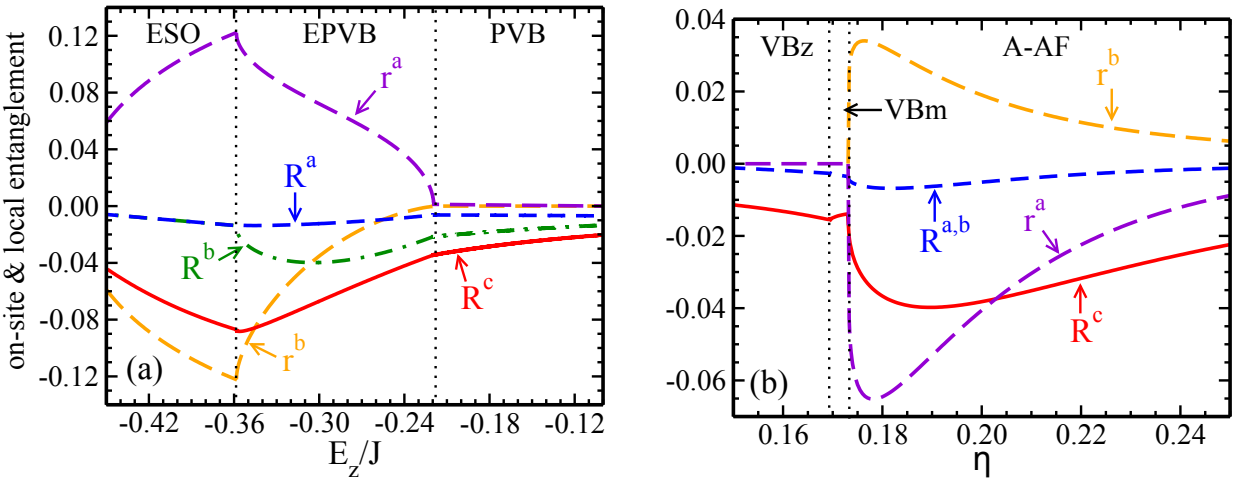

Figure 3.11: On-site r^γ and bond R^γ entanglement parameters for: (a) $\eta = 0.15$ and $-0.45 < E_z/J < -0.1$ in the ESO, EPVB and PVB phases; (b): $E_z = -0.72J$ and $0.15 < \eta < 0.25$ in the VBz, VBm and A-AF phases.

the ab planes, with $\langle S^z \sigma^x \rangle \neq 0$ and no fluctuations along the c axis, where r^c follows from $\langle S^z \sigma^z \rangle = 0$. In contrast, in the EPVB phase there is also finite on-site entanglement for the interlayer order parameters, $r^c \neq 0$.

Looking at the bond parameters R^γ we see that the dominant one is R^c falling gradually in the ESO down to the minimum at the ESO-EPVB transition. At the same point R^b drops from zero value in the ESO phase and takes maximally negative value inside the EPVB regime. In contrast, R^a remains close to zero in the entire regime of parameters and in the PVB all the covariances go to zero showing that the order within the PVB phase is practically disentangled. The dominant role of R^c comes from the c–axial symmetry of the ESO phase and increased quantum fluctuations on the ESO-EPVB border while the non-zero value of R^b in the EPVB phase follows from the magnetic and orbital order on the cube in the bc plane mentioned in the previous section.

Finally, we focus on the range of large negative crystal field splitting $E_z = -0.72J$ and display the SO covariances in the VBz, VBm and A-AF phases for increasing Hund's exchange $0.15 < \eta < 0.25$, see Fig. 3.11(b). On the one hand, looking at the VBm region of the plot we can understand why this phase can exist when factorized SO mean field is applied (again, compare Figs. 3.4 and 3.5); the on-site covariances $\{r^a, r^b\}$ vanish here and within the VBz phase. On the other hand, one finds certain on-site entanglement in the A-AF phase, especially close to the transition line — this shows why the A-AF area is expanded in Fig. 3.5 as compared with the non-factorized phase diagram of Fig. 3.4. Concerning bond

entanglement, it is significant (finite $R^c < 0$) only along the interlayer c bonds in all these three phases, taking maximal values of $|R^c|$ in the A-AF phase. One can understand this as follows: in the VBz phase the orbital order is almost perfect and orbitals stay frozen — therefore SO factorization is here almost exact as indicated by a low value of R^c. This is not the case in the A-AF phase where orbitals fluctuate, especially close to the transition line to the VBm phase. The $R^{a,b}$ bond parameters are small due to the imposed FM order within the ab planes which decouples the spin from orbital fluctuations on the bonds along the a and b directions.

3.2.9 Summary and conclusions

The numerical results presented in the last sections, obtained using the sophisticated mean-field approach empoying an embedded cubic cluster, provide a transparent and rather complete picture of possible ordered and disordered phases in the bilayer SO d^9 model. This approach is well designed to determine the character of spin, orbital and SO order and correlations in all the discussed phases as it includes the most important quantum fluctuations on the bonds and captures the essential features of SO entanglement. By analyzing order parameters we also presented evidence which allowed us to identify essential features of different phases and to distinguish between first and second order phase transitions. This is especially important in cases when two phases are separated by an intermediate configuration, such as the PVB-AF or VBm phase, where one finds a gradual evolution from singlet to AF correlations, supported (or not) by non-factorizable SO order parameter. We believe that the cluster mean-field approach presented here and including the joint SO order parameter is more realistic because there is no physical reason, apart from the form of the d^9 Hamiltonian, to treat spin and orbital operators as the only fundamental symmetry-breaking degrees of freedom in any phase.

Interestingly, the results show that the bottom part of the phase diagram of the d^9 SO model does not exhibit any frustration or SO entanglement up to $\eta \simeq 0.07$ and the type of spin and orbital order are chosen there predominantly by the crystal field term $\propto E_z$. Quantum fluctuations dominate at $E_z \simeq 0$ and for $E_z < 0$, where they stabilize either in-plane or interplanar spin singlets accompanied by directional orbitals which stabilize them. Here the VBz phase extends down to large values of E_z, where instead the long-range order in the G-AFz phase was found in the 3D model. This demonstrates that interlayer quantum fluctuations are particularly strong in the present bilayer case. On the contrary, at $E_z > 0$

one finds the G-AF spin order which coexists with FO order of x orbitals. It is clear that both the VBz and G-AF phase are favored by the interplay of lattice geometry and by the shape of occupied orbitals for $E_z \to \pm\infty$. In this low-η regime of the diagram the area occupied by the PVB phase is narrow and especially orbital order is affected by the quantum critical fluctuations. The planar singlets are formed shortly after leaving the VBz phase and remain stable afterwards. Spin-orbital non-factorizability seems to be marginal in the entire VBz phase but plays certain role when switching to the planar singlet phase, especially visible for the interplane bond covariance R^c.

On the contrary, in the PVB phase away from the critical regime SO non-factorizability vanishes and suddenly reappears in the G-AF phase, not as a transition effect but rather as a robust feature vanishing only for high values of E_z. We argue that this is related with surprisingly rigid interplane spin-spin correlations which should, if we assume that SO correlations factorize, decay quickly as t^c approaches $1/2$. Following this factorized picture we could also expect stability of the C-AF phase for higher values of η, above the G-AF phase. These effects are absent in our results, showing that intuition suggesting SO factorization can be misleading even when considering such a simple isotropic orbital configuration.

For higher values of Hund's exchange η frustration increases when AF exchange interactions compete with FM ones, and as a result the most exotic phases with explicit on-site SO entanglement arise; two of them, the ESO and EPVB phase are neighboring and placed in between the VBz and PVB ones, and they become degenerate with both of them at the multicritical point where four phases meet (see Fig. 3.5). This situation follows from the fact that singlet phases are more susceptible to ferromagnetism favored by high η than the G-AF phase is, which turned out to be surprisingly robust. Further increase of η always leads to the A-AF phase throughout a discontinuous transition. Above $\eta \simeq 0.2$ the ESO phase is completely immersed in the A-AF one and ends up with a single bicritical point. If we come back below $\eta \approx 0.2$ then the ESO changes smoothly into the EPVB phase, being an entangled precursor of the PVB order, meaning that the non-uniform orbital order and in-plane singlets are formed and SO entanglement is removed as the orbitals are oriented along the singlet bond. On the other hand, this phase can be also seen as an extension of the A-AF into fully AF sector because the EPVB phase has long-range magnetic order, being however strongly non-uniform (see Fig. 3.9(a)).

The present $K_3Cu_2F_7$ bilayer system is somewhat similar to $La_{2-2x}Sr_{1+2x}Mn_2O_7$ bilayer manganites with very rich phase diagrams and competition between phases with different types of long-range order in doped systems [108, 109]. Such phases are generic in transition

metal oxides and were also reproduced in models of bilayer manganites which have to include in addition superexchange interaction between core t_{2g} spins [102, 103] that suppresses SO fluctuations and entanglement in the e_g subsystem. In contrast, $K_3Cu_2F_7$ bilayer is rather unique as the only electronic interactions arise here due to entangled SO superexchange. They explain the origin of the VBz phase observed [105] in $K_3Cu_2F_7$ but not found in bilayer manganites, and provide an experimental challenge of investigating whether signatures of SO entanglement could be identified in future experiments.

3.3 Two–dimensional Kugel–Khomskii model

The Kugel-Khomskii model for two dimensional lattice is given by the similar Hamiltonian as for the bilayer case 3.7,

$$\begin{aligned}\mathcal{H} &= -\frac{1}{2}J\sum_{\langle ij\rangle||\gamma}\left\{(r_1\,\Pi_t^{(ij)}+r_2\,\Pi_s^{(ij)})\left(\frac{1}{4}-\tau_i^\gamma\tau_j^\gamma\right)+(r_2+r_4)\,\Pi_s^{(ij)}\left(\frac{1}{2}-\tau_i^\gamma\right)\left(\frac{1}{2}-\tau_j^\gamma\right)\right\}\\ &- E_z\sum_i\tau_i^c,\end{aligned} \tag{3.39}$$

but here the sums go over the bonds $\langle i,j\rangle$ of a square lattice and $\gamma=a,b$. This model is designed for K_2CuF_4, if we neglect the Jahn-Teller distortions, and can explain the pressure induced phase transition from AO FM phase to FO AFx phase [110], as we will show using MF methods. In the following sections we will present: the single-site phase diagram of the model including basic AF and FM magnetic configuration in Sec. 3.3.1 and cluster MF approach in Sec. 3.3.2. Then, in Sec. 3.3.3 will show the cluster MF phase diagrams with more exotic valence-bond and double-AF states and their thermal evolution for chosen temperatures. The thermal decay of the double-AF phase will be discussed in more details in Sec. 3.3.4. Finally, we will explain double-AF spin order in terms of an effective spin-only perturbative Hamiltonian in Sec. 3.3.5, derived in the similar way as the $t-J$ model is derived out of 2D Hubbard model [111]. Final conclusions and summary will be given in Sec. 3.3.6.

3.3.1 Single-site mean field

Using the same reasoning and formulas as in Section 3.2.1 we can easily obtain single-site MF phase diagram for a 2D model. The starting point is the effective orbital Hamiltonian obtained from the 2D KK model,

$$\mathcal{H}_{\mathrm{MF}} = \frac{1}{2}J\sum_{i,\gamma}\left\{\tau_i^\gamma\tau_{i+\gamma}^\gamma(\chi^\gamma-\xi^\gamma)+\tau_i^\gamma\xi^\gamma-\frac{1}{4}(\chi^\gamma+\xi^\gamma)\right\}-E_z\sum_i\tau_i^c, \tag{3.40}$$

where sums go over the sites of a square lattice, $\gamma = a, b$ and $i+\gamma$ is the nearest neighbor of site i in the direction γ. The quantities:

$$\begin{aligned}\chi^\gamma &= r_1\Pi_t^\gamma + r_2\Pi_s^\gamma,\\ \xi^\gamma &= (r_2+r_4)\Pi_s^\gamma,\end{aligned} \tag{3.41}$$

are the parameters obtained by averaging over spin operators with assumption that the spin order, determining χ^γ and ξ^γ, depends only on the direction γ and not on site i. It is sufficient to investigate the phases with either G-AF or FM long-range order and these are the only two types of broken symmetry states we will take into account. Following Table 3.1 we put $\Pi_t^\gamma = 1$ and $\Pi_s^\gamma = 0$ in FM phase and $\Pi_t^\gamma = \Pi_s^\gamma = 1/2$ in G-AF phase. The MF decoupling and solution of self-consistency equation is given in Sec. 3.2.1 can be easily adopted to the single-layer system.

The resulting phase diagram is shown in Fig. 3.12. The diagram is similar to the one obtained for the bilayer system (see Fig. 3.2) but the number of phases is here smaller due to the simpler geometry of the lattice (no C-AF or A-AF configuration possible). As before, we can distinguish between two classes of solutions of self-consistency equations: (*i*) AO solutions (green area) and (*ii*) FO solutions with fully polarized orbitals being either x or z (white area). The FO phases are either AF or FM in negative E_z sector (G-AFz and FMz phases) while for positive E_z we have found that only the G-AFx configuration is stable. The AO part of the diagram lies between x and z phases and is dominated by ferromagnetism (FM phase). The antiferromagnetism with AO order is limited to a narrow area in the crossover regime between G-AFx and FM phases, only for sufficiently small Hund's rule coupling ($\eta \lesssim 0.2$). The multicritical point is located at $E_z = -0.5J$ and $\eta = 0$ meaning that the area of the G-AFz phase for small η shrinks here with respect to the one found for a bilayer. This can be understood in such a way: z orbitals are elongated in the c direction and

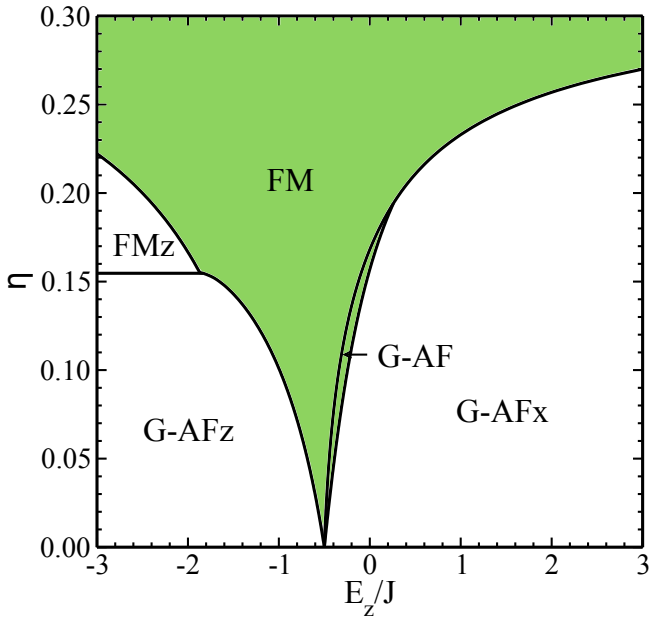

Figure 3.12: Phase diagram of the 2D KK model obtained in the single-site MF approximation. Shaded green area indicates phases with AO order while the remaining phases are accompanied by FO order with fully polarized x or z orbitals.

favor strong antiferromagnetism in this direction— increasing number of ab planes makes the G-AF configuration more stable. This is confirmed in case of a fully 3D system studied in Sec. 3.4.

3.3.2 Cluster mean field at zero and finite temperature

Following the ideas from Secs. 3.2.2 and 3.2.3, to obtain more general approximation than a single-site mean field and finite-temperature description of the system, we divide the lattice into square clusters showed in the Fig. 3.13. The bonds corresponding to the solid lines in the figure are left unchanged with respect to the KK Hamiltonian (3.39) while the bonds depicted with dashed lines are decoupled using the approximate identity:

$$O_i O_j \approx O_i\langle O_j\rangle_T - \frac{1}{2}\langle O_i\rangle_T\langle O_j\rangle_T + O_j\langle O_i\rangle_T - \frac{1}{2}\langle O_i\rangle_T\langle O_j\rangle_T, \tag{3.42}$$

with $\langle\dots\rangle_T$ being a thermal average in a canonical ensemble with Boltzmann constant fixed as $k_B = 1$. Now we assume that site i belongs to our chosen cluster (Fig. 3.13) and j belongs to

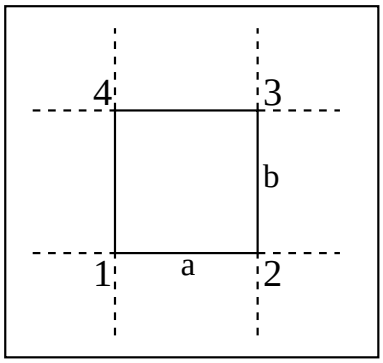

Figure 3.13: Schematic view of the square cluster (plaquette) used in the cluster MF approach to the 2D KK model. Vertices $i = 1, 2, 3, 4$ and directions $\gamma = a, b$ are marked in the figure, and dashed lines stand for the outgoing MF interactions in the a and b direction.

a neighboring one and the bond is splitted into two halves– first is added to the Hamiltonian of cluster i and the other to j. In this way an original KK Hamiltonian transforms into the sum of commuting cluster Hamiltonians interacting via mean fields. The mean fields follow from Eq. (3.42) applied to all the two-site operator products encountered in the Hamiltonian (3.39) and are defined as:

$$s_i^\alpha \equiv \langle S_i^\alpha \rangle_T \quad , \qquad t_i^\gamma \equiv \langle \tau_i^\gamma \rangle_T \, , \qquad v_i^{\alpha,\gamma} \equiv \langle S_i^\alpha \tau_i^\gamma \rangle_T \, , \tag{3.43}$$

with $\alpha = x, z$, $\gamma = a, b$ and $i = 1, 2, 3, 4$. Note that, in contrast to the bilayer case, we do not assume that the SU(2) symmetry of the spin sector can be broken only in the z spin direction ($\alpha = z$) but we also allow $\alpha = x$ to capture more exotic types of magnetic order suggested by the perturbative expansions from Sec. 3.3.5. We do not consider $\alpha = y$ as the two spin components are sufficient to capture all interesting features and we prefer to keep the cluster Hamiltonian strictly real. Unlike in the bilayer case we do not assume anything about the order *inside* the cluster because the considered plaquette is small enough to keep all the order parameters as independent from one another and as the quantities to be determined. Nevertheless, we still have to relate *different* clusters to make the problem solvable. The simplest solution is to assume that all the clusters are in the same state and the values of order parameters do not vary from cluster to cluster. More general solution is to allow the neighboring clusters to be rotated by $\pi/2$ with respect to each other. This means orbital order parameters can alternate from cluster to cluster and produce e.g. PVB configuration.

The self–consistency equations still cannot be solved exactly because the effective cluster Hilbert space is of the size $d = 2^8$ which is too large for analytical methods. The way out is to use Bethe–Peierls–Weiss method, i.e., set certain initial values for the order parameters $\{s_i^\alpha, t_i^\gamma, v_i^{\alpha,\gamma}\}$ and next employ numerical diagonalization algorithm to diagonalize the cluster Hamiltonian. Then we recalculate $\{s_i^\alpha, t_i^\gamma, v_i^{\alpha,\gamma}\}$ according to their definitions given by Eqs. (3.43) using, in general, the partition function known from the diagonalization and all the eigenstates. The procedure is repeated until the convergence conditions for energy and order parameters are satisfied.

3.3.3 Zero- and finite-temperature phase diagrams

Phase diagrams can be determined by finding the configurations with lowest free energies for given temperature T and parameters E_z and η being the solutions of the self-consistency equations, which means that they reached the demanded convergence condition. To include all possible configurations we first initiate the MF iterations by random values of order parameters $\{s_i^\alpha, t_i^\gamma, v_i^{\alpha,\gamma}\}$. After determining which phases appear in the phase diagram the phase boundaries are calculated by comparing the energies starting from typical values of order parameters $\{s_i^\alpha, t_i^\gamma, v_i^{\alpha,\gamma}\}$ in considered phases.

In Fig. 3.14(a) we showed the zero-temperature phase diagram of the 2D KK model. The diagram includes two G-AF phases with FO order for negative and positive values of E_z. In contrast to the single-site approach, the orbitals are not fully polarized but the dominant orbital component is still z for $E_z < 0$ and x for $E_z > 0$. Similarly to the bilayer phase diagram (Fig. 3.5), the right G-AF phase borders with a PVB phase from the left-hand side (yellow area) and with FM phase from the top. The left G-AF phase was absent in the bilayer case because the lattice geometry favored interlayer singlets which is not the case for a single layer. Away from the central part of the diagram, dominated by the PVB configuration, the left G-AF phase exhibits interesting instability at the AF-FM transition; a new, intermediate phase appears called double-AF phase (orange area). This new state is characterized by an exotic magnetic order shown in Fig. 3.15, with neighboring spins being perpendicular and next nearest neighbors being AF, coexisting with a simple FO order. it will be shown later on (see Sec. 3.3.5), this strange behavior can be understood in terms of a perturbation expansion around the fully polarized FO configuration by deriving an effective spin-only model. Returning to our diagram, we can see the two FM phases differing by the orbital configuration; the pure FM phase is accompanied by AO order and the other one

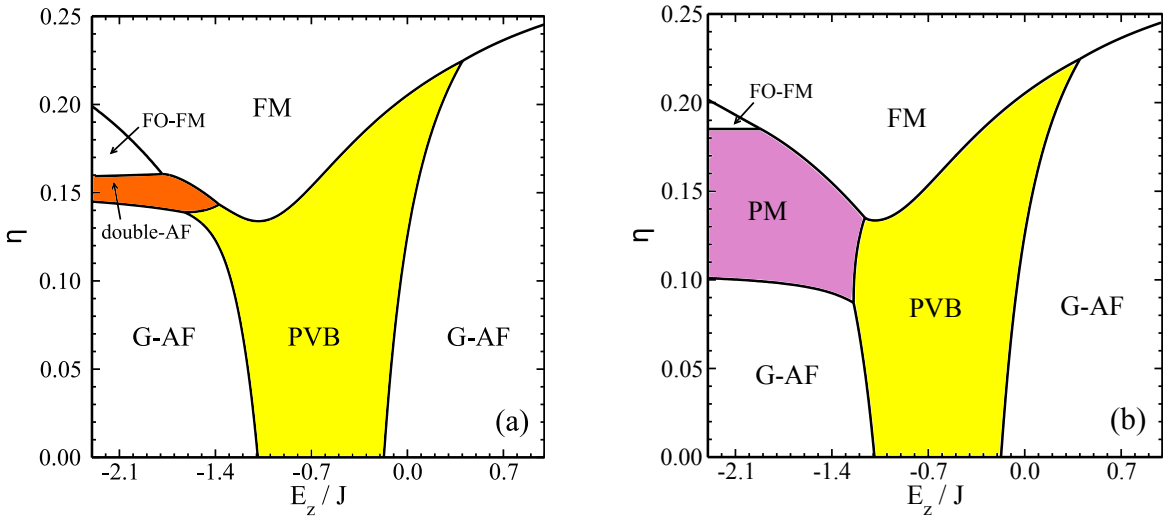

Figure 3.14: Phase diagrams of the 2D KK model in the cluster MF approximation, obtained at: (a) $T = 0$ and (b) $T = 0.05J$. In between the G-AF and FM phases on finds: plaquette valence-bond phase (PVB) with alternating spin singlets (shaded in yellow), and entangled, double-AF phase (orange). At temperature $T = 0.05J$ a new, FO paramagnetic phase appears– PM (violet area) replacing double-AF order. For high-temperature diagrams see Fig. 3.16.

has FO order. The transition between these two orders is smooth in contrast to all other transitions found at $T = 0$, including transitions to double-AF phase. The presence of FO order in the negative-E_z part of the phase diagram is a new effect comparing to the bilayer case, where this parameter region was dominated by the A-AF phase.

The low-temperature phase diagram is showed in Fig. 3.14(b). At the temperature $T = 0.05J$ the double-AF phase is already destroyed and replaced by a paramagnetic phase (PM, violet area) with no long-range spin order and FO order induced by the crystal field E_z. Also the upper part of the left G-AF phase and the bottom part of the FM phase in the negative-E_z region get unstable and are replaced by the PM phase. The positive-E_z part of the phase diagram and the major part of the PVB phase are not influenced by weak thermal fluctuations. The high fragility of the PM area under the thermal fluctuations can be understood by realizing the two facts: (i) the strong z orbital component present for $E_z < 0$ is not compatible with the planar geometry of the lattice (see Figs. 3.1(a) and 3.1(c))– the orbitals point out of the plane and (ii) the Heisenberg interactions between the spins are weak due to the sing change at the AF-FM transition. All transitions from AF or FM phases to a paramagnet are smooth.

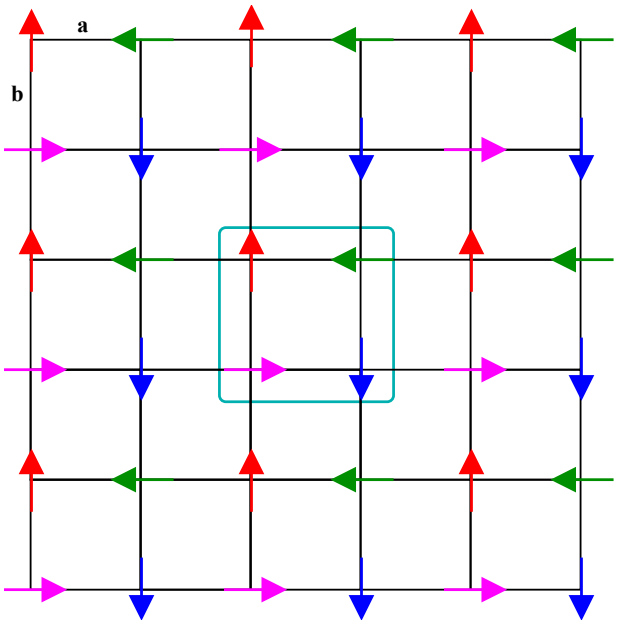

Figure 3.15: Artist's view of the double-AF spin order realized by the 2D KK model. Four colors of the arrows correspond to four spin sublattices. Up (down) arrows stand for $\langle S_i^z \rangle = \pm 1/2$, right (left) arrows stand for $\langle S_i^x \rangle = \pm 1/2$. The embedded cluster is marked with a blue frame.

In Figs. 3.16(a) and 3.16(b) we show high-temperature phase diagrams for $T = 0.2J$ and $T = 0.34J$ respectively. Already for the lower temperature $T = 0.2J$ the left G-AF phase is completely melted to the paramagnet together with the FO-FM phase. The lowest part of the FM phase loses magnetization and becomes paramagnetic with alternating orbitals (blue area). The PVB phase shrinks slightly from the left but the right part of the phase diagram is still intact. At higher temperature $T = 0.34J$ the PVB phase no longer exists for $\eta = 0$ and melts to the PM phase from the left and to G-AF one from the right which is somewhat peculiar meaning that thermal fluctuation destroy alternating pairs of singlets and restore global AF magnetization. On the other hand, the orbital order is lowered to the FO one stabilized by the crystal field E_z so we can argue that overall spin and orbital order is lowered by the thermal fluctuations. In the FM region the AO-PM phase expands to the positive-E_z part of the diagram replacing the FM phase and gets melted itself from the bottom becoming FO. One can expect that for higher temperatures the PVB phase will disappear completely and the right G-AF will finally melt down to a paramagnet. The AO-PM and FM phases will be present in any temperature because they are favored by r_1

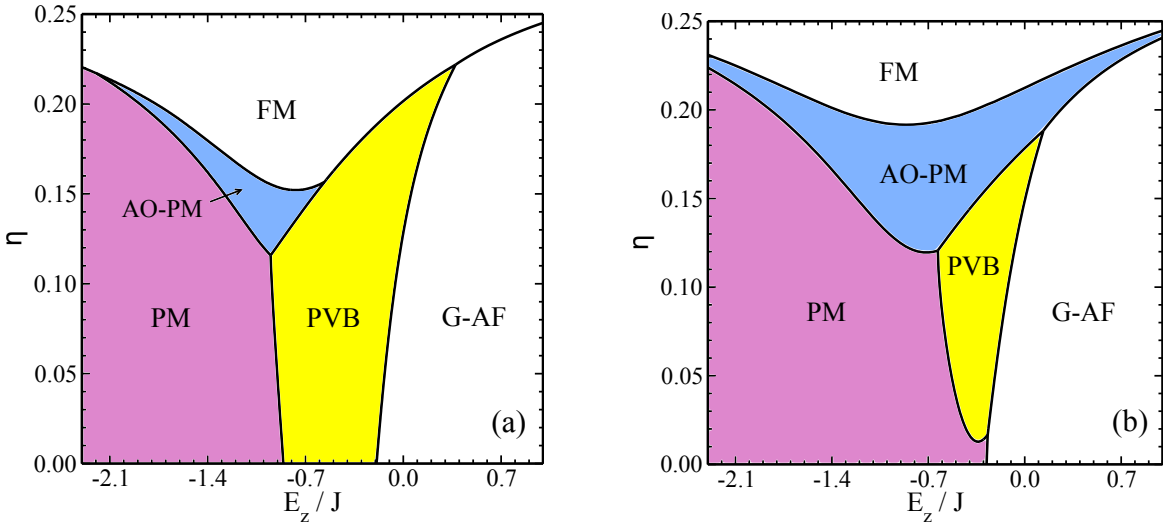

Figure 3.16: Phase diagrams of the 2D KK model in the cluster MF approximation at finite temperature: (a) $T = 0.2J$, and (b) $T = 0.34J$. PM phase (pink area) completely suppresses G-AF phase in the negative–E_z region, part of the FM phase becomes paramagnetic but preserves orbital alternation (blue area).

coefficient which can be arbitrary large but we should keep in mind that physical values of η never exceed $\eta = 0.25$.

3.3.4 Thermal decay of the double-AF phase

As we can see in Figs. 3.14(a) and 3.14(b) the double-AF phase melts down to a paramagnet in relatively low temperature. This not surprising because, as we will show in the next subsection, the exotic spin order in double-AF phase is stabilized by interactions of the second and third order in the perturbative expansion, around fully polarized FOz configuration, with energy scales being lower than in case of standard magnetic ordering. Therefore it is interesting to look more carefully at the thermal evolution of spin, orbital and SO order in the double-AF phase.

In Fig.3.17 (a) we can see the spin $s^{x,z} \equiv s_1^{x,z}$ and orbital $t^{a,b} \equiv t_1^{a,b}$ order parameters in the double-AF ($E_z = -2J$, $\eta = 0.15$) phase as functions of temperature together with total AF magnetization defined as $s \equiv \sqrt{(s^x)^2 + (s^z)^2}$. Due to the symmetry of the phase shown in Fig. 3.15 it is sufficient to look at order parameters at a chosen site i, here $i = 1$. As we can see, the orbital order in the double-AF phase is FO, due to large negative crystal field E_z, and as such is very resistant to thermal fluctuations. Thus $t^{a,b}(T)$ behaves as a constant

function. This is not the case for the magnetic order; the $s^{x,z}$ curves tend smoothly to zero at the transition to the PM phase whereas for $T = 0$ the total AF magnetization s stays close to the classical value of $s = 0.5$. Due to the symmetry of the rotation around the y axis in the spin space the proportion between s^x and s^z is not fixed and in this case they originate from the random configuration chosen as a starting point at $T = 0$. In contrast to that, the total s is unambiguously determined by the minimum of the free energy.

To quantify the effects of SO entanglement in the double-AF phase we define the on-site r_α^γ an bond R^γ SO covariances in analogy with the bilayer system considered in Sec. 3.2.8:

$$r_\alpha^\gamma = v_1^{\alpha,\gamma} - s_1^\alpha t_1^\gamma, \qquad R^\gamma = \left\langle (\mathbf{S}_1 \cdot \mathbf{S}_{1+\gamma}) \tau_1^\gamma \tau_{1+\gamma}^\gamma \right\rangle - \left\langle \mathbf{S}_1 \cdot \mathbf{S}_{1+\gamma} \right\rangle \left\langle \tau_1^\gamma \tau_{1+\gamma}^\gamma \right\rangle . \tag{3.44}$$

At $T = 0$ such quantities show how the spin and orbital degrees of freedom mix in the wave function of the cluster but it should not be treated as a rigorous measure of entanglement, such as for example von Neumann entropy defined in the Sec. 2.2.2. For $T > 0$ it is not clear how much of the SO mixing is thermal and how much is quantum so we cannot talk about the entanglement anymore. In Fig. 3.17(b) we can see the thermal evolution of r_α^γ and R^γin the double-AF and PM phases in the same parameter range as before. The behavior of the on-site covariances r_α^γ is similar to the behavior of magnetic order parameters and the non-zero values at $T = 0$ indicate SO entangled ground-state. Surprisingly, despite the FO configuration of the double-AF phase the r_α^γ functions depend on γ in a non-trivial way. This requires an explanations; it turns out that the SO order exhibits an alternating nature of the AO order, i.e.:

$$v_1^{\alpha,\gamma} = -v_3^{\alpha,\gamma}, \qquad v_2^{\alpha,\gamma} = -v_4^{\alpha,\gamma}, \tag{3.45}$$

but:

$$v_2^{z,a} = -v_1^{x,b}, \qquad v_2^{z,b} = -v_1^{x,a}, \tag{3.46}$$

$$v_2^{x,a} = v_1^{z,b}, \qquad v_2^{x,b} = v_1^{z,a}. \tag{3.47}$$

This means that we need to know four SO mean fields to determine the SO order that gives four different SO covariances r_α^γ. The bond SO covariances R^γ behave in a simpler way; as we could expect the dependence on γ is trivial. R^γ take non-zero values in whole range of temperature with intriguing zero-point before the transition line. The reason for this sign

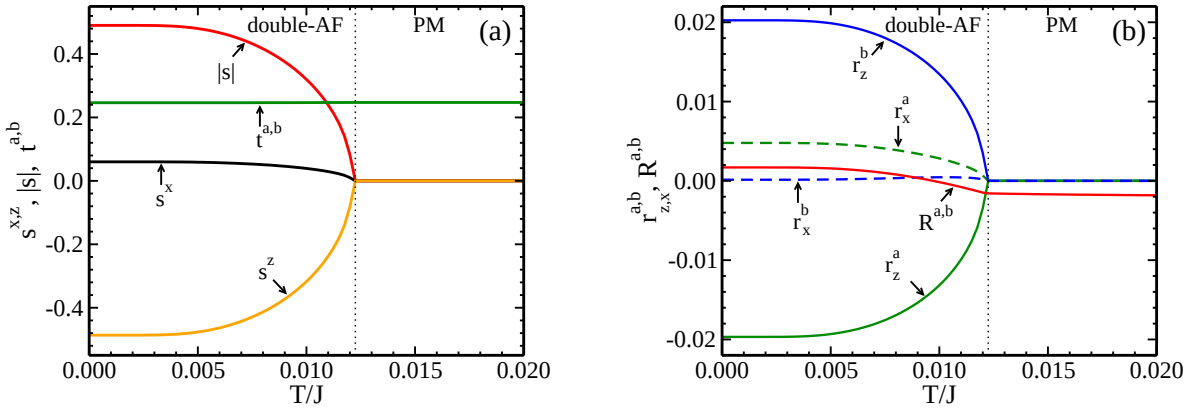

Figure 3.17: Thermal evolution of the order parameters and SO covariances in the double-AF and PM phase for $0 < T < 0.02J$ and $E_z = -2J$, $\eta = 0.15$: (a) order parameters– orbital $t^{a,b}$ (green line) and spin $s^{x,z}$ (orange and black lines) mean fields and total AF magnetization s (red line); (b) covariances– on-site r^{γ}_{α} (green and blue lines) and bond R^{γ} (red line) SO covariances for $\gamma = a, b$ and $\alpha = x, z$.

change is unknown; our hypothesis is that this is quantum covariance from the low-T region that changes into the thermal one remaining in the PM phase.

The spin and orbital NN correlation functions not showed here behave in a very predictable way; the spin correlations are close to zero at $T = 0$ and above, which agrees with Fig. 3.15 and analytical considerations in the following subsection, and the orbital ones stay close to $(t^a)^2$.

3.3.5 Effective spin model in the double-AF phase

To explain the exotic magnetic order found in the double-AF phase and shown in Fig. 3.15 we will derive an effective spin model for this phase. The idea is to use the standard quantum perturbation theory with degeneracy for the orbital sector of the KK model. We can divide the Hamiltonian given by Eq. (3.39) into the unperturbed part H_0 and perturbation V in the following way:

$$H_0 = -E_z \sum_i \tau_i^c, \tag{3.48}$$

$$V = -\frac{1}{2}\sum_{\langle ij\rangle||\gamma}\left\{(r_1\,\Pi_t^{(ij)} + r_2\,\Pi_s^{(ij)})\left(\frac{1}{4} - \tau_i^{\gamma}\tau_j^{\gamma}\right) + (r_2 + r_4)\,\Pi_s^{(ij)}\left(\frac{1}{2} - \tau_i^{\gamma}\right)\left(\frac{1}{2} - \tau_j^{\gamma}\right)\right\}, \tag{3.49}$$

where for simplicity we put $J = 1$. This can serve as a starting point for the perturbative treatment for large $|E_z| > J$. For negative E_z (from now on in units of J) the ground state $|0\rangle$ of H_0 is the state with all orbitals being the z orbitals, i.e.,

$$\forall i: \quad \tau_i^c |0\rangle = -\frac{1}{2} |0\rangle , \tag{3.50}$$

with energy $E_0 = \frac{1}{2} E_z L^2$ (where L is the linear size of the system). Following the quantum perturbation theory we can construct the effective spin Hamiltonian H_s using the expansion in powers of E_z^{-1}:

$$H_s = E_0 + \langle 0| V |0\rangle + \sum_{n \neq 0} \frac{1}{E_n - E_0} \langle n| V |0\rangle^2 + O\left(E_z^{-2}\right), \tag{3.51}$$

where all the overlaps are taken between the orbital states leaving the spin operators alone. Knowing the definition of the orbital operators τ_i^γ:

$$\tau_i^{a,b} \equiv \frac{1}{4}(-\sigma_i^z \pm \sqrt{3}\sigma_i^x), \quad \tau_i^c \equiv \frac{1}{2}\sigma_i^z. \tag{3.52}$$

we can easily calculate the desired orbital overlaps. Zero and first order give:

$$H_s^{(0)} + H_s^{(1)} = \frac{1}{2} E_z L^2 + \sum_i \sum_{\gamma=a,b} \frac{1}{2} \left\{ (\mathbf{S}_i \cdot \mathbf{S}_{i+\gamma}) \frac{-3r_1 + 4r_2 + r_4}{16} - \frac{9r_1 + 4r_2 + r_4}{64} \right\}. \tag{3.53}$$

In the second order the sum runs over all excited orbital states but looking at Eqs. (3.49) and (3.52) one can see that V has non-zero overlap only with states with one orbital excited or with two orbitals excited being nearest neighbors. This brings us to the second order correction of the form:

$$\begin{aligned} H_s^{(2)} &= \frac{1}{E_z} \frac{3}{2^{10}} \sum_{i_0} \left\{ \sum_{\substack{\gamma=\pm a, \\ \pm b}} s_\gamma \left(\mathbf{S}_{i_0} \cdot \mathbf{S}_{i_0+\gamma}\right) \left(r_1 + 2r_2 + 3r_4\right) \right\}^2 \\ &+ \frac{1}{2E_z} \frac{9}{2^{10}} \sum_{i_0} \sum_{\gamma=a,b} \left\{ \left(\mathbf{S}_{i_0} \cdot \mathbf{S}_{i_0+\gamma}\right) \left(r_1 + r_4\right) + \frac{3r_1 - r_4}{4} \right\}^2, \end{aligned} \tag{3.54}$$

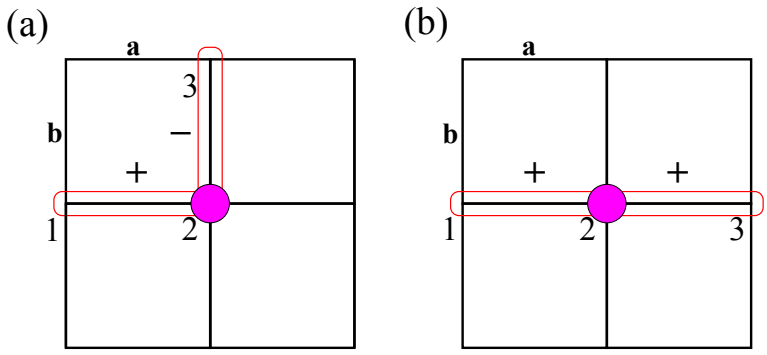

Figure 3.18: Schematic views of second order corrections in effective spin Hamiltonian: (a) effective second-NN interactions; (b) effective third-NN interaction. Red frames stand for Heisenberg bond with ± sign depending on the bond's direction and magenta dots are the single-site orbital excitations in the ground state.

where s_γ is a sign factor depending on bond's direction γ originating from the definition of operators $\tau_i^{a,b}$, i.e.,

$$s_\gamma = \left\{ \begin{array}{ccc} 1 & if & \gamma = \pm a \\ -1 & if & \gamma = \pm b \end{array} \right\}. \tag{3.55}$$

Second powers in $H_s^{(2)}$ produce spin products of the two forms which can be simplified using elementary algebra:

$$\left(\mathbf{S}_{i_0+\gamma} \cdot \mathbf{S}_{i_0}\right)\left(\mathbf{S}_{i_0} \cdot \mathbf{S}_{i_0+\gamma'}\right) = \frac{1}{4}\left(\mathbf{S}_{i_0+\gamma} \cdot \mathbf{S}_{i_0+\gamma'}\right) + i\frac{1}{2}\mathbf{S}_{i_0+\gamma} \cdot \left(\mathbf{S}_{i_0} \times \mathbf{S}_{i_0+\gamma'}\right), \tag{3.56}$$

$$\left(\mathbf{S}_{i_0} \cdot \mathbf{S}_{i_0+\gamma}\right)^2 = -\frac{1}{2}\left(\mathbf{S}_{i_0} \cdot \mathbf{S}_{i_0+\gamma}\right) + \frac{3}{16}. \tag{3.57}$$

The second identity together with linear terms in $\mathbf{S}_{i_0} \cdot \mathbf{S}_{i_0+\gamma}$ give E_z^{-1} correction to the Heisenberg interactions in $H_s^{(1)}$ while the first one leads to new type of physics. At the AF-FM phase transition the NN Heisenberg interactions change sing meaning that the first order Hamiltonian $H_s^{(1)}$can be arbitrarily small; then the second order effects governed by Eqs. (3.54) and (3.56) become important. Looking at Eq. (3.56) we can see that the imaginary term is antihermitian and must cancel out with other terms in $H_s^{(2)}$. Thus, in $H_s^{(2)}$, we are left with pure Heisenberg term $\mathbf{S}_{i_0+\gamma} \cdot \mathbf{S}_{i_0+\gamma'}$ connecting sites $i_0+\gamma$ and $i_0+\gamma'$, being either second or third nearest neighbors, presented in Fig. 3.18(a) and 3.18(b), with sign given by

$s_\gamma s_{\gamma'}$. Finally, the effective spin Hamiltonian up to second order can be written as:

$$\begin{aligned} H_s &= \sum_{\langle i,j\rangle} (\mathbf{S}_i \cdot \mathbf{S}_j) \left\{ \frac{-3r_1 + 4r_2 + r_4}{32} + O\left(E_z^{-1}\right) \right\} - \frac{1}{E_z} \frac{3}{2^{10}} \sum_{\langle\langle i,j\rangle\rangle} (\mathbf{S}_i \cdot \mathbf{S}_j) \left(r_1 + 2r_2 + 3r_4\right)^2 \\ &+ \frac{1}{E_z} \frac{3}{2^{11}} \sum_{\langle\langle\langle i,j\rangle\rangle\rangle} (\mathbf{S}_i \cdot \mathbf{S}_j) \left(r_1 + 2r_2 + 3r_4\right)^2 + O\left(E_z^{-2}\right), \end{aligned} \tag{3.58}$$

with $\langle\langle i,j\rangle\rangle$ and $\langle\langle\langle i,j\rangle\rangle\rangle$ denoting second and third nearest neighbors i and j. In the limit of $E_z \to -\infty$ the NN interactions vanish at $\eta = \eta_0 \approx 0.1547$ and we are left with next-NN (NNN) AF interactions and twice weaker third-NN FM interactions. The origin of this factor 2 lies in the double counting of the NNN interactions. One can easily guess that the ground state of such Hamiltonian consists of two, weakly fluctuating antiferromagnets on two interpenetrating sublattices of the square lattice and the angle φ between them is undetermined, as shown in Fig. 3.19(a). Such ground state is similar to the double-AF phase (Fig. 3.15) and η_0 nicely falls into the area of double-AF in the phase diagram of Fig. 3.13(a) but we still have to find the reason why the two aniferromagnets prefer to be perpendicular. To answer this question we have to go to the third order of perturbation expansion given by the formula:

$$H_s^{(3)} = \sum_{n\neq 0} \sum_{m\neq 0} \frac{1}{E_n - E_0} \frac{1}{E_m - E_0} \langle 0| V |n\rangle \langle n| V |m\rangle \langle m| V |0\rangle . \tag{3.59}$$

This produces many contributions to the spin Hamiltonian but we are interested only in terms with new structure comparing to the lower orders because the other will be the E_z^{-2} corrections to the interactions we already have. The terms bringing potentially new physics are the ones with three different Heisenberg bonds multiplied one after another. Such contribution is depicted in Fig. 3.19(b) for sites $i = 1, 2, 3, 4$ and can be transformed as:

$$\begin{aligned} (\mathbf{S}_1 \cdot \mathbf{S}_2)(\mathbf{S}_2 \cdot \mathbf{S}_3)(\mathbf{S}_3 \cdot \mathbf{S}_4) &= \frac{1}{16} \mathbf{S}_1 \cdot \mathbf{S}_4 + \frac{1}{4} (\mathbf{S}_1 \cdot \mathbf{S}_4)(\mathbf{S}_2 \cdot \mathbf{S}_3) - \frac{1}{4} (\mathbf{S}_1 \cdot \mathbf{S}_3)(\mathbf{S}_2 \cdot \mathbf{S}_4) \\ &+ i\frac{1}{8} \mathbf{S}_1 \cdot (\mathbf{S}_3 \times \mathbf{S}_4) + i\frac{1}{8} \mathbf{S}_1 \cdot (\mathbf{S}_4 \times \mathbf{S}_2), \end{aligned} \tag{3.60}$$

where imaginary terms are antihermitian and must cancel out with other terms of the same

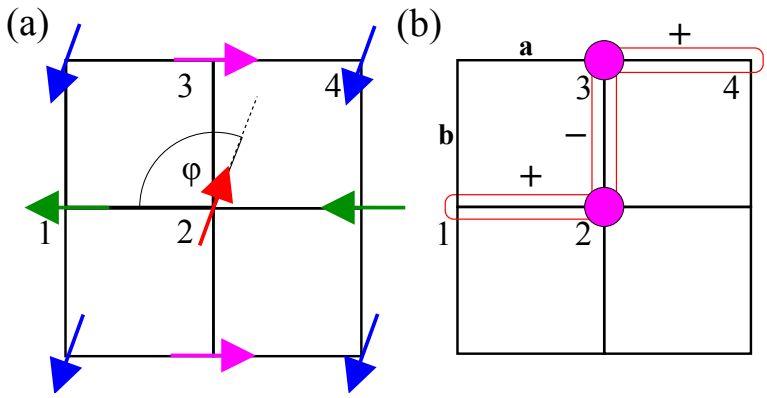

Figure 3.19: Panel (a): two independent AF orders realized by effective spin Hamiltonian H_s up to second order. Angle φ between the two neighboring spins is undetermined. Panel (b): exemplary third order correction to H_s fixing the angle φ as $\varphi = \pi/2$. Red frames stand for Heisenberg bond with $\pm$ sign depending on the bond's direction and magenta dots indicate the single-site orbital excitations in the ground state.

structure in $H_s^{(3)}$. To analyze the other terms in Eq. (3.60) we have to use the fact that order on sublattices is almost classical AF: (*i*) first terms is an AF interaction between the sublattices which is *not* compatible with antiferromagnetism on sublattices being of the order of E_z stronger, (*ii*) second term favors perpendicularity of the two AF sublattices which is compatible with the order on sublattices, and (*iii*) third term brings no new information about the order. Taking into account all three arguments we argue that third order perturbative contributions of form given by Eq. (3.60) favor perpendicularity of the two AF orders. Now we have to extract all such contributions from Eq. (3.59) and check if the total sign is indeed positive because otherwise our arguments would be incomplete. After long but elementary calculation we obtain the total sublattice-interaction Hamiltonian as:

$$H_{int}^{(3)} = \frac{3^3}{2^{17}E_z^2}\left(r_1+r_4\right)\left(r_1+2r_2+3r_4\right)^2 \sum_{i_0}\sum_{\gamma=a,b}\left(\mathbf{S}_{i_0}\cdot\mathbf{S}_{i_0+\gamma}\right)\sum_{\substack{\gamma'\neq\gamma\\ \gamma''\neq-\gamma}} s_{\gamma'}s_{\gamma''}\left(\mathbf{S}_{i_0+\gamma'}\cdot\mathbf{S}_{i_0+\gamma+\gamma''}\right), \tag{3.61}$$

which in classical limit takes the following form:

$$H_{int}^{(3)} \approx \frac{3^5}{2^{17}E_z^2}\left(r_1+r_4\right)\left(r_1+2r_2+3r_4\right)^2 \sum_{i_0}\frac{1}{16}\cos^2\varphi. \tag{3.62}$$

We easily find φ minimizing energy at $\varphi = \pi/2$. This finally explains the exotic magnetic

order encountered in the double-AF phase as a third order perturbative effect of orbital fluctuations. We have checked by the cluster MF method that the tendency towards two perpendicular AF orders is strongly suppressed for extremely low E_z and then the algorithm can converge for any random value of φ, but still the AF order on sublattices is rigid. These observations are consistent with the analytical results presented above.

3.3.6 Summary and conclusions

Summarizing, we have constructed the cluster MF approximation for the 2D KK model and obtained a phase diagram with AF and FM long range orders together with a valence-bond phase and exotic double-AF phase. The last one is a consequence of AF-FM transition, where the NN Heisenberg interactions, from the first order of the perturbation expansion around the FO configuration, change sign passing through zero. It was proved that at this point the second and third NN Heisenberg interactions become important and the lattice splits into two sublattices which do not interact up to the third order of perturbative expansion. Then, in the third order, the effective interactions lose their Heisenberg character and become more classical favoring the perpendicular orientation of the two sublattices. This perturbative reasoning involving relatively high orders of the orbital fluctuations confirms the fact that double-AF phase is stabilized by the SO entanglement which manifests itself in high values of the on-site SO covariances. Thus, the double-AF phase cannot be observed in the approach assuming factorizable spin and orbital mean fields, as the single-site MF approximation. We also argue that the double-AF phase can be observed in the positive E_z region, connecting right G-AF phase with the FM one, because the same expansion as performed for FOz configuration can be performed for the FOx one. The only difference is that it will be stable for much higher values of η, close to $\eta = 0.29$, and thus for much higher E_z than shown in the phase diagram of Fig. 3.14(a).

We note that the phase transition from the FM to the right G-AF phase, present in the cluster MF phase diagram above $\eta \simeq 0.22$, for increasing E_z, agrees qualitatively with the pressure induced phase transition observed in K_2CuF_4 [110]. Also the fact that the FM phase is accompanied by the AO order and AF phase by the FO one stays in agreement with experiments done for K_2CuF_4 and with Goodenough-Kanamori rules [3].

The overall thermal evolution of the phase diagram shows that this new type of magnetic order is very subtle and susceptible to thermal fluctuations and melts down directly to a paramagnet at very low $T \simeq 0.012J$. Such high susceptibility is also a feature of the G-AF

with FOz order where spin interactions in the plane are weak due to the small overlap of the z orbitals. The FM and PVB phases are more resistant to heat and both high-η PVB and FM first melt to an AO paramagnet and only at higher temperature to an ordinary PM. This is because the orbital order is more like a classical Ising order here, which is an exact statement for the QCM, as explained in [49], being essentially an orbital model with maximally frustrated interactions [51]. As a matter of fact, in a pure 2D system no magnetic order should be present above $T = 0$ as it was proved in the famous paper by Mermin and Wagner [112]. Nevertheless, the Mermin-Wagner theorem concerns the spontaneous breaking of continuous symmetries and does not apply to the orbital model or to orbital interactions in a spin-orbital model. Moreover, considering magnetic ordering of K_2CuF_4 makes sense because this compound consists of weakly interacting planes and can be regarded as a 2D system but still some weak interplane interactions are present and can stabilize magnetic order.

We argue that the cluster MF method presented in this section is more general that the one used for the bilayer system, as it involves more components of spin, and thus reveals more of the essential physics of the model in 2D. This statement is confirmed by the perturbative expansion in the double-AF phase showing that additional spin component is necessary to describe exotic magnetic order. Therefore we will use this generalized MF method to study the KK model on a 3D cubic lattice in the following section.

3.4 Three-dimensional Kugel–Khomskii model

The major part of the introduction and motivation for the 3D KK model was given at the beginning of this chapter. The Hamiltonian we would like to focus on has the same form as before:

$$\begin{aligned} \mathcal{H} &= -\frac{1}{2}J \sum_{\langle ij \rangle || \gamma} \left\{ (r_1\, \Pi_t^{(ij)} + r_2\, \Pi_s^{(ij)}) \left(\frac{1}{4} - \tau_i^\gamma \tau_j^\gamma \right) + (r_2 + r_4)\, \Pi_s^{(ij)} \left(\frac{1}{2} - \tau_i^\gamma \right) \left(\frac{1}{2} - \tau_j^\gamma \right) \right\} \\ &- E_z \sum_i \tau_i^c, \end{aligned} \tag{3.63}$$

with $\gamma = a, b, c$ and sums taken over all bonds and sites of the 3D cubic lattice. The section is organized in a similar way as before: in Sec. 3.4.1 we present a single-site MF phase diagram of the model containing the same configuration as in the bilayer case, then in Sec. 3.4.2 we

introduce cluster MF method for the 3D system with two different topologies of cluster and show the resulting phase diagram. The diagram contains three phases with exotic magnetic order: the already known double-AF phase being AF in the c direction, canted-A-AF phase– the 1D version of the latter one and striped-AF phase with anisotropic AF order in the ab planes.

In the following subsections we show the behavior of the order parameters, spin angles, total magnetization, correlations and SO covariances for two paths in the phase diagram: from A-AF through canted-A-AF to FM phase (Sec. 3.4.3) and from striped-AF to G-AF phase (Sec. 3.4.4). Then we give a heuristic arguments for stability of the striped-AF phase in Sec. 3.4.5 and derive effective, perturbative spin Hamiltonians for canted-A-AF phase (Sec. 3.4.6) in the spirit of the derivation done for the 2D double-AF phase in Sec. 3.3.5. Further on, in Sec 3.4.7, we explain the absence of the C-AF phase in the cluster phase diagram of the 3D KK using similar method of perturbative expansion in the orbital sector. This explanation is also valid for the bilayer KK model. Finally, we describe briefly thermal evolution of canted-A-AF and striped-AF phases in Sec. 3.4.8 presenting the behavior of spin and orbital order parameters. The final summary and conclusions for the 3D KK model are given in Sec. 3.4.9 being the summary of the whole study on KK model presented here.

3.4.1 Single-site mean field

Repeating the reasoning and formulas from Sections 3.2.1 and 3.3.1 we can easily obtain single-site MF phase diagram for a 3D model. Like before, the starting point is an effective orbital Hamiltonian of the form

$$\begin{aligned} \mathcal{H}_{\rm MF} &= \frac{1}{2}J\sum_{i,\gamma}\left\{\tau_i^\gamma\tau_{i+\gamma}^\gamma(\chi^\gamma-\xi^\gamma)+\tau_i^\gamma\xi^\gamma-\frac{1}{4}(\chi^\gamma+\xi^\gamma)\right\} \\ &- E_z\sum_i\tau_i^c, \end{aligned} \tag{3.64}$$

where sums go over the sites of a square lattice, $\gamma=a,b,c$ and $i+\gamma$ is the nearest neighbor of site i in the direction γ. The coefficients,

$$\chi^\gamma = r_1\Pi_t^\gamma + r_2\Pi_s^\gamma, \quad \xi^\gamma = (r_2+r_4)\Pi_s^\gamma, \tag{3.65}$$

are the parameters obtained by averaging over spin operators with assumption that the spin order, determining χ^γ and ξ^γ, depends only on the direction γ and not on site i. Like in the bilayer case described in the Sec. 3.2.1 we will investigate phases with different long-range magnetic orders with appropriate mean values of singlet and triplet projectors $\Pi^\gamma_{s,t}$ given in Table 3.1. Apart from fully AF and FM phase we include also A-AF and C-AF configurations with spin correlations being AF in the c direction or in the ab planes, respectively, and FM otherwise. Solutions of the self-consistency equations and ground-state energies in different phases are obtained in the same way as described in previous sections.

The resulting phase diagram is shown in Fig. 3.20, area with AO phases is shaded in green. Remarkably, the diagram is almost the same as the one obtained for the bilayer system (see Fig. 3.2) and the major difference is the location of the multicritical point being now at $E_z = 0$ and $\eta = 0$ whereas for a bilayer it was $E_z = -0.25J$ and $\eta = 0$ (and for a single layer– $E_z = -0.5J$, $\eta = 0$). In the 3D case the cubic symmetry is obeyed by the model (3.63) at $E_z = 0$, while due to the shape of the z orbitals which are occupied in G-AFz phase and favor antiferromagnetism in the c direction the phase isless stable in the bilayer geometry, as explained said in Sec. 3.3.1. The C-AF with alternating orbitals also gets larger in 3D system but again, this phase will be completely absent in the cluster approach.

3.4.2 Cluster mean field

The cluster MF approach to the 3D KK model employs the same ideas and mathematical structures as in the 2D case (see Sec. 3.4.2), and we treat the 3D model as a generalization of the 2D one. The most natural choice of the cluster would be a cube with 8 sites as it was done in the bilayer case (see Fig. 3.3) but, since we want to keep two components of the spin order parameter and to study the thermal evolution of the model, we adopted here a simpler and less time-consuming approach and we consider 4-site clusters. The geometry of the clusters will depend on the direction in which we expect to have more quantum fluctuations. For example, if we want to study the transition between G-AF an A-AF phases then the reasonable cluster topology is a square in the ab plane, shown in Fig. 3.21(a), because during the transition the order along the c direction does not change. On the other hand, if we are interested in a transition between A-AF and FM phase where the order in the ab planes remain constant then the better choice is a chain along the c direction— see Fig. 3.21(b). As usually, the dashed lines outgoing from the vertices of the clusters shown in Fig. 3.21 are the MF interactions; to simulate infinite 3D lattice we need them in all three directions. In

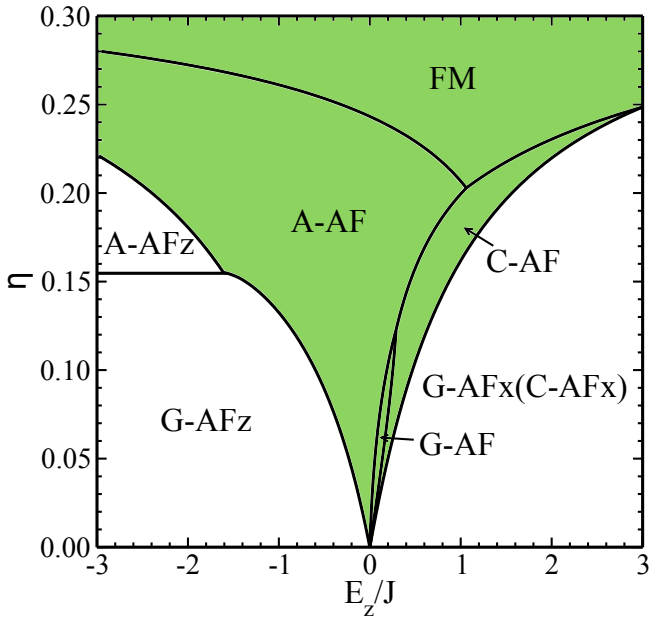

Figure 3.20: Phase diagram of the 3D KK model obtained in the single-site MF approximation. In this approach the FO AFx and C-AFx phases have exactly the same energy. Shaded green area indicates phases with AO order while the remaining magnetic phases are accompanied by FO order with fully polarized x or z orbitals.

the case of a square cluster we assume that the neighboring clusters in the c direction can have either the same spin configuration (gives FM bonds along the c axis) or inverted spin configuration (gives AF bonds along c). Furthermore, we assume that the neighbors in the ab plane can have either the same orbital configuration (gives AO and FO orders in the ab planes) or the orbital configuration is rotated by $\pi/2$ in the ab plane (gives PVB phase). Similarly, we assume that the chain clusters are copied without any change in the c direction and the neighboring chains in the ab planes have: (i) orbital configuration rotated by $\pi/2$ and (ii) spin configuration either inverted (gives planar AF) or left unchanged (gives planar FM). All these assumptions are necessary to solve the self-consistency problem and are motivated by the phase diagrams of 2D and bilayer systems (see Secs. 3.4.2 and 3.2.5).

The resulting phase diagram is shown in the Fig. 3.22. The yellow shading marks the PVB phase and the orange one indicates exotic magnetic orders. The orange phases are: double-AF phase already encountered in the 2D system, canted-A-AF phase and striped-AF phase. In the double-AF phase the order in the ab planes is such as depicted in Fig. 3.15 and this configuration repeats in the neighboring planes with a spin inversion meaning

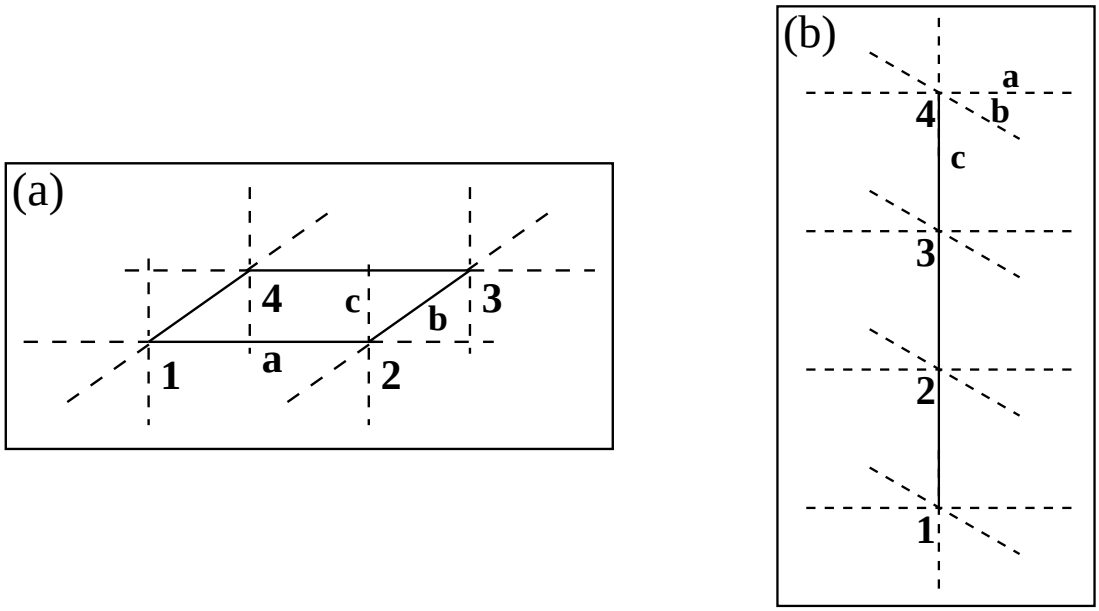

Figure 3.21: Schematic view of the clusters (solid lines) used in the cluster mean-field approach of Sec. 3.4.2 to the 3D KK model: (a) a plaquette in the ab plane, and (b) a chain in the c direction. Vertices $i = 1, 2, 3, 4$ and directions $\gamma = a, b, c$ are marked and dashed lines stand for the outgoing MF interactions with neighboring sites.

antiferromagnetism in the c direction. Note that this phase separates phases with in-plane antiferromagnetism (G-AF) and ferromagnetism (A-AF) which is the same as in the 2D case (see Fig. 3.14(a)). The interaction in the c direction are compatible with the in-plane magnetic order and even stabilize it as evidenced by the fact that the double-AF phase appears here for lower E_z than in the 2D phase. The double-AF phase with interplanar antiferromagnetism plays a role of the resonating valence-bond (RVB) phase found in the 3D KK model [27] where it was proposed as an intermediate phase between the G-AF and A-AF phases. We believe that the present result is more realistic than an RVB phase with 1D Heisenberg chains along c direction [27] would be infinitely susceptible to any in-plane magnetism because the 1D Heisenberg antiferromagnet is critical and thus unstable. We argue that the double-AF phase is well justified by the effective perturbative spin model derived in Sec. 3.3.5.

If we increase η in the A-AF phase we will encounter another magnetic transition, with spin correlations along c direction changing the sign. This is where the canted-AF phase appears as an intermediate phase connecting smoothly (in contrast to double-AF) the A-AF phase with FM one. In the canted-AF configuration the spins are FM in the ab planes and

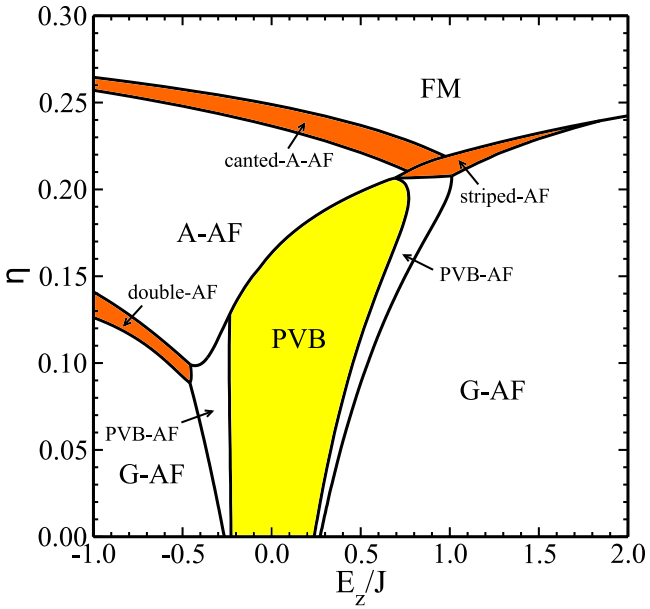

Figure 3.22: Phase diagram of the 3D KK model in the cluster MF approximation. Plaquette valence-bond phase with alternating spin singlets in the ab planes is highlighted in yellow. Phases with exotic magnetic order are shaded in orange.

the order along direction c changes gradually from AF to FM with interplane spin angle ϕ, being the canting angle, taking values between $\phi = 0$ and $\phi = \pi-$ see Fig. 3.23(b). On the other side of the phase diagram, for similar η, we find the striped-AF phase characterized by breaking of the symmetry between a and b directions in the orbital and spin sectors. The magnetic order in striped-AF phase is AF with anisotropy; along one direction in the ab plane the order is purely AF and in the perpendicular direction the angle between neighboring spins is close to π but not exactly π as shown in Fig. 3.23(a). The orbital configuration is FO with one preferred direction, i.e. $t^a \neq t^b$. Striped-AF phase connects with left G-AF phase by a smooth phase transition. Further on we will present some analytical arguments explaining both canted-AF (perturbative expansion) and striped-AF phase (heuresis).

The remaining part of the phase diagram, which is not shaded, contains well known magnetic phases including G-AF, A-AF and FM configurations placed similarly as in the single-site MF phase diagram of Fig. 3.20. The degeneracy between left G-AF and C-AF phase is removed again, as in the bilayer case (see Fig. 3.5), and this time we will provide a perturbative explanation of this fact. Similarly to the bilayer phase diagram, the PVB phase connects with the left G-AF phase by the intermediate PVB-AF configuration but due to

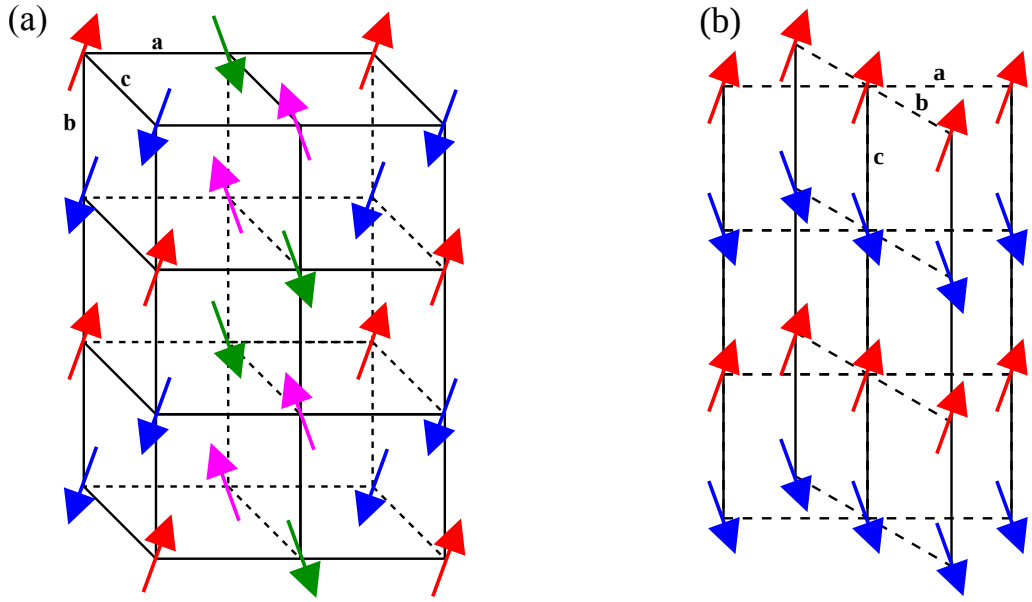

Figure 3.23: Schematic views of the two exotic spin orders realized by the 3D KK model: (a) striped magnetic order in the ab plane present in the striped-AF phase, with AF order in the c direction; (b) spin order realized in the canted-A-AF phase, see also Fig. 3.22.

the presence of the right G-AF phase we have also right PVB-AF phase. One can summarize that the whole bottom part of the phase diagram up to $\eta \approx 0.085$ contains only smooth phase transitions.

Before deriving the effective spin models for the new magnetic configuration found in the 3D KK model we will look more closely at the phase transitions connecting the A-AF and FM phases through the canted-A-AF configuration and striped-AF with the G-AF phase.

3.4.3 From A-AF to FM phase

In Figs. 3.24(a) and 3.24(b) we show the cosine of the spin canting angle ϕ in the c direction and the total magnetization $|s|$ defined in the following way:

$$\cos\phi = \frac{1}{s^2}\left(s_1^x s_2^x + s_1^z s_2^z\right), \qquad |s| \equiv \sqrt{\left(s^x\right)^2 + \left(s^z\right)^2}, \tag{3.66}$$

as functions of η in the A-AF, canted-A-AF and FM phases for $E_z = -0.5J$. For the AF configuration along c angle ϕ takes value $\phi = \pi$ and $\cos\phi = -1$, for FM order along c we have $\phi = 0$ and $\cos\phi = 1$. In the canted-A-AF phase $\cos\phi$ interpolates smoothly between these two values and remains constant in the A-AF and FM phases. Fig. 3.24(b) shows that

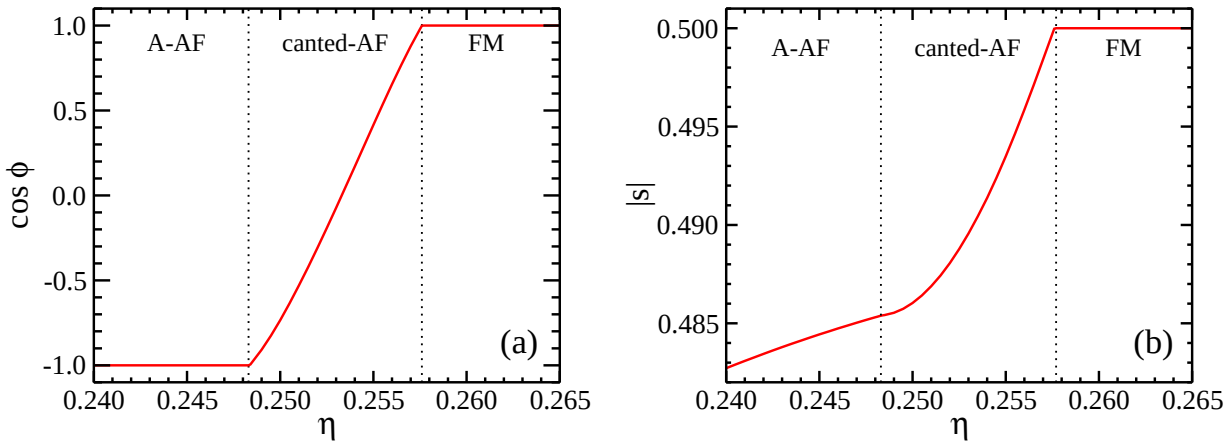

Figure 3.24: Evolution of the magnetic order for increasing η at $E_z = -0.5J$: (a) cosine of the canting angle ϕ, and (b) total magnetization $|s|$ both in the A-AF, canted-A-AF and FM phases from left to right.

the spin order in the considered range of η is almost classical with $|s|$ being close to 0.5, but quantum fluctuations arise when the spin order evolves away from the FM phase. In the canted-A-AF phase the slope of $|s|$ is the biggest and the quantum fluctuations drop rapidly with increasing η.

In Fig. 3.25(a) we show the behavior of the spin correlation functions $C_s^c(d)$ along the c direction for first, second and third NN neighbors ($d = 1, 2, 3$) in the chain cluster (see Fig. 3.21 (b)) for the same path in the phase diagram as before. First and third NN correlations confirm that the order along the c direction changes from AF to FM in a continuous way, with correlations passing through zero. The second NN correlation stays FM and almost constant in the whole range of η. This peculiar behavior will be explained by an effective perturbative spin Hamiltonian in Sec. 3.4.6. Fig. 3.25(b) presents the SO covariances; on-site $r^{a,b}$and bond $R^c(d)$ in the c direction for the range d. The on-site $r^{a,b}$ were already defined in the case of 2D system (see Sec. 3.3.4) and the d-range covariances are defined analogically to the NN ones as:

$$R^c\left(d\right) = \left\langle (\mathbf{S}_1 \cdot \mathbf{S}_{1+dc}) \tau_1^c \tau_{1+dc}^c \right\rangle - \left\langle \mathbf{S}_1 \cdot \mathbf{S}_{1+dc} \right\rangle \left\langle \tau_1^c \tau_{1+dc}^c \right\rangle . \tag{3.67}$$

As we could expect, in the FM phases all the covariances vanish and in the canted-A-AF phase their slope is the biggest. The $R^c(1)$ function is the one of the largest magnitude meaning that the configurations are highly bond-entangled on the short distance. In contrast to that, the longer range covariances $R^c(d)$ for $d > 1$ are close to zero but $R^c(3)$ as the only one becomes more significant in the canted-A-AF phase showing that this phase can be governed by higher

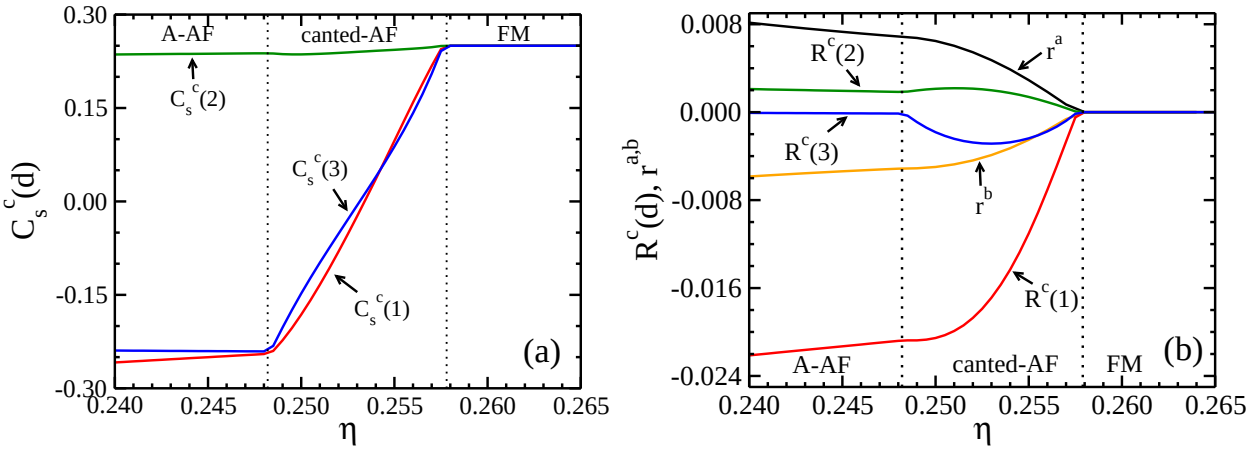

Figure 3.25: Evolution of spin and orbital correlations with increasing η for $E_z = -0.5J$: (a) spin correlation functions $C_s^c(d)$ in the c direction for distance d, and (b) on-site SO covariances $r^{a,b}$ and bond SO covariances $R^c(d)$ in the c direction for distance d in the A-AF, canted-A-AF and FM phases.

range spin interactions accompanied by large orbital fluctuations. The on-site covariances behave monotonically and take relatively small absolute values meaning that they are not of the prime importance in the considered phases.

3.4.4 From striped-AF to G-AF phase

Another new and exotic magnetic order of the 3D KK model is the striped-AF phase. This configuration can evolve smoothly towards the ordinary G-AF order when we increase E_z. In Fig. 3.26(a) we can see how the order parameters change when we go through this transition at $\eta = 0.22$. The orbital order parameters $t^{a,b}$ confirm breaking of the a-b symmetry in the striped-AF phase where they take slightly different values, the difference vanishes at the phase transition. In the magnetic sector we can distinguish four spin sublattices– see Fig. 3.23(a), two of which are not related by a spin inversion. To show the full complexity of the spin order we show spin averages on sites $i = 1, 3$ and both components $\alpha = x, z$. The behavior of curves confirms the striped character of the magnetic order in striped-AF phase vanishing at the transition point. In Fig. 3.26(b) we can see quantities derived out of the original order parameters being the cosines of the angle between the neighboring spins in a and b direction, $\phi^{a,b}$, and the total magnetization $|s|$, both defined as in Eq. (3.66). The behavior of $\cos\phi^b$ confirms the AF order along the b direction independent of E_z while in the b direction the angle ϕ^a changes from around $2\pi/3$ to π at the phase transition. After

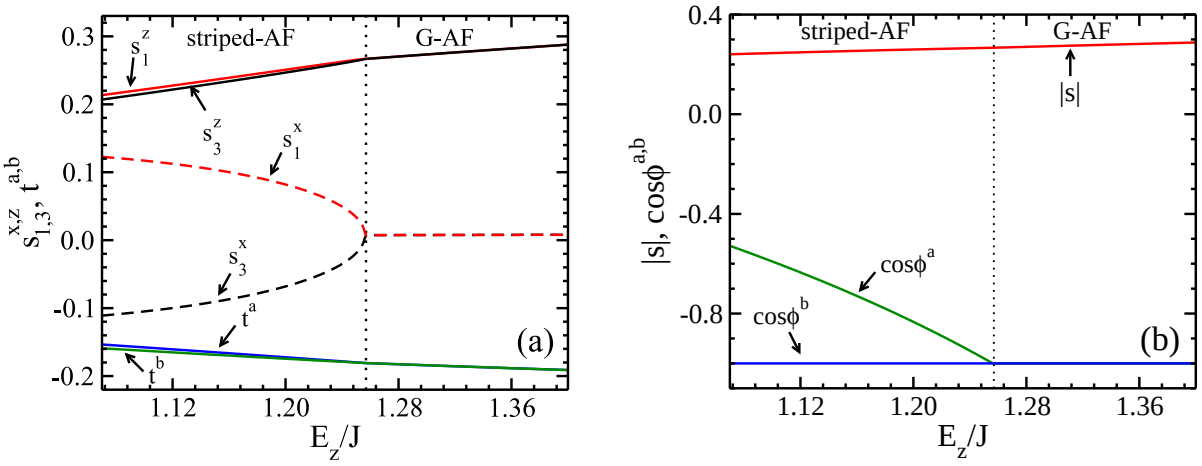

Figure 3.26: Evolution from the stripes-AF to G-AF phase at $\eta = 0.22$: (a) orbital $t^{a,b}$ and magnetic $s^{x,z}_{1,3}$ order parameters, and (b) total magnetization $|s|$ and cosines of spin angles ϕ^a and ϕ^b.

the transition the cosines remaining equal as expected in the isotropic AF phase. The total magnetization $|s|$ is almost constant, increasing monotonically when E_z grows, showing that the essential physics of the striped-AF phase lies in the spin angles, although its relatively low starting value means that striped-AF phase is affected by strong spin quantum fluctuation that weaken AF order.

In Figs. 3.26(a) and 3.26(b) we presented the on-site and bond SO covariances for the same parameter range as before. As we can see, the striped-AF phase exhibits relatively large on-site entanglement in x component of spin vanishing in the G-AF phase (see Fig. 3.26(a)) together with the entanglement in z component of spin that remains in the G-AF phase (see Fig. 3.26(b)). For the x component the dominating covariances are the ones in b direction and for the z component those in a direction. The fact that the z covariances remain in the G-AF is somewhat surprising as one could expect that this phase with no frustration and almost fully polarized FO configuration can be trivially factorized into spin and orbital wave functions. This turns out to be wrong and in Sec. 3.4.7 we will show that high order orbital fluctuation are essential for stabilizing AF order along the c direction in this phase.

3.4.5 Heuresis of the striped-AF phase

Striped-AF is the only phase of the 3D KK model that breaks the symmetry between a and b direction in the lattice. One can ask if there are any term in the Hamiltonian of Eq.

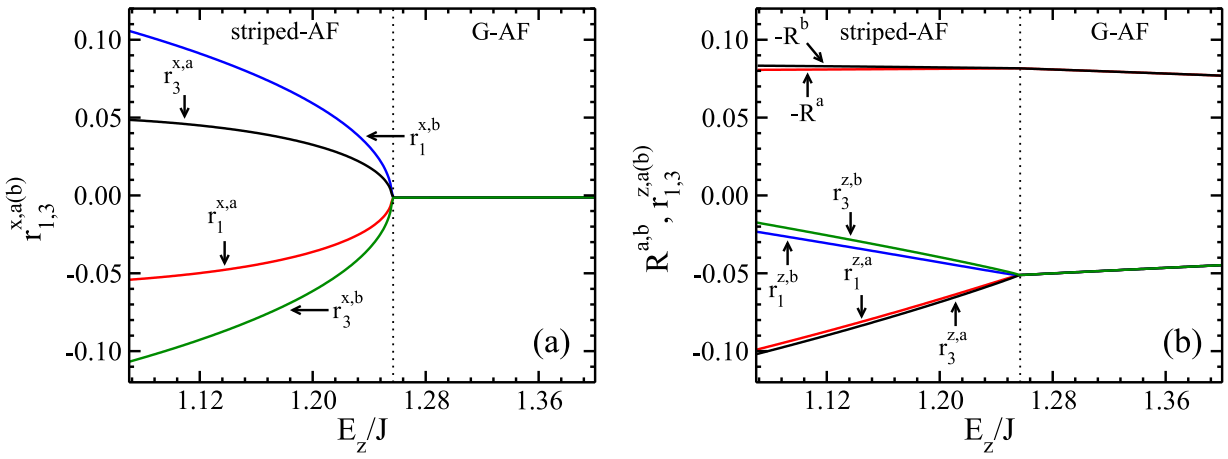

Figure 3.27: Evolution of covariances from the striped-AF to G-AF phase at $\eta = 0.22$ under increasing E_z/J: (a) on-site SO covariances $r^{x,a}_{1,3}$, $r^{x,b}_{1,3}$, and (b) $r^{z,a}_{1,3}$, $r^{z,b}_{1,3}$ together with bond SO covariances $R^{a,b}$.

(3.63) favoring such symmetry breaking. The answer is positive: the interaction between the orbitals is given by $\tau^\gamma_i \tau^\gamma_j$ terms that can be written as follows,

$$\tau^\gamma_i \tau^\gamma_j = \frac{1}{16}\left(\sigma^z_i\sigma^z_j - s_\gamma\sqrt{3}\sigma^z_i\sigma^x_j - s_\gamma\sqrt{3}\sigma^x_i\sigma^z_j + 3\sigma^x_i\sigma^x_j\right), \tag{3.68}$$

with sites i and j being nearest neighbors, and $s_\gamma = \pm 1$. According to Ref. [51], the Hamiltonian containing only these interactions alone with negative sing favors classical FM configurations in the σ^x_i components of the pseudospin. Such symmetry breaking is equivalent to the one observed in the striped-AF phase because:

$$\left\langle \tau^a_i - \tau^b_j \right\rangle = \frac{\sqrt{3}}{2}\left\langle \sigma^x_i \right\rangle. \tag{3.69}$$

In the full KK model the orbital interactions come together with spins as the terms:

$$\tau^\gamma_i \tau^\gamma_j \left\{ \left(\mathbf{S}_i \cdot \mathbf{S}_j\right)\left(r_1 + r_4\right) + \frac{3r_1 - r_4}{4} \right\} = A_{ij}\tau^\gamma_i \tau^\gamma_j, \tag{3.70}$$

may be represented by an effective orbital coupling A_{ij}— assuming that SO entanglement is low we can treat A_{ij} as numbers determined by the average spin-spin correlations. To stabilize the striped-AF phase we need all A_{ij} to be negative. This imposes a condition on the spin order, i.e.,

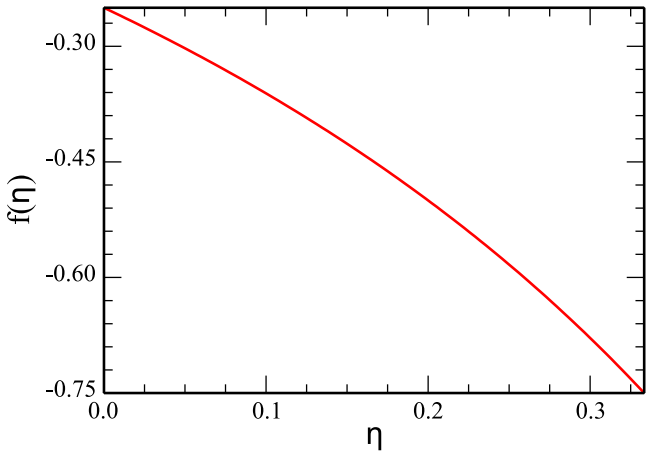

Figure 3.28: Plot of the function $f(\eta)$ (3.71) in the physical range of $\eta \in [0, 1/3)$. To stabilize striped-AF phase, the NN spin correlations should lie below the curve.

$$A_{ij} < 0 \Longleftrightarrow \langle (\mathbf{S}_i \cdot \mathbf{S}_j) \rangle < \frac{1}{4} - \frac{1}{2}\frac{1+\eta}{1-\eta} = f(\eta). \tag{3.71}$$

The $f(\eta)$ function is presented in Fig. 3.28. We can see that the condition (3.71) is possible to satisfy in the full physical range of η (meaning $f(\eta) > -3/4$) provided that quantum fluctuations in the spin sector are strong enough. This stays in odds with the fact that NN spin correlations are rather weak in the striped-AF phase but we have to remember that the explanation of the striped order given here lacks many details of the KK model with SO entanglement being the most notable. Nevertheless we argue that it captures the most important aspect of striped-AF phase which is the a-b symmetry breaking.

3.4.6 Effective spin model in the canted-A-AF phase

To explain the exotic magnetic order found in the canted-A-AF phase, displayed in Fig. 3.23(b) and described in Sec. 3.4.3, we derive an effective spin model for this phase at orbital degeneracy ($E_z = 0$). The idea is, as before, to use the standard quantum perturbation theory with degeneracy for the orbital sector of the KK model. We can divide the Hamiltonian given by Eq. (3.63) into the unperturbed part H_0 and perturbation V in the following way:

$$H_0 = \sum_{\substack{\langle i,j \rangle \| \\ \gamma=a,b}} \frac{3}{128}\left(3r_1 + r_4\right)\sigma_i^x \sigma_j^x - 3L^3 \frac{3r_1 + 2r_2 + r_4}{32}, \quad V = H - H_0. \tag{3.72}$$

In contrast to the previous calculations, done for the double-AF phase of the 2D system (see Sec. 3.3.5), the ground state $|0\rangle$ of H_0 is not a FO state but exhibits an AO order. This is because H_0 is a classical Ising model with AF interactions implying that $\langle\sigma_i^x\rangle = -\left\langle\sigma_{i+\gamma}^x\right\rangle$ or $\left\langle\tau_i^{a,b}\right\rangle = \left\langle\tau_{i+\gamma}^{b,a}\right\rangle$. Such choice of the unperturbed Hamiltonian is dictated by the results of cluster MF approach showing that canted-A-AF is an AO phase, just like A-AF and FM phases, so by taking FO ground-state we would miss the essential physics. Following the quantum perturbation theory we can construct the effective spin Hamiltonian H_s using the following expansion in powers of V,

$$H_s = E_0 + \langle 0|\, V\, |0\rangle + \sum_{n\neq 0} \frac{1}{E_n - E_0} \langle n|\, V\, |0\rangle^2 + O\left(V^3\right), \tag{3.73}$$

where the sums are over the excited states of H_0. In the zeroth order we get E_0, being the ground-state energy of the Hamiltonian H_0, and in the first order:

$$H_s^{(1)} = \sum_{\substack{\langle i,j\rangle \parallel \\ \gamma=a,b}} (\mathbf{S}_i \cdot \mathbf{S}_j)\, \frac{7}{32}(8r_2 - 7r_1 + r_4) + \sum_i (\mathbf{S}_i \cdot \mathbf{S}_{i+c})\, \frac{1}{8}(2r_2 - r_1 + r_4). \tag{3.74}$$

The NN interactions in the c direction vanish at $\eta = \eta_0 \simeq 0.236$ while the NN interactions in the ab planes are already FM in this region. The numerical results show that the in-plane ferromagnetism is very weakly fluctuating. For this reason we will assume that $\mathbf{S}_i\mathbf{S}_{i+\gamma} = 1/4$ for $\gamma = a, b$ and focus on the interactions in the c direction. In the second order V can produce two types of excited states: (i) with a single orbital rotated by $\pi/2$ in the ab plane, or (ii) with a rotated pair of neighboring orbitals. This leads to two type of terms in the interplanar Hamiltonian $H_{s,c}^{(2)}$:

$$\begin{aligned} H_{s,c}^{(2)} &= -\frac{32}{3\,(3r_1+r_4)} \sum_i (\mathbf{S}_i \cdot \mathbf{S}_{i+c}) \left\{ \frac{1}{320}\left(r_1^2 - r_4^2\right) - \frac{1}{6}\,(r_2 + r_4) \left(-\frac{1}{2} E_z + \frac{3}{32}(r_2 + r_4) \right) \right\} \\ &- \frac{32}{9\,(3r_1+r_4)} \sum_i (\mathbf{S}_{i-c} \cdot \mathbf{S}_{i+c})\, \frac{1}{128}\,(r_2+r_4)^2\,. \end{aligned} \tag{3.75}$$

The Heisenberg NN interactions pass through zero at the transition from the A-AF to FM phase; then the second NN interaction become important. According to the second line of Eq.

(3.75), these interactions are non-vanishing and favor ferromagnetism which agrees with the numerical result shown in Fig. 3.25(a). Now the remaining question concerns the physical mechanism for the non-trivial canting angle, interpolating between $\phi = \pi$ and $\phi = 0$ when passing from the A-AF to FM phase. The answer is found by considering the third order of the perturbative expansion given by:

$$H_s^{(3)} = \sum_{n\neq 0}\sum_{m\neq 0} \frac{1}{E_n - E_0}\frac{1}{E_m - E_0} \langle 0|\, V\, |n\rangle \langle n|\, V\, |m\rangle \langle m|\, V\, |0\rangle\,, \tag{3.76}$$

and the terms with three Heisenberg bonds multiplied by each other along the c direction. Such terms lead to the correction $H_{s,c}^{(3)}$ of the form:

$$H_{s,c}^{(3)} = \frac{22}{5\times 3^4}\frac{(r_2+r_4)^2\,(r_4+r_1)}{(3r_1+r_4)^2}\sum_i \left\{\frac{1}{8}\,(\mathbf{S}_{i+c}\cdot\mathbf{S}_{i-2c}) + \frac{1}{2}\,(\mathbf{S}_{i+c}\cdot\mathbf{S}_{i-2c})\,(\mathbf{S}_i\cdot\mathbf{S}_{i-c})\right\}, \tag{3.77}$$

where we used identity of Eq. (3.60) to simplify the product. Now, according to Fig. 3.23(b), if we use the classical expressions for the spin scalar product using the canting angle ϕ for the odd neighbors and the FM order for the even neighbors, i.e.,

$$\mathbf{S}_i\cdot\mathbf{S}_{i+(2n-1)c} = \frac{1}{4}\cos\phi, \quad \mathbf{S}_i\cdot\mathbf{S}_{i+2nc} = \frac{1}{4}, \tag{3.78}$$

with $n = 1, 2, 3, \ldots$, then we get the classical expression for the ground-state energy $E_0(\phi)$:

$$\begin{aligned} E_0(\phi) &= \frac{\cos\phi}{4}\left\{\frac{2r_2 - r_1 + r_4}{8} - O\left(\frac{32}{9\,(3r_1+r_4)}\right)\right\} + \frac{\cos^2\phi}{32}\frac{22}{5\times 3^4}\frac{(r_2+r_4)^2\,(r_4+r_1)}{(3r_1+r_4)^2} \\ &= \cos\phi A(\eta) + \cos^2\phi B(\eta). \end{aligned} \tag{3.79}$$

Such function has a non-trivial minimum at ϕ_0 as long as $B(\eta) > 0$ (which is the case here) given by the equation:

$$\cos\phi_0 = \begin{cases} -1 & for \quad A(\eta) < -B(\eta)/2 \\ -2\frac{A(\eta)}{B(\eta)} & for \quad |A(\eta)| < B(\eta)/2 \\ 1 & for \quad A(\eta) > B(\eta)/2, \end{cases} \tag{3.80}$$

with functions $A(\eta)$ and $B(\eta)$ defined by Eq. (3.79). This reproduces well the behavior of $\cos\phi$ obtained via cluster MF method.

3.4.7 Effective model in the G-AF phase: G-AF versus C-AF order

In this subsection we will derive an effective spin Hamiltonian around the FO ordered state with x orbitals occupied to explain the energy difference between the G-AF and C-AF phase, favoring the G-AF order in the cluster MF approach (see Fig. 3.22). As in Sec. 3.3.5 we can divide the Hamiltonian given by Eq. (3.63) into the unperturbed part H_0 and perturbation V in the following way:

$$H_0 = -E_z \sum_i \tau_i^c, \tag{3.81}$$

$$V = V_{ab} + V_c, \tag{3.82}$$

with perturbation splitted into planar V_{ab} and interplanar V_c part given by:

$$V_{ab} = -\frac{1}{2}\sum_{\substack{\langle i,j\rangle \parallel \\ a,b}} \left\{ (r_1\,\Pi_t^{(ij)} + r_2\,\Pi_s^{(ij)}) \left(\frac{1}{4} - \tau_i^\gamma \tau_j^\gamma\right) + (r_2 + r_4)\,\Pi_s^{(ij)} \left(\frac{1}{2} - \tau_i^\gamma\right)\left(\frac{1}{2} - \tau_j^\gamma\right)\right\}, \tag{3.83}$$

$$V_c = -\frac{1}{2}\sum_{\langle ij\rangle \| c} \left\{ (r_1\,\Pi_t^{(ij)} + r_2\,\Pi_s^{(ij)}) \left(\frac{1}{4} - \tau_i^c \tau_j^c\right) + (r_2 + r_4)\,\Pi_s^{(ij)} \left(\frac{1}{2} - \tau_i^c\right)\left(\frac{1}{2} - \tau_j^c\right)\right\}, \tag{3.84}$$

where for simplicity we take the units of $J = 1$. For positive E_z the ground state $|0\rangle$ of H_0 is the state with all orbitals being the x orbitals, i.e.,

$$\forall i: \quad \tau_i^c\,|0\rangle = \frac{1}{2}\,|0\rangle \tag{3.85}$$

with energy $E_0 = -\frac{1}{2}E_z L^3$. Using Eq. (3.73) we can construct the effective spin Hamiltonian H_s as a power expansion in V. Note that the ground state $|0\rangle$ is an eigenstate of V_c to zero eigenvalue; for this reason V_c gives no contribution to H_s up to second order in V and the interplane interactions appear as E_z^{-2} terms. The effective spin Hamiltonian H_s up to second order in V can be calculated in the same way as in Sec. 3.3.5 and contains the same spin interactions:

$$
\begin{aligned}
H_s &= \sum_{\langle i,j\rangle} (\mathbf{S}_i \cdot \mathbf{S}_j) \left\{ 3\frac{4r_2 - r_1 + 3r_4}{32} + O\left(E_z^{-1}\right) \right\} + \frac{1}{E_z} \sum_{\langle\langle i,j\rangle\rangle} \frac{3}{2^{10}} (\mathbf{S}_i \cdot \mathbf{S}_j) (2r_2 + r_4 - r_1)^2 \\
&- \frac{1}{E_z} \sum_{\langle\langle\langle i,j\rangle\rangle\rangle} \frac{3}{2^{11}} (\mathbf{S}_i \cdot \mathbf{S}_j) (2r_2 + r_4 - r_1)^2 + O\left(E_z^{-2}\right), \qquad (3.86)
\end{aligned}
$$

where all bonds are in the ab planes. Again, one can think of a double-AF phase similar to the one obtained in the limit of $E_z \to -\infty$ for η close to η_0 where the NN interactions vanish (in this case $\eta_0 \simeq 0.2915$) but this is not our aim in this subsection– we search for an effective description of the interplane interactions. Looking at the third order correction to H_s given in Eq. (3.76) and at the form of V_c we can see that the interplane part of the third order correction $H_{s,c}^{(3)}$ has the following structure:

$$
H_{s,c}^{(3)} = \sum_{n \neq 0} \frac{1}{(E_n - E_0)^2} \langle 0| V_{ab} |n\rangle \langle n| V_c |n\rangle \langle n| V_{ab} |0\rangle . \qquad (3.87)
$$

This can be greatly simplified if we take into account two facts: (i) V_{ab} can excite only single orbitals or pair of neighboring orbitals so the sum over n turns into the sum over excited sites i and (ii) V_c is non-zero only around the excited orbitals. After the simplification we get,

$$
\begin{aligned}
H_{s,c}^{(3)} &= -\frac{3}{E_z^2} \frac{r_1 - r_2}{2^{11}} (2r_2 + r_4 - r_1)^2 \sum_i \sum_{\substack{\gamma = \pm a, \\ \pm b}} \sum_{\substack{\gamma' = \pm a, \\ \pm b}} s_\gamma s_{\gamma'} (\mathbf{S}_i \cdot \mathbf{S}_{i+\gamma}) (\mathbf{S}_i \cdot \mathbf{S}_{i+c}) (\mathbf{S}_i \cdot \mathbf{S}_{i+\gamma'}) \\
&- \frac{9}{4E_z^2} \frac{r_1 - r_2}{2^{11}} \sum_i \sum_{\substack{\gamma = \pm a, \\ \pm b}} \left[(\mathbf{S}_i \cdot \mathbf{S}_{i+\gamma}) (r_1 + r_4) + \frac{3r_1 - r_4}{4} \right] (\mathbf{S}_i \cdot \mathbf{S}_{i+c}) * \\
&* \left[(\mathbf{S}_i \cdot \mathbf{S}_{i+\gamma}) (r_1 + r_4) + \frac{3r_1 - r_4}{4} \right], \qquad (3.88)
\end{aligned}
$$

where the first line originates from the single-orbital excitations and the second from orbital-pairs excitations. The interplane interactions are typically sandwiched between two in-plane bonds; this can be treated with the following spin identity:

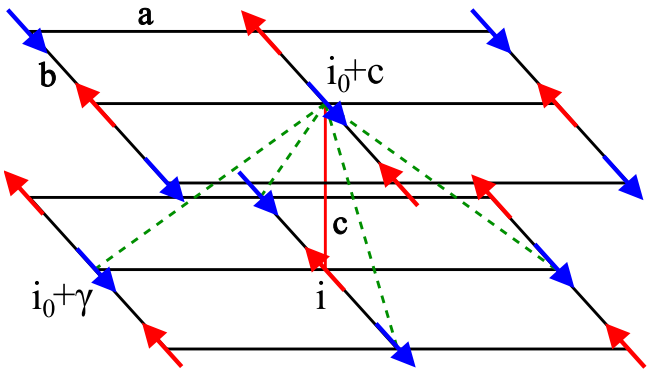

Figure 3.29: Schematic view of the G-AF spin order on the two planes of 3D cubic lattice stabilized by the third-order NNN Heisenberg interactions (green dashed lines) between sites $i_0+\gamma$ and i_0+c being FM (see Eq. (3.90)). The NN FM interactions between i_0 and i_0+c (red line) are incompatible with G-AF order but they are four times less numerous.

$$\begin{aligned}(\mathbf{S}_i\cdot\mathbf{S}_{i+\gamma})\,(\mathbf{S}_i\cdot\mathbf{S}_{i+c})\,(\mathbf{S}_i\cdot\mathbf{S}_{i+\gamma'}) &= \frac{1}{4}\,(\mathbf{S}_{i+c}\cdot\mathbf{S}_{i+\gamma})\,(\mathbf{S}_i\cdot\mathbf{S}_{i+\gamma'})-\frac{1}{4}\,(\mathbf{S}_{i+\gamma'}\cdot\mathbf{S}_{i+\gamma})\,(\mathbf{S}_i\cdot\mathbf{S}_{i+c})\\ &+ \frac{1}{4}\,(\mathbf{S}_i\cdot\mathbf{S}_{i+\gamma})\,(\mathbf{S}_{i+c}\cdot\mathbf{S}_{i+\gamma'})+i\frac{1}{8}\mathbf{S}_{i+\gamma}\cdot(\mathbf{S}_{i+c}\times\mathbf{S}_{i+\gamma'})\,.\end{aligned} \tag{3.89}$$

After using this and the identity of Eq. (3.56), the $H^{(3)}_{s,c}$ correction is ready for final approximation—we assume that the spins form classical AF state in the ab planes, i.e., $(\mathbf{S}_i\cdot\mathbf{S}_{i+\gamma})\equiv-\frac{1}{4}$ for $\gamma=a,b$. Of course, this is not completely true because we neglect quantum fluctuations but these should be small in the 3D long-range ordered magnetic configuration being either G-AF or C-AF. The final formula for interplane interactions is:

$$H^{(3)}_{s,c}=-\frac{9}{4E_z^2}\frac{r_1-r_2}{2^{10}}\sum_i\left[(\mathbf{S}_i\cdot\mathbf{S}_{i+c})\,r_1\,(r_1-r_4)+\sum_{\substack{\gamma=\pm a,\\ \pm b}}(\mathbf{S}_{i+c}\cdot\mathbf{S}_{i+\gamma})\,(r_1+r_4)\,\frac{3r_1-r_4}{4}\right], \tag{3.90}$$

containing NN and NNN Heisenberg bonds both favoring ferromagnetism. This could lead to frustration as the NN bonds favor C-AF state while the NNN bonds prefer G-AF but one can easily check that the number of NNN bonds per site is four times larger than that of NN bonds (see Fig. 3.29). If we take into account this factor of 4 comparing the coupling

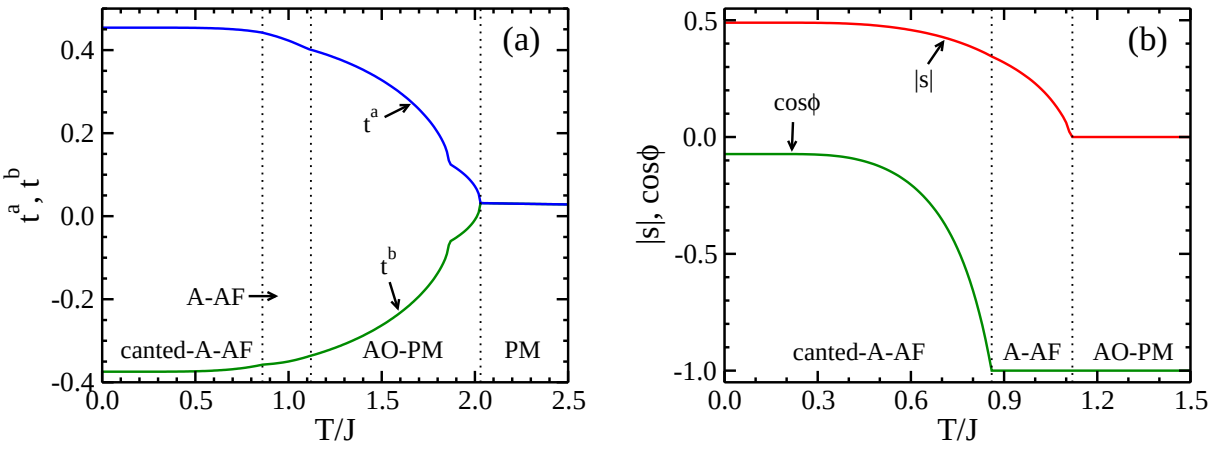

Figure 3.30: Thermal evolution of the orbital and magnetic order in the canted-A-AF, A-AF, AO-PM and PM phases for $E_z = -0.5J$, $\eta = 0.253$ and increasing T: (a) orbital $t^{a,b}$ mean fields for $0 < T < 2.5J$; (b) cosine of the canting angle ϕ and total magnetization $|s|$ for $0 < T < 1.5J$.

constants J_{NNN} and J_{NN} of the NN and NNN interactions we obtain:

$$4J_{NNN} - J_{NN} = (r_1+r_4)(3r_1-r_4) - r_1(r_1-r_4) = 4\frac{1+\eta(1-4\eta)}{(3\eta^2+2\eta-1)^2} > 0 \qquad (3.91)$$

in the physical range of η, $\eta \in [0, 1/3)$. This finally shows why the G-AF phase is favored over the C-AF phase both in the 3D and bilayer case, as long as we go beyond the single-site MF approximation which cannot capture the subtle third-order orbital fluctuations (compare Figs. 3.2 with 3.5 and 3.20 with 3.22).

3.4.8 Thermal decay of the canted-A-AF and striped-AF orders

Finally, after determining the most important properties of the 3D KK model in zero temperature, we can study the effects of thermal fluctuations in the exotic magnetic phases. For double-AF phase we have checked that the thermal evolution does not lead to any new configurations comparing to the double-AF phase in the 2D model (see Sec. 3.3.4) so we will focus on canted-A-AF and striped-AF phases only.

In Figs. 3.30(a) and 3.30(b) we show thermal evolution of orbital and magnetic order in the canted-A-AF phase for $E_z = -0.5J$ and $\eta = 0.253$. We argue that these values of E_z and η are representative for the whole canted-A-AF phase, at least away from the transitions to

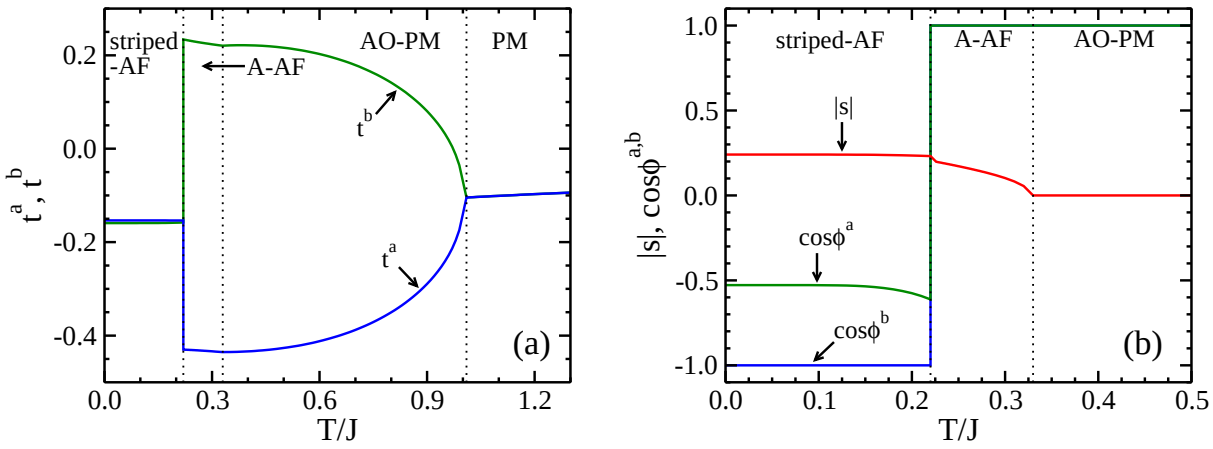

Figure 3.31: .Thermal evolution of the orbital and magnetic order in the striped-AF, A-AF, AO-PM and PM phases for $E_z = 1.07$, $\eta = 0.22$ and increasing T: (a) orbital $t^{a,b}$ mean fields for $0 < T < 1.3J$; (b) cosines of the canting angles $\phi^{a,b}$ and total magnetization $|s|$ for $0 < T < 0.5J$.

neighboring phases. As we can see in Fig. 3.30(a) the AO order persists up to relatively high temperature of $T \approx 2J$ where it changes into FOz one which is induced here by the crystal field E_z. Due to the cluster geometry, which is a chain, the external sites $i = 1, 4$ feel different interactions than the internal ones (see Fig. 3.21(b)). For this reason it is possible that the orbital mean fields for external sites are already as in the FO phase while the internal ones are still alternating. This happens at $T \approx 1.8J$ and causes the characteristic bends of the $t^{a,b}$ curves which are already averaged over all cluster sites. On the way from canted-AF to PM phase not much happens in the orbital sector but as we see in Fig. 3.30(b) there are two magnetic phase transitions. At the first one the canting angle ϕ becomes trivial and canted-A-AF becomes ordinary A-AF. The total magnetization $|s|$ does not feel this transition and remains finite until the second one at $T \approx 1.1J$ where the A-AF collapses to the AO-PM phase with no magnetic order. One can expect that for higher η the thermal evolution would involve the FM instead of A-AF phase as the first effect of thermal fluctuation is destroying the non-trivial canting angle.

Figs. 3.31(a) and 3.31(b) show thermal evolution of orbital and magnetic order in the striped-AF phase for $E_z = 1.07$ and $\eta = 0.22$. Looking at Fig. 3.30(a) we see that the orbital order favoring one direction in the ab plane persists up to relatively low temperature of $T \approx 0.2J$ and gets replaced by the AO order which remains until $T \approx 1J$ and then melts down to FO order. The transition between striped-AF and A-AF phases is discontinuous and involves the change in the symmetry of orbital configuration thus the $t^{a,b}$ parameters in the

striped-AF phase have different meaning than $t^{a,b}$ in the A-AF phase. The indication of this first order phase transition is the crossing of free energy levels. In Fig. 3.31(b) we can see the magnetic part of the thermal evolution; striped-AF order remains almost constant until the free energy crossing and then the cosines jump to a single value of $\cos\phi^{a,b} = 1$ meaning full ferromagnetism in the ab planes. The interplane spin correlation remain negative and thus we are in the A-AF phase. At the same total magnetization $|s|$ remains continuous and starts to drop gradually towards zero at the transition to the AO-PM phase which is of the second order. The constancy of $|s|$ at the point of first transition means that the free energy depends strongly on total magnetization and not on angles $\{\phi^a, \phi^b\}$.

3.4.9 Summary and conclusions

Summarizing, we have presented rather complete description of the 3D KK model in the framework of the cluster MF theory and effective perturbative models. We argue that the striped-AF phase, representing new type of symmetry breaking in the whole class of KK models considered here, still requires more advanced approach than the one that was implemented here. This heuristic approach explains the a-b symmetry breaking as the breaking of the Z_2 symmetry in the space of orbital pseudospins but leaves some questions unanswered. Firstly, we cannot derive any effective, perturbative Hamiltonian for this phase as it appears in the intermediate coupling regime and it is not clear what the reference configuration should look like. On the first glance, one could propose the FOx ordered state but this will lead to an effective Hamiltonian favoring double-AF state which is not what we wish for. Secondly, it is hard to claim that the striped-AF phase is a consequence of proximity of the FM phase, as there is no smooth phase transition from striped-AF to FM phase. And finally, it is not clear why this phase appears only in the 3D case; we have checked that it converges to a stable solution in the 2D case but with energy being always higher than that of either the G-AF or FM phase.

On the contrary, we managed to obtain a very clear picture in the left part of the phase diagram, with a sequence of phase transitions, occurring for increasing η, involving intermediate phases with exotic magnetic orders. This sequence is caused by the first order NN Heisenberg interactions changing their sign first in the ab planes, which stabilizes double-AF phase, and then along the c direction, which leads to a canted-A-AF configuration. In both cases we found perturbative expansions around certain orbital configurations explaining these new magnetic orders. In case of the double-AF phase the effective Hamiltonian is the same as

for the 2D KK model with additional AF interactions in the c direction. In the other case the intermediate configuration turned out to be essentially classical, with FM planes dumping any quantum fluctuations, and we used this fact to construct the effective spin model around the AO configuration to explain canted-A-AF ordering.

To supplement these analytical consideration we presented the plots of order parameters, correlations and SO covariances for the two cuts in the phase diagram, passing through canted-A-AF and striped-AF phases. They show that both phases involve SO entanglement and the plots for the canted-A-AF phase are supported by the effective spin Hamiltonian derived for this phase. The plots for double-AF phase were already given in the 2D case and its properties for the 3D lattice are very similar.

As the last analytical result we showed the derivation of the effective spin Hamiltonian for the FOx configuration which explains why the G-AF phase always wins with the C-AF configuration for 3D and bilayer systems although these two phases are degenerate in the single-site MF approach. The answer was found in the third order of the perturbation expansion and it was showed that the AF order in the c direction is induced by the two effects: (i) AF order in the ab planes, and (ii) NNN interaction between the planes being FM. This demonstrates that the right G-AF phase is highly SO entangled, because we need third order orbital fluctuations to stabilize the spin order, and agrees with the plots of SO covariances presented for the bilayer KK model.

The results at finite temperature obtained in the canted-A-AF and striped-AF phases indicate that the striped order is easily destroyed by thermal fluctuations whereas the canted-A-AF phase is more robust and a non-trivial canting angle can be found up to relatively high temperatures. This can be easily understood if we think of canted-A-AF phase as a classical configuration while the striped-AF phase is affected by strong quantum fluctuations; the energy scales for magnetic excitations must be much higher in the canted-A-AF phase. Again, the orbital order turned out to be more stable than the magnetic order.

Although the phase diagram obtained for the 3D KK model is similar to the one presented in Ref. [27], there is one major difference. The intermediate phase between the G-AF and A-AF phases on the left, here being the double-AF phase, was claimed to be a valence bond phase with resonating singlets in the c direction [27]. Our results do not support such configuration and the effective spin Hamiltonian we derived cannot reproduce such a result. This means that the 3D KK model in our approach excludes any signatures of the 1D Heisenberg physics reported for $KCuF_3$ [88] which suggests that the KK model is not enough to correctly describe $KCuF_3$ and should be supplemented by other terms. This seems to

be confirmed by the latest papers on $KCuF_3$ where authors supplement the KK model with additional spin interaction [86] or additional degrees of freedom [85] to explain the properties of this compound. We believe that only the second option is true.

3.5 Final remarks on the Kugel–Khomskii model

Finally, we would like to remark that experimental phase diagrams of strongly correlated transition metal oxides are one of the challenging directions of current research. Systematic trends observed for the onset of the magnetic and orbital order in the $R\mathrm{VO}_3$ perovskites (where R=La, ...) have been successfully explained by the competing interactions in presence of SO entanglement [95]. In contrast, the theory could not explain exceptionally detailed information on the phase diagram of the $R\mathrm{MnO}_3$ manganites which accumulated due to impressive experimental work [113].

Summarizing, the presented analysis demonstrates that SO entanglement plays a crucial role in complete understanding of the phase diagram of the bilayer, 2D and 3D KK model. By introducing additional SO order parameter for a bilayer, independent of spin and orbital mean fields we obtained new phases in highly frustrated regime of parameters. By including additional component of spin as an order parameter we managed to capture the most important features of the AF-FM phase transitions for 2D and 3D system both in ab planes and c direction which are the intermediate phases with exotic spin order. What more, we managed to support and interpret our numerical results with the help of an analytical approach based on the perturbation expansion in the orbital sector leading to effective spin Hamiltonians.

We argue that the cluster method we used here is sufficiently realistic to investigate the phase diagrams of the KK models on various lattices, and could be applied to other SO superexchange models adequate for undoped transition metal oxides.

Chapter 4

Final summary and conclusions: frustration and entanglement

Thus, by joint analytical and numerical effort we managed to extract some interesting properties out of the Hamiltonians of quantum compass and Kugel-Khomskii models which are indeed simple to write but rather non-trivial to solve. The solvability is unquestionable only in case of a ladder compass model which can be mapped to the quantum Ising model thanks to the special symmetries of the QCM. In a 2D QCM these symmetries do not lead to the solution but reduce considerably the number of degrees of freedom. This is useful only in case of small lattices as the reduction is of the order of linear size of the system. On the other hand, this has a consequence in self-duality of the 2D QCM in the thermodynamic limit, which is not the case for the ladder, where XX and ZZ interactions act in inequivalent directions. As a result the quantum phase transitions for 2D and ladder QCM are of different types; for a ladder the energy spectrum becomes quasi-continuous at the critical point as it happens in the QIM, whereas for a 2D system the spectrum remains discrete in its low-energy part and only the ground-state degeneracy becomes exponential in the linear size of the system. The behavior of the von Neumann entropy of the subsystem being a single line in a 6×6 lattice confirms that the QPT found in the 2D QMC at the isotropic point is of the second order which stays in agreement with the NN spin correlation functions exhibiting no discontinuity. The heat capacity obtained both for ladder and planar QCM indicates the existence of two energy scales in finite systems. The larger one can be associated with classical Ising exicitations, being the single spin flips, whereas the other one can be related to the Bogoliubov quasiparticles in case of a ladder system. These quasiparticles become gapless in

the thermodynamic limit and form a quasi-continuum thus the low-temperature peak in the heat capacity remains for an infinte ladder. In contrast to that, the heat capacities obtained for 2D QCM for increasing system sizes L show that the low-temperature peak vanishes for $L \to \infty$, so we can argue that the quasiparticles (e.g. the ones defined in a non-local MF approach of Sec. 2.2.1) remain gapped in the 2D case. This is coherent with the existence of an ordered phase in 2D QCM found above $T_c = 0.055J$ [49].

In the case of the KK model the question of solvability is trivial. The model is inherently unsolvable. Already the Heisenberg model in more than one dimension has no exact solutions and here it is coupled to a frustrated orbital problem. For this reason the approximate approaches are fully justified, including single-site and cluster mean-field approximations together with various perturbative expansions. The first two methods have one unquestionable advantage– we do not have to assume anything about spin and orbital configuration of the model for a given values of the parameters E_z and η. This is especially true for a single-site MF approach in which we obtained the phase diagrams of the KK model in all three cases of a 2D, bilayer, and 3D lattice. Already in this simple framework the results are non-trivial, revealing a multicirtical point at Hund's exchange $\eta = 0$ and crystal-field splitting $E_z = -1/2, -1/4, 0$ for a 2D, bilayer, and 3D lattice respectively. At this special points the phases with FOz, FOx and AO orders become degenerate and different magnetic orders cross, including fully AF and FM phases for a 2D system or fully AF and planarly FM phases both for 3D and bilayer systems. From the point of view of number and types of different configurations the 3D and bilayer systems are almost the same– the difference is only visible in a cluster approach when the bilayer geometry can favor interlayer singlets. Once more we emphasize that the G-AF phase with FOx order in a single-site MF approach is always degenerate with the C-AFx phase for a 3D and bilayer lattices and this degeneracy is lifted in a cluster approach. Another special feature of the single-site MF phase diagrams is the existence of the two classes of orbital orders, never connected in a smooth way, one when the orbitals are frozen in classical FOx or FOz configurations and the other when the orbitals alternate (AO order). Such fully classical orbital orderings are unstable in a cluster approach, away from the limit of $|E_z| \to \infty$, when they are subject to quantum fluctuations and depend strongly on values of E_z and η.

The applitaction of the cluster MF method to the KK model provided remarkably good results. First of all, the considerable number of phase transitions became smooth and the new phases occured. The area in between the two G-AF phases with FOz and FOx orders, previously dominated by the multicritical point, now became a part of a PVB phase for

all three lattice geometries (see Secs. 3.2.5, 3.3.3 and 3.4.2). Therefore, the multicritical point was moved to the higher values of η meaning that the most frustrated part of the phase diagram is in fact at a finite Hund's exchange. In case of a bilayer lattice the cluster approach additionally stabilizes the inerlayer-singlet phases (VBz and VBm) which substitute the G-AF phase in the regime of negative E_z and agree with the observed properties of $K_3Cu_2F_7$ [105]. What more, by taking the non-factorized SO mean fields we managed to capture the effects of SO entanglement resulting in stable ESO and EPVB phases for a bilayer system and intermediate PVB-AF phases both in a bilayer and 3D systems. Additionally, by including more than one component of a spin mean field into the cluster MF Hamiltonian we obtained another new configurations with exotic spin order namely; double-AF phase for 2D and 3D lattices and canted-A-AF together with striped-AF phases for a 3D lattice. These phases turned out to be an effect of the AF-FM transitions, driven by the increasing Hund's exchange η, taking place either in the ab plane(s) (this stabilizes the double-AF phase) or along the c axis (this stabilizes the canted-A-AF phase) and this statement was proved rigorously by perturbative expansions in the orbital sectors of the KK model. In case of the striped-AF phase no such proof was given but a heuristic reasoning shows that this phase, characterized by a symmetry breaking between a and b directions in the lattice, can be stable as long as the AF exchange is strong enough despite the increasing η. In that sense the striped-AF phase can be treated as another intermediate configuration in the area of the AF-FM transition with strong on-site SO entanglement (see Sec. 3.4.4). Finally, the cluster MF approach showed that the degeneracy between C-AF and G-AF found in the single-site approximation is artificial and the C-AF phase is absent in the realistic system described by the KK model, both for a 3D and a bilayer lattice. Again, this was also rigorously proved by a perturbative expansion in the orbital sector.

At finite temperature the cluster MF method provided another non-trivial results. Both for 2D and 3D lattices it confirmed the general obeservation, valid e.g. for $LaMnO_3$ [9], that the orbital ordering occurs at much higher temperature than the magnetic one. This is because the orbital part of the KK Hamiltonian can be regarded as more classical, due to the form of interactions that resemble classical Ising bonds, and the energy scales for excitations in the orbital sector are higher than in the spin sector. On the other hand, when the exotic magnetic order occurs and the temperature is increased, it can either first decay to an ordinary one, as it happens in the canted-A-AF and striped-AF phases (see Secs. 3.4.8), or decay directly to a paramagnet, like the double-AF phase (see Sec. 3.3.4). Finite-temperature phase diagrams of the 2D KK model show that the orbital order can

greatly support the magnetic one against thermal fluctuation. This happens to the G-AF phase in the regime of positive E_z when antiferromagnetism remains stable up to relatively high temperature of $T = 0.34J$ whereas the spin order in the negative-E_z area is already gone. Similarly, the singlet PVB phase is also stable at this temperature as the valence-bond configuration is accompanied by the orbital order with cigar-shaped orbitals pointing at each other along the singlet bonds. On contrary to that the FM phase can become paramagnetic without losing AO order and this gives AO-PM phase. In general, any on-site or bond SO entanglement is expected to be suppressed at finite temperature as it happens in the double-AF phase, at least in terms of the introduced SO covariances and we argue that the pure quantum entanglement cannot be distinguished from the thermal mixing in such case.

We suggest that the models we considered are frustrated only for some special choice of parameters. As a matter of fact this question is clear only in case of classical Hamiltonians where interaction terms commute with each other. For example, in the ground state of finite size ladder or 2D lattice QCM both x and z- part of the Hamiltonian give a negative contribution to the total ground-state energy meaning that they are not frustrated. The situation changes in the thermodynamic limit of the 2D QCM when the system orders according to the dominating interaction and the other one is ignored or, in the isotropic QCM, the spontaneous symmetry breaking occurs and one of the interactions becomes favored. Is such case we may say that the disfavored interaction is marginally frustrated, in the sense that it gives zero (or rather 0^+) contribution to the total energy in the limit of $L \to \infty$. As we see, the question of frustration of the 2D QCM is never as transparent as in the canonical case of a triangle of Fig. 1.2. On the other hand, the ladder QCM seems to be not frustrated for any system size and the infinite degeneracy of the ground state in the thermodynamic limit should be attributed to quantum criticality.

A different, and maybe more practical approach to the problem of frustration can be formulated in the quantum Monte Carlo (QMC) framework. We can argue that a spin (or pseudospin) system is frustrated if we encounter the so-called sing problem, meaning that we cannot define transition probabilities from one state of the system to another in order to calculate the partition function with classical action. This criterion is good because it uses classical version of a Hamiltonian and brings us back to the triangle showed in Fig. 1.2. The drawback of such definition is that it is not always obvious if a Hamiltonian has the sign problem; sometimes it can be cured by a change of representation. It is clear that if go to the eigenbasis of the Hamiltonian then the transition probabilities will be easy to define in any case– this is of course completely impossible in practice but shows that the sign problem

depends on the basis. Nevertheless the definition of frustration based on QMC approach has its sense even if we have no idea about these subtleties; we can say that the model is frustrated if no QMC results for such model appear in the literature in a reasonable time. Using this criterion and looking into Ref. [49] we argue that indeed, QMC in two dimensions is not frustrated, at least not for finite system sizes.

The same reasoning as above brings us to the conclusion that the KK model is frustrated because no QMC results for this model have appeared since 1972, when the model was invented. This can be found surprising, as the KK model is nothing more than a Heisenberg model coupled to an orbital model on a square lattice. Inserting FO configuration in the orbital sector, which is justified for large $|E_z|$, leaves us with pure Heisenberg model with no frustration. This is however not the whole truth. As we could see in the previous chapter, the fact that FO configuration is not an eigenstate of the orbital Hamiltonian has its consequences, one of which is the energy gap between C-AF and G-AF configurations in 3D KK model caused by the third order orbital fluctuations. In general, it is the orbital sector that is responsible for the frustration in the KK model [27] while the spin interactions often remain not frustrated. The most notable example of such behavior is the double-AF phase, found both in the 2D and 3D KK model, stabilized by the second and third order orbital fluctuations around the FOz configuration, where the effective Hamiltonian describes two independent $J_1 - J_2$ models on two sublattices. Thereby the $J_1 - J_2$ model is one of the canonical examples of geometrical frustration when both $J_1 > 0$ and $J_2 > 0$ but this time we get $J_1 > 0$ and $J_2 < 0$ resulting in absolutely no frustration in the spin sector. A similar situation happens in the 1D counterpart of the double-AF phase found in the 3D KK model being canted-A-AF phase. This means that spin frustration in the KK model is rather rare because phases with well established long-range magnetic order give no chance for spin frustration either.

Does it mean that frustration is purely orbital in the KK model? This we cannot say. First of all there is still a PVB phase present for all KK models considered here. This configuration is a good candidate for a spin-frustrated phase because it has no long-range spin order and is stable in the intermediate coupling area of the phase diagrams. One can argue that beyond cluster MF approach PVB could become a spin liquid and spin liquids, at least at higher dimension, often arise from frustrated interactions. Secondly, we have rather mysterious striped-AF phase found for 3D system which physics still remains mostly unexplained. It is possible that this phase is frustrated both in orbital and spin sector and as a result we get the a-b symmetry breaking.

Appendix A

Evaluation of the energy origin $C_{\vec{r}}(\alpha)$ in invariant subspaces

We need to express $\sum_{i=1}^{N} r_i$, which appears in $C_{\vec{r}}(\alpha)$, see Eq. (2.6), in terms of chain configurations $\{L_i\}$. This task may be accomplished by the following construction. Let us imagine certain string of r_i's written in terms of chains $\{L_i\}$ and kink areas $\{A_i\}$:

$$A_1(L_1)A_2(L_2)A_3(L_3)\cdots A_k(L_k)\ .$$

First, we want to calculate the sum of r_i's included in chains. We choose any r_i from the chain L_1 and fix its sign as $r_{\rm in}$. Now this chain gives $r_{\rm in}L_1$ contribution to the total sum of r_i's. To get to the second chain we have to pass through the first kink area A_1. If the number of kinks in A_1 is even, then the next chain will give the contribution $r_{\rm in}L_2$, and if not, then it will give the opposite number. Therefore, after passing through the whole system we will get the term

$$r_{\rm in}(L_1 + p_2L_2 + p_2p_3L_3 + \cdots + p_2p_3\ldots p_kL_k)\ , \tag{A.1}$$

where $p_i = (-1)^{K_i}$, and K_i is a number of kinks in kink area i. It is clear that the parameters $\{p_i\}$ satisfy $\prod_{i=1}^{k} p_i \equiv 1$. Now we need to calculate the sum of r_i's placed in kink areas. The sign of the first chain is already chosen as $r_{\rm in}$ so we pass to A_2. For even number of kinks in A_2 the contribution is zero. If the number is odd, then we get the sum equal $-r_{\rm in}$. Passing to the next kink area we follow the same rules but we have to change $r_{\rm in}$ into $p_2r_{\rm in}$. The total

contribution from the kink areas is then equal to

$$-p_1 r_{\rm in} \left\{ \frac{1+p_1}{2} + \sum_{i=2}^{k} p_1 p_2 \dots p_{i-1} \frac{1+p_i}{2} \right\} \ . \tag{A.2}$$

Using the results given in Eqs. (A.1) and (A.2) we obtain finally

$$\sum_{i=1}^{N} r_i = r_{\rm in} \left\{ L_1 - 1 + \sum_{i=2}^{k} p_2 p_3 \dots p_i (L_i - 1) \right\} \ . \tag{A.3}$$

Thanks to this result, we can write the energy given by Eq. (2.37) in terms of new variables $\{L_i, p_i\}$ instead of $\{r_i\}$ which are definitely more natural for the present problem.

Appendix B

Solution of the mean-field equations

Here we present briefly the solution of the self-consistency Eqs. (3.20) obtained in the single-site MF approximation. It is obtained as follows: assuming a–b symmetry of the system, i.e., putting $\chi^a = \chi^b$ and $\xi^a = \xi^b$, we derive t^a and t^c from Eq. (3.19) as functions of α and β,

$$t^c = 4g\alpha + 2gE_z + g_1, \tag{B.1}$$

$$t^a = -2g\alpha - \frac{2\beta}{\sqrt{3}}g_2 - \frac{1}{2}(2gE_z + g_1), \tag{B.2}$$

with

$$g = (\chi^a - \xi^a + 2\chi^c - 2\xi^c)^{-1}, \tag{B.3}$$

$$g_1 = g(\xi^a - \xi^c), \tag{B.4}$$

$$g_2 = (\chi^a - \xi^a)^{-1}. \tag{B.5}$$

Now we introduce a parametrization

$$\alpha = \Delta \sin\phi, \qquad \beta = \Delta \cos\phi, \tag{B.6}$$

and use the self-consistency Eqs. (3.20). From t^c one finds immediately $\sin\phi$ depending on Δ,

$$\sin\phi = -2\,\frac{2gE_z + g_1}{8g\Delta + 1}. \tag{B.7}$$

Comparing Eq.(3.20) for t^a one gets:

$$-\sin\phi - \sqrt{3}\cos\phi \;=\; 4\left(2g\Delta\sin\phi + \frac{2}{\sqrt{3}}g_2\Delta\cos\phi + gE_z + \frac{1}{2}g_1\right). \tag{B.8}$$

After inserting $\sin\phi$ into Eq. (B.8) we obtain a surprisingly simple result for $\cos\phi$:

$$\cos\phi\left(\Delta - \frac{3}{8g_2}\right) = 0. \tag{B.9}$$

This leads to two classes of solutions of self-consistency Eqs. (3.20): (i) either $\cos\phi = 0$, or (ii) $\Delta = 3/8g_2$ and $\cos\phi \neq 0$. The first option implies $\sin\phi = \pm 1$ and leads to two uniform orbital configurations with $t^c = \mp\frac{1}{2}$ and $t^a = t^b = -t^c/2$. Furthermore, using Eq. (B.7) we can calculate Δ and find the borders of these uniform phases demanding $\Delta \geq 0$.

The second option, i.e., $\cos\phi \neq 0$, implies AO-type of order with:

$$t_c \;=\; \frac{2gE_z + g_1}{3g/g_2 + 1}, \tag{B.10}$$

$$t_a \;=\; -\frac{1}{2}\frac{2gE_z + g_1}{3g/g_2 + 1} \mp \frac{\sqrt{3}}{2}\sqrt{\frac{1}{4} - \left(\frac{2gE_z + g_1}{3g/g_2 + 1}\right)^2}, \tag{B.11}$$

and with phase borders defined by the condition: $2|t^c| \leq 1$. The phase borders given here set the maximal range of the phase under consideration and cannot be treated as the lines of phase transitions shown in the phase diagram; the latter lines are determined by comparing the ground state energies E_0 calculated form Eq. (3.21).

Bibliography

[1] K. I. Kugel and D. I. Khomskii, JETP Lett. **15**, 446 (1972).

[2] P. W. Anderson, Phys. Rev. **115**, 2 (1959).

[3] J. B. Goodenough, *Magnetism and the Chemical Bond* (Interscience, New York, 1963).

[4] Y. Tokura and N. Nagaosa, Science **288**, 462 (2000).

[5] K. I. Kugel and D. I. Khomskii, Usp. Fiz. Nauk **136**, 621 (1982).

[6] H. J. Jahn and E. Teller, Proc. R. Soc. A **161**, 220 (1937).

[7] G. A. Gehring and K. A. Gehring, Rep. Prog. Phys. **38**, 1 (1975).

[8] J. van den Brink, New J. Phys. **6**, 201 (2004).

[9] N. N. Kovaleva, A. M. Oleś, , A. M. Balbashov, A. Maljuk, D. N. Argyriou, G. Khaliullin, and B. Keimer, Phys. Rev. B **81**, 235130 (2010).

[10] Z. Nussinov, M. Biskup, L. Chayes, and J. van den Brink, Europhys. Lett. **67**, 990 (2004).

[11] J. van der Brink, P. Horsch, F. Mack, and A. M. Oleś, Phys. Rev. B **59**, 6795 (1999).

[12] A. Mishra, M. Ma, F.-C. Zhang, S. Guertler, L.-H. Tang, and S. Wan, Phys. Rev. Lett. **93**, 207201 (2004).

[13] C. Zener, Phys. Rev. **82**, 403 (1951).

[14] A. M. Oleś and G. Khaliullin, Phys. Rev. B **84**, 214414 (2011).

[15] J. van den Brink and D. I. Khomskii, Phys. Rev. Lett. **82**, 1016 (1999).

[16] G. H. Wannier, Phys. Rev. **79**, 2 (1950).

[17] D. C. Mattis, *The Theory of Magnetism Made Simple* (World Scientific, Singapore, 2006).

[18] L. Longa and A. M. Oleś, J. Phys. A: Math. Gen. **13**, 1031 (1980).

[19] S. Sachdev, Phys. Rev. B **45**, 21 (1992).

[20] P. Chandra and B. Douçot, Phys. Rev. B **38**, 9335 (1988).

[21] B. Normand, Contemporary Physics **50**, 533 (2009).

[22] W. Brzezicki, J. Dziarmaga, and A. M. Oleś, Phys. Rev. B **75**, 134415 (2007).

[23] L. Balents, Nature **464**, 199 (2010).

[24] C. Castelnovo, R. Moessner, and S. L. Sondhi, Nature **451**, 42 (2008).

[25] G. Khaliullin, Prog. Theor. Phys. Suppl. **160** (2005).

[26] J. van den Brink, Z. Nussinov, and A. M. Oleś, *Introduction to Frustrated Magnetism: Materials, Experiments, Theory* (Springer, New York, 2011), pp. 631-672.

[27] L. F. Feiner, A. M. Oleś, and J. Zaanen, Phys. Rev. Lett. **78**, 2799 (1997).

[28] L. F. Feiner, A. M. Oleś, and J. Zaanen, J. Phys.: Condens. Matter **10**, L555 (1998).

[29] S. Di Matteo, G. Jackeli, C. Lacroix, and N. B. Perkins, Phys. Rev. Lett. **93**, 077208 (2004).

[30] G. Khaliullin and S. Maekawa, Phys. Rev. Lett. **85**, 3950 (2000).

[31] L. F. Feiner and A. M. Oleś, Phys. Rev. B **71**, 144422 (2005).

[32] A. M. Oleś, P. Horsch, L. F. Feiner, and G. Khaliullin, Phys. Rev. Lett. **96**, 147205 (2006).

[33] J. van den Brink, P. Horsch, and A. M. Oleś, Phys. Rev. Lett. **85**, 5174 (2000).

[34] B. Normand and A. M. Oleś, Phys. Rev. B **78**, 094427 (2008).

[35] J. Chaloupka and A. M. Oleś, Phys. Rev. B **83**, 094406 (2011).

[36] F. Vernay, K. Penc, P. Fazekas, and F. Mila, Phys. Rev. B **70**, 014428 (2004).

[37] A. J. W. Reitsma, L. F. Feiner, and A. M. Oleś, New J. Phys. **7**, 121 (2005).

[38] Z. Nussinov and E. Fradkin, Phys. Rev. B **71**, 195120 (2005).

[39] C. Xu and J. E. Moore, Phys. Rev. Lett. **93**, 047003 (2004).

[40] R. Orús, A. C. Doherty, and G. Vidal, Phys. Rev. Lett. **102**, 077203 (2009).

[41] E. Cobanera, G. Ortiz, and Z.Nussinov, Phys. Rev. Lett. **104**, 020402 (2010).

[42] B. Douçot, M. V. Feigel'man, L. B. Ioffe, and A. S. Ioselevich, Phys. Rev. B **71**, 024505 (2005).

[43] S. Gladchenko, D. Olaya, E. Dupont-Ferrier, B. Douçot, L. B. Ioffe, and M. E. Gershenson, J. Phys. Soc. Jpn. **96**, 1606 (2000).

[44] P. Milman, W. Maineult, S. Guibal, L. Guidoni, B. Douçot, L. Ioffe, and T. Coudreau, Phys. Rev. Lett. **99**, 020503 (2007).

[45] D. I. Khomskii and M. V. Mostovoy, J. Phys. A **36**, 9197 (2003).

[46] J. Dorier, F. Becca, and F. Mila, Phys. Rev. B **72**, 024448 (2005).

[47] W.-L. You, G.-S. Tian, and H.-Q. Lin, J. Phys. A **43**, 275001 (2010).

[48] H.-D. Chen, C. Fang, J. Hu, and H. Yao, Phys. Rev. B **75**, 144401 (2007).

[49] S. Wenzel and W. Janke, Phys. Rev. B **78**, 064402 (2008).

[50] F. Trousselet, A. M. Oleś, and P. Horsch, Europhys. Lett. **91**, 40005 (2010).

[51] L. Cincio, J. Dziarmaga, and A. M. Oleś, Phys. Rev. B **82**, 104416 (2010).

[52] W. Brzezicki and A. M. Oleś, Acta Phys. Pol. A **115**, 162 (2009).

[53] J. H. H. Perk, H. W. Capel, M. J. Zuilhof, and T. J. Siskens, Physica A **81**, 319 (1975).

[54] E. Eriksson and H. Johannesson, Phys. Rev. B **79**, 224424 (2009).

[55] W.-L. You and G.-S. Tian, Phys. Rev. B **78**, 184406 (2008).

[56] W. L. You, Eur. Phys. J. B **85**, 83 (2012).

[57] E. Dagotto, Rep. Prog. Phys. **62**, 1525 (1999).

[58] S. Gopalan, T. M. Rice, and M. Sigrist, Phys. Rev. B **49**, 8901 (1994).

[59] S. Trebst, H. Monien, C. J. Hamer, Z. Weihong, and R. P. Singh, Phys. Rev. Lett. **85**, 4373 (2000).

[60] C. Knetter, K. P. Schmidt, M. Grüninger, and G. S. Uhrig, Phys. Rev. Lett. **87**, 167204 (2001).

[61] P. Horsch and F. Mack, Eur. Phys. J. B **5**, 367 (1998).

[62] K. Wohlfeld, A. M. Oleś, and G. A. Sawatzky, Phys. Rev. B **75**, 180501(R) (2007).

[63] S. Notbohm, P. Ribeiro, B. Lake, B. A. Tennant, K. P. Schmidt, G. S. Uhrig, C. Hess, R. Klingeler, G. Behr, B. Büchner, et al., Phys. Rev. Lett. **98**, 027403 (2007).

[64] K. Penc, J.-B. Fouet, S. Miyahara, O. Tchernyshyov, and F. Mila, Phys. Rev. Lett. **99**, 117201 (2007).

[65] W. Brzezicki and A. M. Oleś, Phys. Rev. B **80**, 014405 (2009).

[66] W. Brzezicki, *Lectures on the Physics of Strongly Correlated Systems XIV*, vol. 1297 of *AIP Conference Proceedings* (AIP, New York, 2010), pp. 407-411.

[67] V. J. Emery and C. Noguera, Phys. Rev. Lett. **60**, 631 (1988).

[68] S. Lal and M. S. Laad, J. Phys.: Condens. Matter **20**, 235213 (2008).

[69] E. Lieb, T. Schultz, and D. Mattis, Ann. Phys. **16**, 407 (1961).

[70] J. Dziarmaga, Phys. Rev. Lett. **95**, 245701 (2005).

[71] A. Georges, O. Parcollet, and S. Sachdev, Phys. Rev. B **63**, 134406 (2001).

[72] M. Ferrero, F. Becca, and F. Mila, Phys. Rev. B **68**, 214431 (2003).

[73] W. Atisattapong and J. Poulter, New J. Phys. **10**, 093012 (2008).

[74] W. Brzezicki and A. M. Oleś, Eur. Phys. J. B **66**, 361 (2008).

[75] W. Brzezicki and A. M. Oleś, Phys. Rev. B **82**, 060401 (2010).

[76] W. Brzezicki, *Lectures on the Physics of Strongly Correlated Systems XV*, vol. 1419 of *AIP Conference Proceedings* (AIP, New York, 2011), pp. 261-265.

[77] W. Brzezicki and A. M. Oleś, J. Phys.: Conf. Ser. **200**, 012017 (2010).

[78] A. Weisse and H. Fehske, *Computational Many Particle Physics*, vol. 739 of *Lect. Notes Phys.* (Springer, Berlin, 2008), pp. 545-577.

[79] J. Zaanen and A. M. Oleś, Phys. Rev. B **48**, 7197 (1993).

[80] L. F. Feiner and A. M. Oleś, Phys. Rev. B **59**, 3295 (1999).

[81] A. M. Oleś, P. Horsch, G. Khaliullin, and L. F. Feiner, Phys. Rev. B **72**, 214431 (2005).

[82] J. Deisenhofer, I. Leonov, M. V. Eremin, C. Kant, P. Ghigna, F. Mayr, V. V. Iglamov, V. I. Anisimov, and D. van der Marel, Phys. Rev. Lett. **101**, 157406 (2008).

[83] I. Leonov, D. Korotin, N. Binggeli, V. I. Anisimov, and D. Vollhardt, Phys. Rev. B **81**, 075109 (2010).

[84] N. Binggeli and M. Altarelli, Phys. Rev. B **70**, 085117 (2004).

[85] J. C. T. Lee, S. Yuan, S. Lal, Y. I. Joe, Y. Gan, S. Smadici, K. Finkelstein, Y. Feng, A. Rusydi, P. M. Goldbart, et al., Nat. Phys. **8**, 63 (2012).

[86] M. V. Eremin, D. V. Zakharov, H.-A. K. von Nidda, R. M. Eremina, A. Shuvaev, A. Pimenov, P. Ghigna, J. Deisenhofer, and A. Loidl, Phys. Rev. Lett. **101**, 147601 (2008).

[87] I. Yamada and N. Kato, J. Phys. Soc. Jpn. **63**, 289 (1994).

[88] B. Lake, D. A. Tennant, C. D. Frost, and S. E. Nagler, Nature Materials **4**, 329 (2005).

[89] D. A. Tennant, T. G. Perring, R. A. Cowley, and S. E. Nagler, Phys. Rev. Lett. **70**, 4003 (1993).

[90] R. Caciuffo, L. Paolasini, A. Sollier, P. Ghigna, E. Pavarini, J. van den Brink, and M. Altarelli, Phys. Rev. B **65**, 174425 (2002).

[91] A. M. Oleś, L. F. Feiner, and J. Zaanen, Phys. Rev. B **61**, 6257 (2000).

[92] T. N. D. Silva, A. Joshi, M. Ma, and F. C. Zhang, Phys. Rev. B **68**, 184402 (2003).

[93] B. Frischmuth, F. Mila, and M. Troyer, Phys. Rev. Lett. **82**, 835 (1999).

[94] G. Khaliullin, P. Horsch, and A. M. Oleś, Phys. Rev. B **70**, 195103 (2004).

[95] P. Horsch, A. M. Oleś, L. F. Feiner, and G. Khaliullin, Phys. Rev. Lett. **100**, 167205 (2008).

[96] C. Ulrich, G. Khaliullin, J. Sirker, M. Reehuis, M. Ohl, S. Miyasaka, Y. Tokura, and B. Keimer, Phys. Rev. Lett. **91**, 257202 (2003).

[97] J. Sirker, A. Herzog, A. M. Oleś, and P. Horsch, Phys. Rev. Lett. **101**, 157204 (2008).

[98] A. M. Oleś, J. Zaanen, and P. Fulde, Physica B & C **148**, 260 (1987).

[99] J. B. Grant and A. K. McMahan, Phys. Rev. B **46**, 8440 (1992).

[100] A. M. Oleś, Phys. Rev. B **28**, 327 (1983).

[101] A. I. Lichtenstein, V. I. Anisimov, and J. Zaanen, Phys. Rev. B **52**, R5467 (1995).

[102] A. M. Oleś and L. F. Feiner, Phys. Rev. B **67**, 092407 (2003).

[103] M. Daghofer, A. M. Oleś, D. M. Neuber, and W. von der Linden, Phys. Rev. B **73**, 104451 (2006).

[104] E. Herdtweck and D. Babel, Z. Anorg. Allg. Chem. **474**, 113 (1981).

[105] H. Manaka, Y. Miyashita, Y. Watanabe, and T. Masuda, J. Phys. Soc. Jpn. **76**, 044710 (2007).

[106] W. Brzezicki and A. M. Oleś, Phys. Rev. B **83**, 214408 (2011).

[107] G. Jackeli and G. Khaliullin, Phys. Rev. Lett. **102**, 017205 (2009).

[108] M. Medarde, J. F. Mitchell, J. E. Millburn, S. Short, and J. D. Jorgensen, Phys. Rev. Lett **83**, 1223 (1999).

[109] M. Kubota, H. Fujioka, K. Hirota, K. Ohoyama, Y. Moritomo, H. Yoshizawa, and Y. Endoh, J. Phys. Soc. Jpn. **96**, 1606 (2000).

[110] M. Ishizuka, I. Yamada, K. Amaya, and S. Endo, J. Phys. Soc. Jpn. **65**, 1927 (1996).

[111] K. A. Chao, J. Spałek, and A. M. Oleś, J. Phys. C **10**, L271 (1977).

[112] N. D. Mermin and H. Wagner, Phys. Rev. Lett. **17**, 1133 (1966).

[113] J.-S. Zhou and J. B. Goodenough, Phys. Rev. Lett. **96**, 247202 (2006).